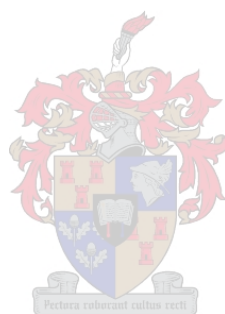


Role of Myrmekites and Associated Deformation Fabrics in Controlling Development of Granitic Mylonites in the Pofadder Shear Zone, Southern Namibia



Deyanira Graciela Cisneros Lazaro

**Submitted in Full Fulfilment of MSc Geology Department of Earth Science,
Stellenbosch University.**

April 2019

Supervisor: Dr Jodie Miller

Co-supervisor: Prof Lukas Baumgartner

DECLARATION

I declare that Role of myrmekites and associated deformation fabrics in controlling development of granitic mylonites in the Pofadder Shear Zone, southern Namibia is my own work, that it has not been submitted for any degree or examination in any other university, and that all the sources I have used or quoted have been indicated and acknowledged by complete references.

Full name: Deyanira Graciela Cisneros Lazaro

Date: April 2019

ACKNOWLEDGEMENTS

I firstly must acknowledge Dr Jodie Miller, my primary supervisor, who has been an unwavering source of academic and emotional support over the last few years and without whom this masters thesis would not have been possible. Secondly, I sincerely thank Prof. Lukas Baumgartner for acting as my co-supervisor and contributing to making my time in Switzerland a period of intense personal and professional growth. I warmly thank the following people for assistance with the collection of analytical data: Martin Robyr and Arnaud Devoir (electron probe microanalyses), Pierre Vonlanthen, Erika Harmzen-Pretorius and Madelaine Frazenburg (SEM imaging) and Laurent Nicod (thin section preparation). I am deeply grateful for the research exchange scholarship provided by the University of Lausanne. I thoroughly enjoyed my time there as the academic staff and my fellow researchers provided endless amounts of stimulating conversation and widened my view of what is possible in research. Lastly, to my sister and my parents, whose unconditional love and support, particularly from afar, sustained me and helped me achieve my goals.

Abstract

The predominantly granitic Pofadder Shear Zone (PSZ) of southern Namibia is a crustal-scale dextral shear zone exhumed from the brittle-ductile transition. A variably deformed megacrystic granite with structurally controlled myrmekite development was studied as a proxy for how alkali feldspar replacement microstructures aid in accommodating strain within granites of the PSZ. Image analysis of the S-C fabric of the protomylonites developed within the granite indicated a sinistral sense of shear and that myrmekites were preferably orientated on the S-plane. The evolving myrmekite morphology from fine-grained vermicular intergrowths to granular aggregates that were easily incorporated into the fine-grained polymineralic matrix, established myrmekite generation as a grain-size reduction and strain-accommodation mechanism within the granitic mylonites. Syn-kinematic reactions, such as myrmekite and muscovite production, were internally balanced and T-MH₂O pseudosections indicated that progressive deformation could have occurred under closed conditions. The biotite-muscovite-2-feldspar-quartz equilibrium assemblage was stable with decreasing fluid contents until fluid-saturated or slightly fluid-undersaturated conditions were reached around 2 mol % H₂O. Two-feldspar thermometry, quartz deformation textures and phengite barometry on associated muscovite growth revealed peak metamorphic conditions were around 450-500 °C and 0.5 GPa. Thermobarometry results (370 °C to ~500 °C, 0.05 – 0.5 GPa) and the wide variability in quartz rod spacing within the myrmekites support a model of continued myrmekite growth under progressively lower grade conditions as the PSZ was exhumed.

Significant myrmekite development was further documented within the polydeformed gneisses surrounding the megacrystic granite and established this strain-induced dissolution-precipitation reaction texture as being of importance within all broadly quartzo-feldspathic gneisses of the PSZ. Increased evidence for retrogression in the field and the great abundance alkali feldspar replacement textures developed within adjacent migmatitic biotite gneisses suggested that some rocks were the site of increased fluid-influx. The preservation of three morphologically and chemically different

replacement structures: myrmekites, flame perthites and albitic rims, shows that the composition of the fluid these rocks equilibrated with varied over time. The preservation of lower-temperature/higher-strain rate quartz microfabrics and the clear development of dextral kinematic indicators within the migmatitic biotite gneiss, in contrast to the sinistral S-C fabric of the megacrystic granite gneiss it is in contact with, suggests that there was some degree of lithology-based strain partitioning within these rocks. This study highlights how strain-partitioning and fluid localisation is highly variable but that myrmekites within mid-crustal granitoids can nevertheless develop and contribute to deformation under closed conditions.

TABLE OF CONTENTS

1	CHAPTER ONE: Study Contextualisation	1
1.1	Introduction	1
1.2	Problem Statement	4
1.3	Aims and Objectives.....	4
1.4	Organisation of Thesis.....	5
1.5	Geological Context	6
1.5.1	The Namaqua Orogeny	6
1.5.2	The Pella Domain	10
1.5.2.1	Orange River Group	10
1.5.2.2	Violsdrif Suite	12
1.5.2.3	Eendoorn Suite.....	12
1.5.2.4	Orange Falls Suite.....	13
2	CHAPTER TWO: Role of myrmekite and associated deformation fabrics in controlling development of granitic mylonites in the Pofadder Shear Zone of southern Namibia.....	14
2.1	Introduction	15
2.2	Geological Context	17
2.3	Analytical Methods	19
2.4	Petrography	20
2.4.1	Protomylonite	20
2.4.2	Mylonite	24
2.4.3	Myrmekite.....	25
2.4.3.1	Morphology.....	25
2.4.3.2	Occurrence	26
2.5	Mineral Chemistry.....	29
2.5.1	Feldspars	29
2.5.2	Muscovite and Biotite	31
2.6	Thermobarometry.....	31
2.6.1	Two-feldspar thermometry.....	33
2.6.2	Phengite barometry	34
2.6.3	T-MH ₂ O Pseudosections.....	34
2.7	Discussion.....	35
2.7.1	Fluid conditions during deformation	36
2.7.2	The myrmekite-formation model	39

2.7.3	Myrmekite contribution to deformation	40
2.7.4	P-T conditions of deformation	42
2.7.5	Implications for deformation of the PSZ.....	43
2.8	Conclusions	44
3	CHAPTER THREE: Heterogenous development of alkali feldspar replacement structures: influence of lithology and fluid influx	45
3.1	Introduction	45
3.2	Field Site Context	46
3.2.1	Migmatitic Biotite Gneiss.....	47
3.2.2	Quartzo-feldspathic Gneiss.....	47
3.3	Petrography	49
3.3.1	Rock types	49
3.3.1.1	Migmatitic Biotite Gneiss.....	49
3.3.1.2	Quartzo-feldspathic Gneiss.....	53
3.3.2	Feldspar and myrmekite microstructures.....	57
3.3.2.1	Migmatitic biotite gneiss.....	57
3.3.2.2	Quartzo-feldspathic gneiss.....	61
3.3.3	Kinematic Indicators	62
3.4	Discussion.....	64
3.4.1	Deformation origin for myrmekites and flame perthites	64
3.4.2	Relative timing of replacement textures	66
3.4.3	Fluid-conditions during shear zone evolution	68
3.4.4	Alkali feldspar weak, plagioclase strong?	70
3.4.5	Strain-partitioning.....	71
3.5	Conclusions	72
4	CHAPTER FOUR: Conclusions	73
4.1	Future work.....	74
	References	76
5	Appendixes.....	85
5.1	Muscovite data	85
5.2	Biotite data.....	96
5.3	Feldspar data.....	105

1 CHAPTER ONE: STUDY CONTEXTUALISATION

1.1 INTRODUCTION

As aseismic slip propagation nucleates within deeper parts of faults, understanding rock deformation at or below the brittle-ductile transition is crucial in understanding how earthquakes initiate and form (Shigematsu *et al.*, 2004). Detailed analysis of deformed granitic and quartzo-feldspathic rocks exhumed from the brittle-ductile transition (Simpson, 1985; Stel, 1986; O'Hara, 1990; Fitz-Gerald and Stünitz, 1993; Bukovská *et al.*, 2015; Han *et al.*, 2016) aids in characterising the deformation mechanisms at play. Recognising how microstructures and textures develop at different stress levels and deformation conditions helps elucidate the dynamics and movement history of fault zones (Knipe, 1989). Symplectites offer one such window into tectonic processes as they are common in deformed and retrogressed rocks (Vernon, 2004). As the characteristic spacing of phases within symplectites is primarily a function of temperature, they have uses as geo-thermometers (Joanny *et al.*, 1991; Remmert *et al.*, 2018). Ogilvie and Gibson (2017) consider the regular organisation of phases within symplectites and coronas to offer an excellent opportunity to study how chemical potential gradients control the organisation of components within rocks as P-T-X (composition) conditions change. Recent work highlights the usefulness of symplectites as indicators of specific metamorphic conditions and aiding in the calculation of detailed pressure-temperature-time paths that would otherwise have been difficult to derive due to pervasive retrogression (Lanari *et al.*, 2013).

Symplectite generation may be isochemical or involve a compositional change between parent and product. Examples of isochemical symplectite transformations include orthopyroxene–plagioclase–spinel symplectites derived from garnet during decompression (Dégi *et al.*, 2010; Obata *et al.*, 2013). In comparison, myrmekites are a specific kind of symplectite which involve the metasomatic change of alkali feldspar via Ca-, Na- and K-exchange to plagioclase and quartz (Becke, 1908; Ashworth, 1972; Abart *et al.*, 2014). Besides being useful as indicators of the temperature of deformation (Yin *et al.*, 2017), myrmekite formation within metagranites at mid-crustal conditions contributes directly to

deformation by aiding in the grain-size reduction of alkali feldspar (Simpson and Wintsch, 1989; Ree *et al.*, 2005). Specifically, myrmekite formation aids in the generation of a fine-grained matrix, which leads to reaction softening, increased deformation and further myrmekite formation in a positive feedback loop (Tsurumi *et al.*, 2002). The fine-grain size of the myrmekite promotes deformation via grain-size sensitive creep mechanisms that contribute strongly to the bulk rock weakening of granitic mylonites (Ceccato *et al.*, 2018). Hence myrmekite generation is increasingly being recognised as an important process promoting grain-size reduction and strain localisation within ductile shear zones of the granitic mid-crust (Tsurumi *et al.*, 2002; Ree *et al.*, 2005; Johnson *et al.*, 2008; Ceccato *et al.*, 2018).

This study focuses on the microstructures, particularly those associated with myrmekites, developed within granitic and other variably deformed rocks of the Pofadder Shear Zone (PSZ). The dominantly granitic PSZ is a continental-scale structure (Fig. 1.1a) that extends more than 500 km from the eastern coast of Namibia into South Africa (Moen and Toogood, 2007; Miller, 2008; Macey *et al.*, 2015) and has a deformation core that is 2-7km wide (Toogood, 1976). With spectacularly developed drag folding clearly visible on satellite imagery (Fig. 1.1b), the clockwise rotation of wall-rocks highlights the dextral strike-slip kinematics of the PSZ (Toogood, 1976; Moen and Toogood, 2007; Lambert, 2013). This is supported microstructurally by the development of predominantly dextral sigma clasts, delta clasts and S-C' fabrics (Toogood, 1976; Moen and Toogood, 2007; Lambert, 2013; Macey *et al.*, 2015; Melosh, 2015) although some infrequent sinistral shear sense indicators are reported, predominantly within the northern wall-rocks (Lambert, 2013). Deformation in the PSZ was active between 1005 ± 5 Ma and 958 ± 5 Ma as determined through U-Pb monazite dating of syn-kinematically emplaced pegmatites into earlier ductile and later brittle-retrograde fabrics (Lambert, 2013). A systematic variation in the pressure and temperature conditions recorded along the strike of the PSZ, from lower crustal depths in the west, to shallower estimates in the east, indicates that the PSZ represents an oblique transect exhumed from the transitional zone within the mid-crust (Melosh, 2015). The crustal scale, lithological character and dextral kinematics, make the PSZ an excellent case study of ancient

continental-scale strike-slip faults, analogous to the modern San Andreas Fault (Melosh, 2015; Melosh *et al.*, 2018).

This study aims to first establish whether myrmekites developed within granitic mylonites of the PSZ were deformation-induced and under what conditions they formed. This will be done by characterising the deformation mechanisms of quartz, muscovite, plagioclase and K-feldspar and how the syn-kinematic reactions between them underpin myrmekite formation. Thereafter the contribution of myrmekite generation to facilitating deformation and strain localisation can be assessed. This will contribute to understanding how myrmekite develops and evolves during ductile shearing generally and hence facilitate our understanding of how crustal-scale granitic shear zones like the PSZ nucleate and grow. Further, by comparing the occurrence of myrmekites and other alkali feldspar replacement structures within mylonites hosted within rocks of varying protoliths interleaved on a small scale, the effects of lithology and fluid-influx on alkali feldspar replacement and deformation, while controlling for bulk P-T conditions, can be evaluated.

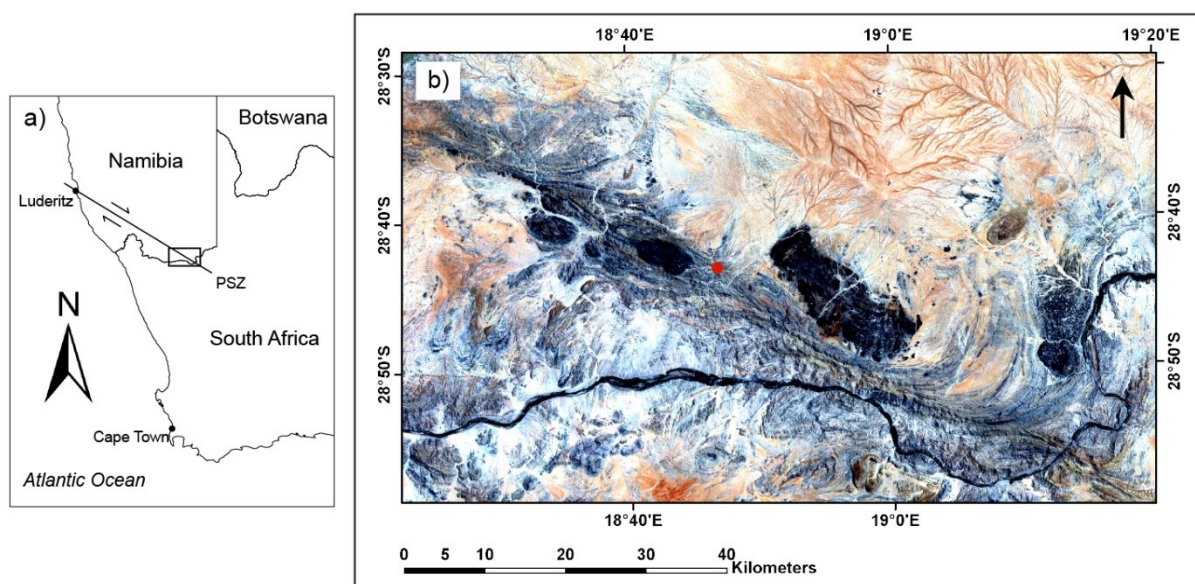


Fig. 1.1 Location maps showing the extent of the PSZ. a) Regional setting of the PSZ striking across the border between southern Namibia and South Africa. b) Landsat (ETM) Image (RGB: 321) underlines the dextral kinematics of the PSZ through the clockwise rotation of wallrocks. Red circle indicates the location of the study area

1.2 PROBLEM STATEMENT

While the P-T conditions, orientation and sense of shear of the PSZ are reasonably well constrained (Jacobs *et al.*, 1993; Thomas *et al.*, 1994), the origins of this dominantly granitic shear zone are still poorly understood. Feldspars are one of the most important minerals in controlling the rheology of granitoids at low metamorphic grades (Stünitz and Fitz Gerald, 1993). If we can characterise the development of myrmekite and understand its contribution to deformation, then this will aid in our understanding of how granitic rocks of the PSZ accommodate strain. Further, by establishing the timing relationships between alkali feldspar replacement structures and their relationship to the kinematic framework within different units, we can better constrain how strain and fluid was partitioned during progressive deformation within the PSZ.

1.3 AIMS AND OBJECTIVES

The overarching aim of this study is to establish whether myrmekite formation facilitated strain localisation within the PSZ and further, whether it can be used to constrain PSZ deformation and fluid conditions. To address this aim, the following key objectives and questions have been developed.

Objective One: To determine the spatial distribution of myrmekite within a granitic mylonite located within the PSZ

- What is the morphology of the myrmekites and what minerals are they preferentially in contact with?
- What is the chemistry of the myrmekites and the minerals they are preferentially in contact with?
- Is there a preferred orientation for the formation of myrmekite?

Objective Two: To develop a viable mechanism(s) for formation of myrmekite in the granitic gneiss

- What is the timing relationship of myrmekite formation with respect to the other major and minor minerals within the host rock?
- What are the P-T conditions of myrmekite formation and the conditions of deformation generally within the PSZ?

- What were the main drivers for myrmekite formation and what are the controls on their orientation?

Objective Three: To establish the relationship between myrmekite formation, fluid infiltration and deformation within different units of the PSZ.

- How does the occurrence and morphology of myrmekite textures within the granitic gneiss compare to other surrounding rock units?
- How do deformation textures within surrounding rocks units compare to one another and what does this imply about fluid and strain localisation during deformation?
- How did myrmekite formation contribute to deformation within the PSZ?

1.4 ORGANISATION OF THESIS

Chapters 2 and 3 within this thesis are organised as they would be presented for publication as two individual, although complementary papers. Chapter 2 focuses on the microscopic-scale deformation features of a metagranite as a proxy for how strain-induced myrmekite contributes to deformation and strain-localisation within granites of the PSZ and addresses objectives one and two. This chapter was submitted to Contributions to Mineralogy and Petrology and is being modified as suggested by the reviewers comments. Chapter 3 broadens in focus to include study into myrmekite generation within the older, poly-deformed gneisses surrounding the younger granites to assess how these have deformed, the syn-kinematic fluid-conditions their microstructures indicate and more broadly, what this implies about fluid and strain localisation as set out by objective three. This chapter requires some additional work to quantify the question of fluid-infiltration before it can be submitted for publication, which required additional data that could not be obtained on the timescale of the thesis. Chapter 4 offers concluding remarks on how myrmekite development contributed to deformation within the PSZ and avenues for further research as raised by chapter 3.

1.5 GEOLOGICAL CONTEXT

1.5.1 The Namaqua Orogeny

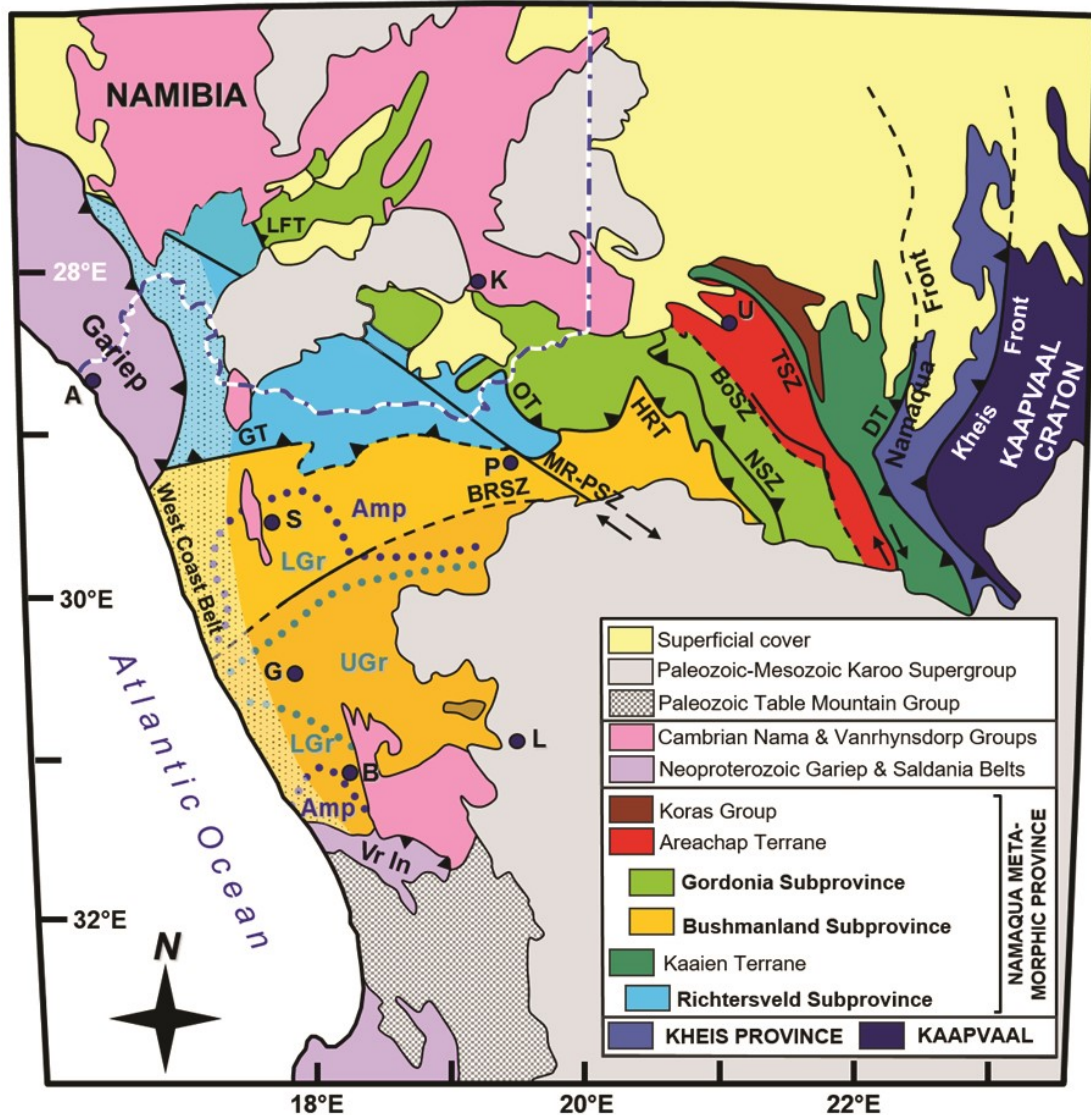


Fig. 1.2 The tectonostratigraphic subdivision of the Namaqua sector of the Namaqua-Natal Metamorphic Province (NMP) showing the position of the Richtersveld Subprovince. MR-PSZ denotes the PSZ. Note that there has been a name change from Gordonia Subprovince to Kakamas Domain that is not reflected in the figure. Taken from Macey *et al.* 2015

The PSZ is set within the Namaqua sector of the Mesoproterozoic Namaqua-Metamorphic Province (Fig. 1.2), a continuous arcuate belt which wraps around the SW edge of the Kaapvaal Craton (Cornell *et al.*, 2006; Eglington, 2006; Jacobs *et al.*, 2008; Macey *et al.*, 2015). This belt formed during the Mesoproterozoic assembly of Rodinia (Hoffman, 1991; Thomas *et al.*, 1994) through accretion of

material onto the Kalahari Craton during the Namaqua Orogeny (Cornell *et al.*, 2006; Jacobs *et al.*, 2008). There is some debate in the literature whether this final convergence represents a continent – continent and/or arc-continent-continent collisional event (Jacobs *et al.*, 1993; Thomas *et al.*, 1994) or a continental back-arc mobile belt (Bial *et al.*, 2015; Macey *et al.*, 2018). What is well established, is that as the Kaapvaal Craton moved southwards, NW-SE directed oblique dextral shearing was produced as a result of the late-stage lateral escape of the Namaqua-Natal belt (Jacobs *et al.*, 1993; Thomas *et al.*, 1994; Macey *et al.*, 2015). The geometry and sense of shear of these crustal-scale shear zones, of which the PSZ is the largest (Rennie *et al.*, 2013; Lambert, 2013), arose due to the local orientation of the abutting Kaapvaal craton (Jacobs *et al.*, 1993; Thomas *et al.*, 1994).

Based on changes in lithostratigraphy, deformation style and metamorphic character, the Namaqua Sector of the Namaqua-Natal Province has been subdivided into several domains separated by major structural discontinuities (see Hartnady *et al.*, 1985; Thomas *et al.*, 1994; Cornell *et al.*, 2006). The nomenclature presented here is following that of Macey *et al.* (2015). The Richtersveld Subprovince forms part of the NW-trending, SW-verging stack of sheets (Fig. 1.3) that characterises the western extent of the Namaqua sector after it was reworked by the Namaqua Orogeny (Clifford, 2004; Bial *et al.*, 2015; Macey *et al.*, 2017). This stack is proposed to have been juxtaposed together at the start of the Namaqua Orogeny at around 1200 Ma, with extensive magmatism and high grade metamorphism, followed by a period of extension with another period of ductile deformation that ended around 1105 Ma (Macey *et al.*, 2018). Within this stack, the Richtersveld Subprovince or Richtersveld Magmatic Arc (RMA) is found above the amphibolite- to granulite-facies Bushmanland Subprovince (Robb *et al.*, 1999) and beneath the granulite-facies Kakamas Domain (Hartnady *et al.*, 1985). The RMA was formed within a Paleoproterozoic island arc between 1910 and 1865 Ma (Reid, 1997; Macey *et al.*, 2017), having cannibalised the earlier Sperrgebiet Arc which evolved around 2.02 Ga (Macey *et al.*, 2017). The RMA is comprised of two main components, the volcano-sedimentary Orange River Group (ORG) and its intrusive equivalent, the Vioolsdrif Suite (Blignault, 1977; Reid *et al.*, 1987). As the metamorphic grades and intensity of the Namaqua Orogeny increase towards the east (Thomas *et al.*,

1994), it has been divided into two domains: (1) the greenschist facies Vioolsdrif Domain, which largely avoided Namaquan orogeny re-working; and (2) the Pella Domain which was pervasively deformed at amphibolite facies conditions of 600 °C and 5–6 kbar (Macey *et al.*, 2015, 2017; Diener *et al.*, 2017).

Due to the complex structural and metamorphic history these rocks experienced, several metamorphic episodes have been recognised. Toogood (1976) recognised six deformation episodes, which Lambert (2013) consolidated to four. These four episodes broadly corresponds to the D₁ to D₄ nomenclature of Macey *et al.* (2015) which was based on the work of Joubert (1986). This was followed by later authors (Melosh, 2015; Diener *et al.*, 2017; Macey *et al.*, 2018) and a brief outline is presented here:

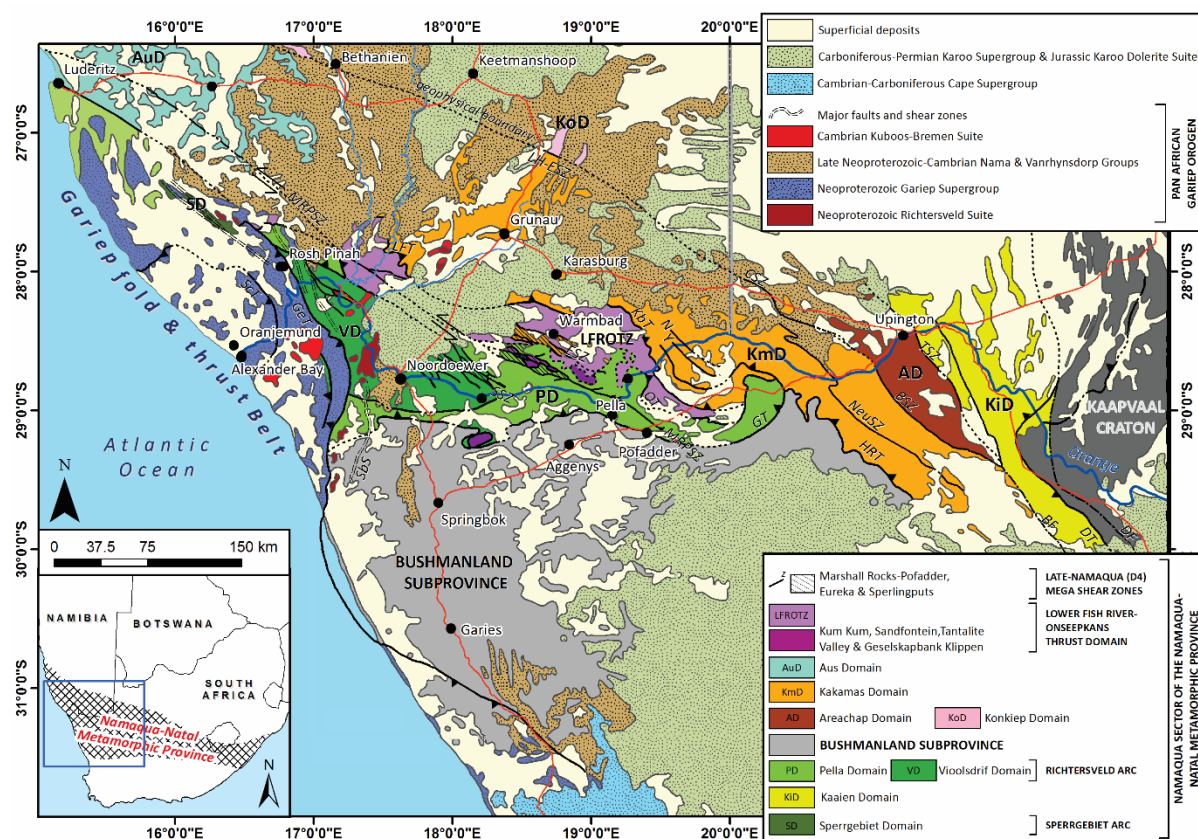


Fig. 1.3 Regional tectonostratigraphic map of the Namaqua sector showing the division of the Richtersveld Magmatic Arc into the greenschist facies Vioolsdrif Domain and the amphibolite facies Pella Domain with the PSZ hosted within the Pella Domain. Other sub-parallel NW-SE trending shear zones such as the Sperlingsputs Shear Zones (SSZ) and Eureka Shear Zone (ESZ) are indicated. Taken from Macey *et al.* (2018)

- D₁: The Orange River Orogeny at ~1.9 Ga deformed the rocks of the ORG at greenschist facies during synchronous emplacement of the Vioolsdrif Suite (Blignault, 1977; Blignault *et al.*, 1983; Moen and Toogood, 2007; Macey *et al.*, 2015)., However this fabric is only preserved within the lower grade Vioolsdrif Domain (Cornell *et al.*, 2006; Macey *et al.*, 2017).
- D₂: The D₁ fabrics in the Pella domain were destroyed during the polyphase deformation associated with the ~1.2 – 1.1 Ga Namaqua Orogeny (Macey *et al.*, 2015, 2018) which is characterised by amphibolite to granulite facies metamorphism and the development of a penetrative gneissic foliation and lineation (Toogood, 1976; Blignault, 1977; Blignault *et al.*, 1983; Colliston and Schoch, 2000, 2013; Macey *et al.*, 2015).
- D₃: Following the terminal phases of D₂, the development of east-trending megascale folding produced basin and dome structures throughout the Namaqua sector which refolded D₂ fabrics (Toogood, 1976; Colliston and Schoch, 2000, 2013; Macey *et al.*, 2015). There is some debate over the timing of the F₃ folds, however some authors contend that it is constrained by the Cu-bearing norite bodies of the Koperberg Suite rocks intruding into steep localized EW-trending near-vertical ductile folds created at ~1030 Ma (Clifford, 2004).
- D₄: This deformation episode saw the development of several sub-parallel NW-SE trending shear zones which include the Eureka Shear Zone (Angombe, 2016), the Sperlingputs Shear Zone (Indongo, 2017), and the largest of these, the PSZ, which transposed and truncated the F₃ folds (Lambert, 2013). These shear zones are broadly brittle-ductile structures characterised by retrograde metamorphism from amphibolite to greenschist facies and dated to around 1000 to 960 Ma (Toogood, 1976; Colliston and Schoch, 2000, 2013; Lambert, 2013; Macey *et al.*, 2015).

1.5.2 The Pella Domain

The PSZ is mostly hosted in the Pella Domain. The Pella Domain within the RMA is comprised of Paleoproterozoic ORG and Vioolsdrif Suite rocks. These rocks preserve a penetrative foliation and lineation as they were strongly deformed at amphibolite facies as well as being intruded by the granitic Eendoorn and Orange Falls Suites during Namaqua thrusting (Macey *et al.*, 2015). What follows below is a brief synopsis of the broader lithostratigraphic framework of the rocks deformed by the PSZ.

1.5.2.1 Orange River Group

Due to contacts between units in the ORG being highly deformed and tectonised, relative stratigraphic ages between them are not possible. ORG rocks in the Pella Domain have recently been revised to encompass four lithodemic units: (1) the dominantly meta-volcanic, minor meta-sedimentary Gaudom gneiss; (2) the dominantly supracrustal Umeis gneiss; (3) the meta-rhyolitic Gaidip gneiss; and (4) the Hom Gneiss (Macey *et al.*, 2015, 2017). A brief description modified from Macey *et al.* (2017) is provided below.

The Gaudom Gneiss occurs as an EW-trending belt across the southern and eastern part of the Pella domain (Fig. 1.4) and is a heterogeneous package consisting of dominantly biotite-hornblende gneisses and sub-ordinate quartzite, amphibolite, meta-agglomerate and rare pelitic schists. The Umeis Gneiss occurs to the north of the PSZ and is a heterogeneous succession defined by both mineralogical and grain size variations and the occurrence of stromatic leucosomes. It is mostly comprised of strongly migmatitic grey hornblende-biotite-quartz-feldspar gneisses and additional quartz-feldspar gneiss, anthophyllite-bearing gneiss, biotite schist, amphibolite, calc-silicate gneiss and sporadic aluminous garnet-sillimanite-bearing layers. The Umeis Gneiss is differentiated from the Gaudom Gneiss by being more biotite-rich, having a better defined schistosity and being more strongly migmatitic. The Gaidip Gneiss is a leucocratic quartzo-feldspathic gneiss. The Hom Gneiss consists of quartzo-feldspathic gneiss and biotite-hornblende gneiss which are intermixed. Both the Gaidip and Hom gneisses occur within the SW edges of the Pella Domain (Fig. 1.4).

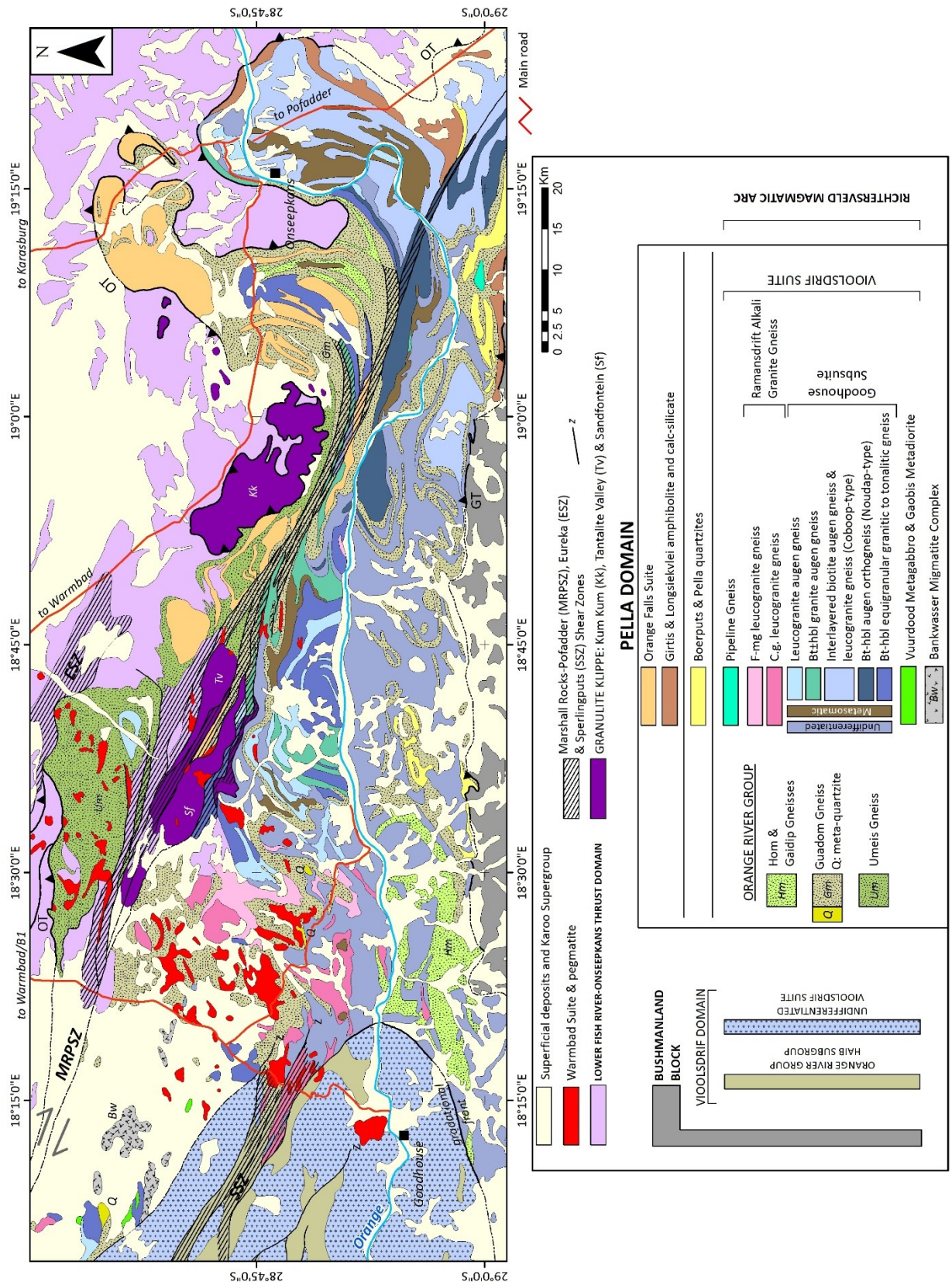


Fig. 1.4 Geological map of the Pella Domain showing the distribution of Orange River Group and its intrusive equivalent, the Vioolsdrif Suite. These were intruded by the Eendoom and Orange Falls Suites. Taken from Macey et al. (2017)

1.5.2.2 *Vioolsdrif Suite*

The Vioolsdrif Suite intrudes the rocks of the ORG and are broadly a calc-alkaline magma series of mafic to felsic plutonic rocks with minor hypabyssal and intrusive migmatitic components. Deformed orthogneisses within the Pella Domain correspond, on the basis of overlapping ages and geochemical characteristics, to the undeformed plutonic rocks of the Vioolsdrif Domain (Macey *et al.*, 2015, 2017) and are described thus below:

The Vuurdoorn Subsuite is comprised of metagabbros and hornblendite that form small plug-like bodies scattered throughout the Pella Domain. The metadioritic and metagabbroic rocks of the Gaobis Subsuite occur towards the western extent of the Pella Domain. The Goodhouse Subsuite has ten recognised subunits differentiated based on composition (tonalite-granodiorite, granite and leucogranite), gneissic texture and modal proportion of mafic minerals. The youngest rocks of the Vioolsdrif Suite are the coarse-grained to porphyritic alkali granite and fine-grained alkali granite dyke swarms of the Ramansdrif Subsuite.

1.5.2.3 *Eendoorn Suite*

The Eendoorn Suite granitoids are a range of variably deformed and sheared megacrystic to porphyroclastic metagranites (Macey *et al.*, 2015) easily identified in the field by their large (>10cm) megacrysts (Colliston and Schoch, 2006). They range in composition from granodiorite to alkali-feldspar granite and occur as a sub-horizontal sheet along the boundary between the Kakamas and Pella Domains (Macey *et al.*, 2015). Field relationships indicate that the Eendoorn is a stitching pluton, with crystallisation ages between 1230 Ma and 1190Ma, emplaced during or after the juxtaposition of the Kakamas and Pella domains, effectively gluing these tectonic blocks together (Macey *et al.*, 2015). In areas not strongly affected by shearing, the Eendoorn granites preserve a magmatic fabric with aligned phenocrysts, which suggests that intrusion occurred into a regional stress field (Macey *et al.*, 2015).

1.5.2.4 Orange Falls Suite

The Orange Falls Suite is a newly recognised unit and below is a summary from the mapping work of Macey *et al.* (2015). It is composed of three textural varieties of granitic to leucogranitic augen gneisses which also occur as dykes intruding into the ORG rocks of the Pella Domain. This suite of rocks is proposed to have intruded during the start of D₂ deformation, pre- or syn-tectonically to the juxtaposition of the Richtersveld and Kakamas Domains as opposed to the later Eendoorn Suite which was late- to post-tectonic during the regional thrust tectonics. As such, the Orange Falls Suite is differentiated from the coarsely porphyroblastic Eendoorn Suite as the latter is slightly younger and shows less intensely magmatically aligned-phenocryst fabrics.

2 CHAPTER TWO: ROLE OF MYRMEKITE AND ASSOCIATED DEFORMATION FABRICS IN CONTROLLING DEVELOPMENT OF GRANITIC MYLONITES IN THE POFADDER SHEAR ZONE OF SOUTHERN NAMIBIA

PUBLICATION NOTES

Cisneros-Lazaro DG, Miller JA, Baumgartner LP, in revision. Role of myrmekite and associated deformation fabrics in controlling development of granitic mylonites in the Pofadder Shear Zone of southern Namibia. *Contributions to Mineralogy and Petrology*, submitted 15th October, reviews received 20th November.

Abstract

Myrmekites developed within metagranites of the Pofadder Shear Zone (PSZ) in southern Namibia were investigated to understand how alkali feldspar deforms under fluid-poor mid-crustal conditions. Myrmekites showed two different morphologies: (1) 'Wormy' myrmekite with a fine-grained vermicular structure that occurred closest to the alkali feldspar host; and (2) 'recrystallised' myrmekite composed of regularly sized quartz grains that formed 120° boundaries with the plagioclase and occurred along the exterior of alkali feldspar and in contact with the mylonitic matrix. These textures were interpreted to represent two generations of myrmekite growth. Recrystallised myrmekite masses were dismembered and incorporated into the fine-grained matrix. This suggests that myrmekite formation during PSZ deformation contributed to the grain size reduction of alkali feldspar and aided in the generation of the fine-grained matrix which accommodated most of the strain. The variability of the quartz rod spacing and the wide range of results from two-feldspar thermometry and phengite barometry on associated muscovite growth indicates that peak metamorphic conditions were around 500 °C, 0.5 GPa and that myrmekite growth continued as the shear zone was exhumed. The myrmekite forming reaction is a deformation induced interface-coupled dissolution-precipitation reaction with relict magmatic plagioclase supplying the needed cationic inputs. The myrmekite forming reaction and syn-kinematic reactions were internally balanced suggesting that deformation within granitic units of the PSZ could have taken place under relatively fluid-poor conditions.

2.1 INTRODUCTION

Myrmekites have long been recognised as polygenetic (Phillips, 1980), occurring widely within different rock types and under different geological conditions. Two theories came to dominate the early discussion on the origin of myrmekite: (1) the solid-state diffusion and exsolution model (Schwantke, 1909; Phillips, 1974); and (2) the replacement model (Becke, 1908; Ree *et al.*, 2005). However, Ashworth (1986) proposed that these two models represent end-members of a continuum of reactions which produce myrmekites. Myrmekite morphology has been suggested as an important indicator for which model is more appropriate (Simpson, 1985). Phillips (1980) suggested that the replacement model of Becke (1908) accounts for the common occurrence of myrmekite within high strain zones of deformed igneous and metamorphic rocks (Phillips *et al.*, 1972; Simpson, 1985; Frisicale *et al.*, 2005; Pennacchioni, 2005; Wu *et al.*, 2017).

The preferential formation of myrmekites on the sides of grains perpendicular to the inferred incremental shortening direction suggested that elastic strain energy or strain due to tangled dislocations was the driver for myrmekite formation in deformed rocks (Simpson and Wintsch, 1989). Deformation-induced myrmekite formation may act as an important facilitator of feldspar grain-size reduction (Ree *et al.*, 2005) and is an efficient reaction-softening mechanism within granitic shear zones (Ceccato *et al.*, 2018). Myrmekite production and subsequent facilitation of deformation has been recognised across a range of deformation conditions; from middle greenschist facies (Ree *et al.*, 2005) to lower amphibolite facies (Menegon *et al.*, 2006), right through to granulite facies (De Toni *et al.*, 2016). Since feldspar is one of the main minerals controlling rock rheology at grades below amphibolite facies (Stünitz and Fitz Gerald, 1993), myrmekite formation has been increasingly highlighted as an important facilitator of deformation and strain softening in felsic rocks within the mid- to upper crust (Tsurumi *et al.*, 2002).

While myrmekites within weakly deformed granites were only found on grain surfaces orientated at large angles to the shortening direction, more strongly deformed rocks contained myrmekites on all reaction surfaces (Menegon *et al.*, 2006). This suggested that with progressive deformation, the contribution of fluid to the nucleation of myrmekite was greater than that of stress due to enhanced fluid/rock interaction. In a study of strain partitioning into dry and wet zones within syntectonic syenites deformed under granulite facies conditions, myrmekite development was restricted to wet zones as myrmekite formation was driven by the ingress of external water-rich fluids (De Toni *et al.*, 2016). However, previous studies have shown that myrmekite formation can take place within a closed system (Cesare *et al.*, 2002; Abart *et al.*, 2014). A totally open system, with an externally buffered fluid source, would be incompatible with myrmekite growth occurring at selected sites as this requires mm-scale gradients in fluid composition as controlled by local mineral reactions (Simpson and Wintsch, 1989). Experimental studies on symplectites in the CaO–MgO–SiO₂ system suggests that water influences symplectite morphology (Remmert *et al.*, 2018). Ordered symplectites with their regular spacing of phases were only generated when a small amount of water (<0.2 wt.% of total charge) was added, while at even minimally higher water contents (0.5 wt.% of total) disordered irregularly shaped ‘garben’ microstructures were formed, rather than symplectites. These authors contend that higher water contents enhance chemical mass transfer to such a degree that the generation of microstructures that minimise transport distances, such as symplectites, are not favoured. Therefore, considering the wide range of conditions under which myrmekite formation is stable, a case by case assessment of what are the drivers for their formation is likely necessary.

This paper aims to evaluate whether the syn-kinematic production of myrmekite is a strain accommodation mechanism within granites in the Pofadder Shear Zone (PSZ). The predominantly meta-granitic PSZ is a crustal scale shear zone within the Namaqua-Natal Metamorphic Belt in southern Namibia (Macey *et al.*, 2015; Melosh, 2015; Melosh *et al.*, 2018). The role of myrmekite in accommodating strain can be assessed by investigating the fluid conditions active during deformation and characterising how syn-kinematic reactions between minerals underpin myrmekite formation.

This was achieved through the petrographic and chemical characterisation of the progressive deformation of a megacrystic granite. To assess the macroscopic occurrence of myrmekite lobes in relation to the mylonitic fabric and other minerals, the orientation and thickness of myrmekite rims were analysed at different microstructural sites. Two-feldspar thermometry on the myrmekites and phengite barometry on associated muscovite growth was used to estimate temperature and pressure conditions during deformation. The results will help our understanding of deformation-induced myrmekite formation during ductile shearing generally and contribute to our understanding of the nucleation and growth history of the PSZ.

2.2 GEOLOGICAL CONTEXT

The PSZ is part of a system of NW-SE striking, oblique dextral shear zones located within the Namaqua-Metamorphic Province (NMP) spanning the border between South Africa and Namibia (Hartnady *et al.*, 1985; Thomas *et al.*, 1994; Cornell *et al.*, 2006; Eglington, 2006; Rennie *et al.*, 2013; Macey *et al.*, 2015; Melosh, 2015). The NMP is broadly a low-pressure amphibolite to granulite facies (Blignault, 1977; Diener *et al.*, 2013) belt formed during the Mesoproterozoic assembly of Rodinia (Hoffman, 1991; Thomas *et al.*, 1994) with accretion of material onto the Kalahari Craton during the Namaqua Orogeny (Cornell *et al.*, 2006; Jacobs *et al.*, 2008). The PSZ is the largest of the crustal-scale dextral shear zones (Lambert, 2013; Rennie *et al.*, 2013) produced during late-stage lateral escape of the NMP as the Kaapvaal Craton moved southwards (Jacobs *et al.*, 1993; Thomas *et al.*, 1994; Macey *et al.*, 2015). The overprinting of brittle and ductile fabrics and the syn-kinematic mineral assemblage indicates a systematic change in deformation conditions from lower amphibolite to upper greenschist as the shear zone was exhumed (Toogood, 1976; MacLaren, 1984; Lambert, 2013). U-Pb monazite dating of syn-kinematically emplaced pegmatites, ranging from 1005 ± 5 Ma to 958 ± 5 Ma, suggests that deformation occurred over a minimum of 37 Ma (Lambert, 2013). The PSZ has been suggested to be an ancient analogue of the San Andreas fault system due to similarities in lithology and deformation conditions (Melosh, 2015; Melosh *et al.*, 2018).

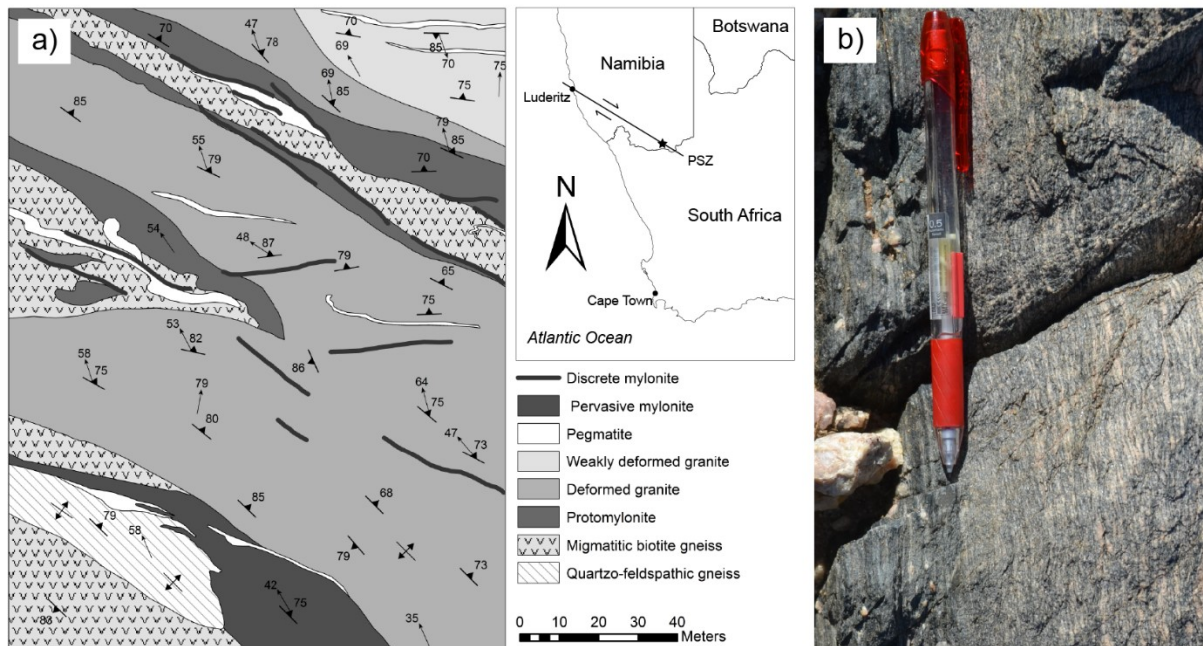


Fig. 2.1 The megacrystic granite gneiss within the PSZ. a) Small scale map showing the distribution of the megacrystic granite gneiss in relation to other units with mylonites concentrated along lithological contacts. Inset map showing the location and orientation of the PSZ. The field area is marked with a black star. b) Field photo of the transition from protomylonite to mylonite

The megacrystic gneiss in this study occurs as lensoid bodies (20-100m thick) interleaved with heterogeneous rock packages, which include variably deformed biotite schists, amphibolite boudins, quartzo-feldspathic gneisses and migmatitic biotite gneisses, deformed during the Namaqua Orogeny. Pre- and syn-tectonic pegmatites occur widely. The discrete mylonite zones developed within this granite are preferentially located at pegmatite and lithological contacts (Fig. 2.1a). The focus of this study is the occurrence of myrmekites in the transition from protomylonite to mylonite within a discrete 30cm shear zone (Fig. 2.1b) on the northern margin of the PSZ where the protolith is still recognisable. On the southern margin of the PSZ across strike from this location, Al-in hornblende deformation P-T estimates of 593 ± 119 °C at 20 -22 km depth were determined (Melosh, 2015).

2.3 ANALYTICAL METHODS

All thin sections were cut parallel to the lineation and normal to the foliation. Preliminary imaging and EDS analysis of selected domains were obtained by SEM using a ZEISS EVO MA15VP SEM at the Central Analytical Facility of Stellenbosch University, South Africa, to establish the range of mineral compositions and spatial distribution of myrmekites. Subsequently, higher resolution imaging and more detailed compositional investigation using EDX analyses were performed using a Tescan Mira II LMU SEM with a Penta-FET 3x detector with a field emission source at the Institute of Earth Sciences at the University of Lausanne, Switzerland. Mineral compositions were determined using a JEOL JXA-8530F electron probe microanalyzer (EPMA) equipped with a Schottky field emission gun at the Institute of Earth Sciences at the University of Lausanne, Switzerland. An acceleration voltage of 15 kV and a beam current of 10 nA were used for quantitative analysis. Analyses with alkali totals below 0.80 were discarded as mixed analyses of quartz and plagioclase within fine-grained myrmekite zones. Element distribution maps for Na, K, Ca, Al, Ba, Sr, Fe and Si were generated in WDS mode at an acceleration voltage of 10 kV, a 10 nA probe current and a dwell time of 40ms per pixel with a probe diameter of 0.5 μm . Modal abundances were calculated using large format BSE images for phase segmentation using the free-ware image processing software ImageJ. Fine-grained alkali feldspar and muscovite in the matrix could not be differentiated during phase segmentation due to similarities in greyscale intensity so muscovite modal abundance was estimated visually. Equilibrium phase diagrams were calculated in the system KNCFMASH using modal abundances and the compositions obtained using spot electron microprobe analysis. The calculations were performed with the DOMINO software (De Capitani and Petrakakis, 2010) and thermodynamic data taken from Berman (1988; update 92) combined with the phengite solution models of Massonne & Szpurka (1997). Activity coefficients for two-feldspar thermometry were calculated with the program AX (Holland and Powell, 2000).

2.4 PETROGRAPHY

The metagranite in this study was subdivided into protomylonite and mylonite, based on the percentage of polymineralic fine-grained matrix being more than 50 % in the latter. Macroscopically the boundary between protomylonite and mylonite is sharp (Fig. 2.1b). In thin-section the mylonite is variable in its proportion of porphyroclasts to matrix. The mylonite described below focuses on the parts of the rock that had the lowest proportion of porphyroclasts.

2.4.1 Protomylonite

The protomylonite consists of plagioclase (15 vol. %) and alkali feldspar (9 %) porphyroclasts, quartz ribbons (18 %) and rare mica fish (<5 %) set within a biotite-rich fine-grained matrix (Fig. 2.2). The protomylonite additionally contains accessory apatite, ilmenite and zircon. The rock has a banded appearance and consists of various layers of monomineralic ribbons of quartz and mica-rich zones which that around feldspar porphyroclasts within a matrix of a fine-grained polymineralic aggregate (Fig. 2.3a, b).

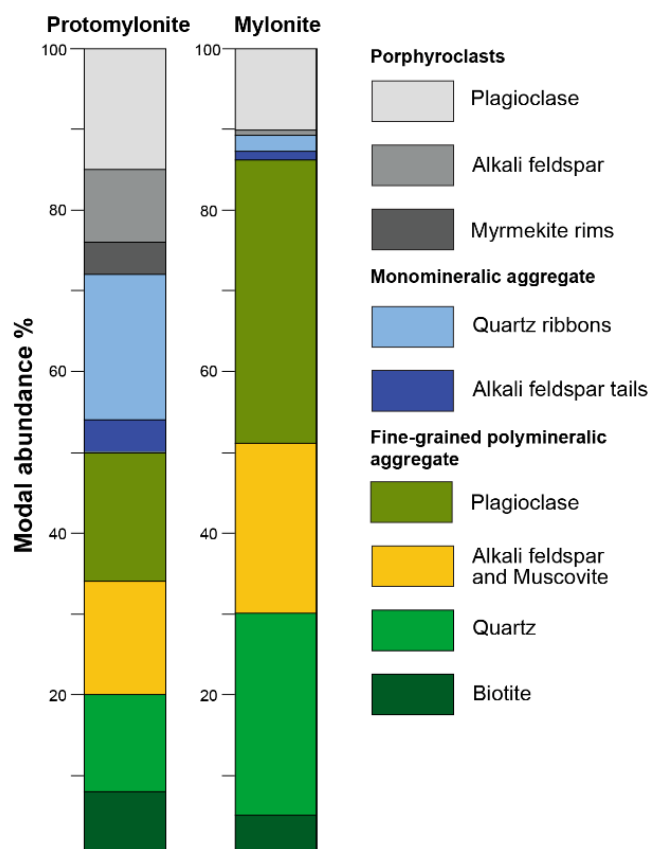
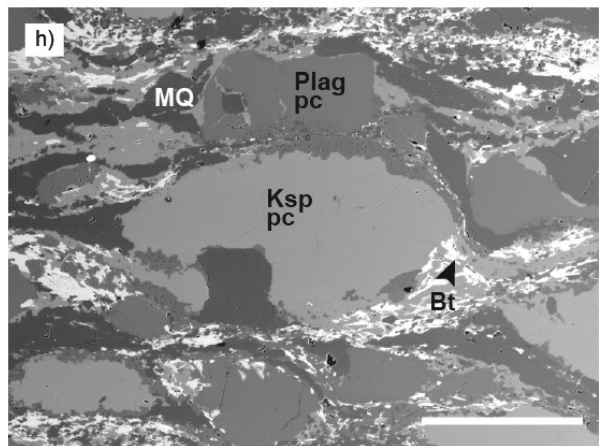
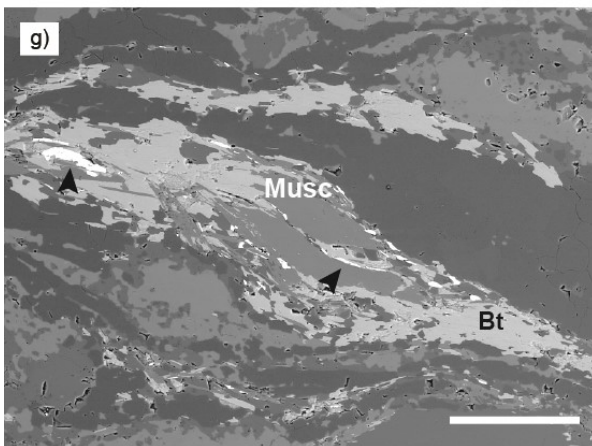
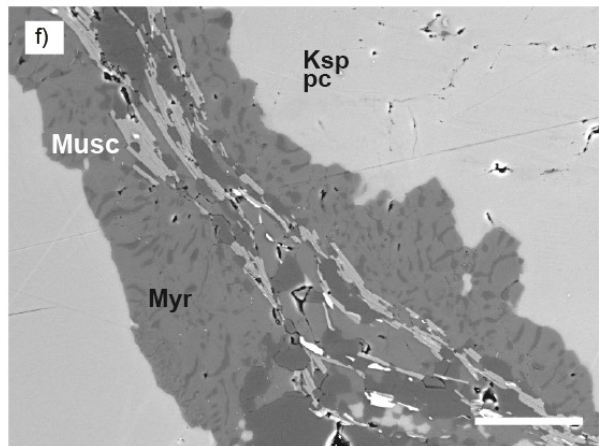
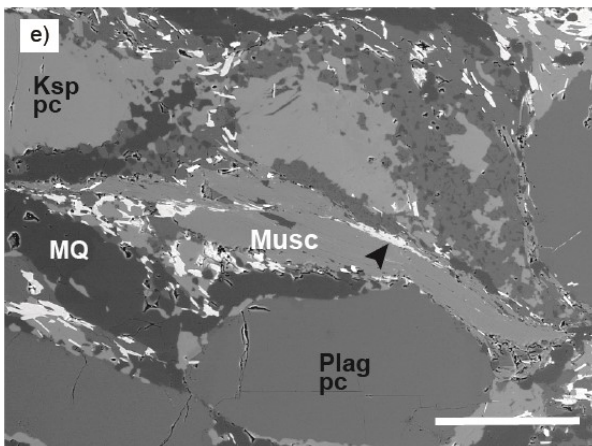
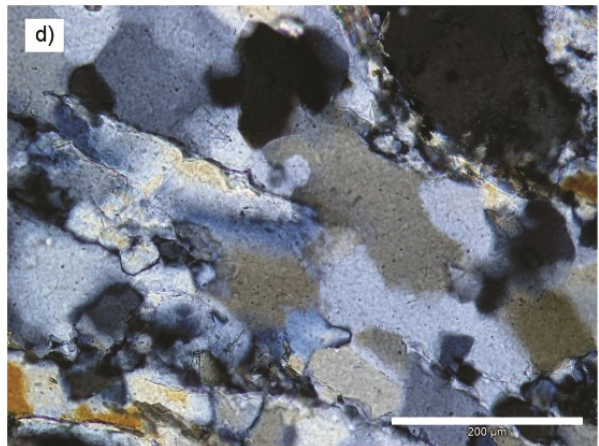
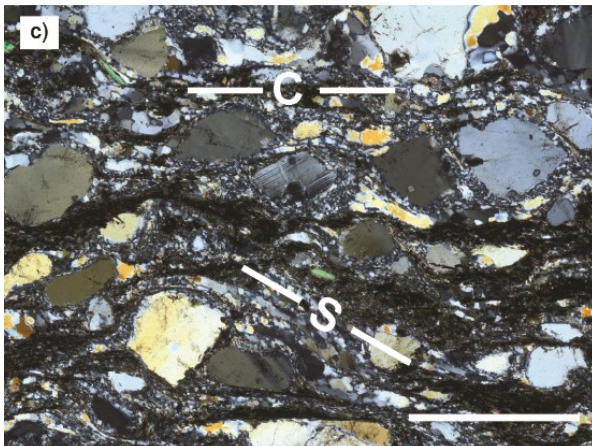
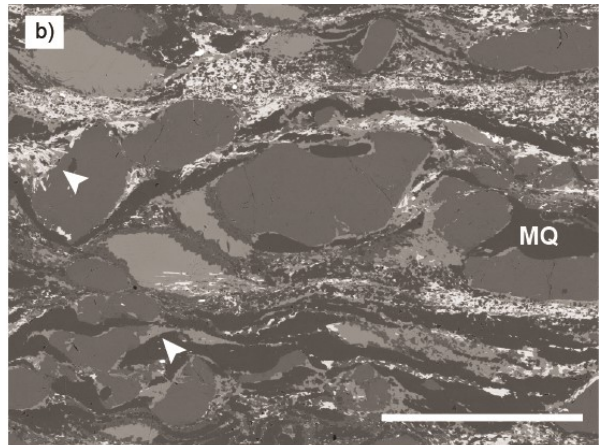
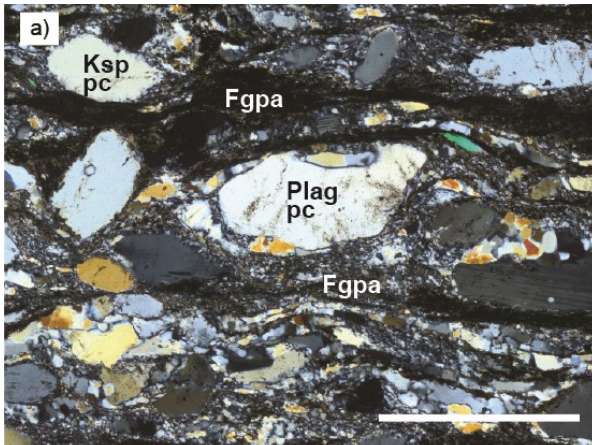


Fig. 2.2 Modal abundances of major constituent minerals in the protomylonite and the mylonite

The protomylonite has a moderately developed S-C fabric (Fig. 2.3c) with the S-surfaces preferentially containing muscovite. The S-C fabric, the orientation of the muscovite fish and the stair-step geometry of the pressure shadows indicate a sinistral sense of shear, which is contrary to the bulk shear sense of the PSZ.

Monomineralic aggregates of quartz constitute 18 % of the rock. In places the ribbons are continuous and can be traced for several mm (Fig. 2.3b). They contribute to the main mylonitic foliation and wrap around feldspar porphyroclasts. Where these aggregates are directly in contact with porphyroclasts, the contact is straight and smooth. The quartz grain boundaries within these aggregates are irregular and lobate as well as showing bulging into neighbouring grains (Fig. 2.3d). Particularly in the thinnest of these aggregates, the individual crystals are elongate in the direction of the foliation and show extensive undulose extinction and sub-grain formation. Plagioclase porphyroclasts make up 15 % of the protomylonite and range in diameter from 40 μm to 1.2 mm, with an average grain size of 300 μm . The aspect ratios (AR) range from perfectly round to 6.6, with an average AR of 1.8 (n=839). The long axes of the porphyroclasts are oriented parallel to the C-plane foliation. Some of the plagioclase grains within the matrix are untwinned, others show simple deformation twins which are not through going and taper towards the ends, but most show extensive undulose extinction. Plagioclase grains are unaltered. Alkali feldspar occurs within plagioclase along fractures, adjacent to quartz blobs and as thin trains along cleavage and twin planes.

Fig. 2.3 *Following page. Photomicrographs and SEM-BSE images of the microstructural features of the protomylonite. Unless otherwise stated C-plane foliation and lineation are horizontal. a) XPL photomicrograph of protomylonite fabric with porphyroclasts set within a fine-grained polymineralic matrix. Scale bar is 1 mm. b) SEM-BSE image of the same area as (a) showing monomineralic quartz aggregates wrapping around porphyroclasts which have extensive alkali feldspar tails (white arrows). c) XPL photomicrograph showing S-C fabric. Scale bar is 1 mm. d) Close up of quartz aggregates showing irregular grain shapes and sizes. Scale bar is 200 μm . e) Type 1 large muscovite fish are bent and kinked with biotite (black arrow) occurring along their cleavage planes. Scale bar is 100 μm . f) Muscovites associated with myrmekite (type 3) are smaller, tabular in shape and have straight contacts with the myrmekite. Scale bar is 50 μm . g) Closely intergrown biotite (type 1) and muscovite with ilmenite trails (black arrows). Scale bar is 200 μm . h) Small, tabular biotite type 3 occurring within strain shadows. Scale bar is 500 μm . Fgpa: fine-grained polymineralic aggregate. Ksp pc: Alkali feldspar porphyroclast. Plag pc: Plagioclase porphyroclast. MQ: Monomineralic quartz aggregate. Musc: Muscovite. Bt: Biotite. Myr: Myrmekite*



The alkali feldspar porphyroclasts constitute 9 % of the protomylonite and range in size from 20 μm to 1.8 mm, with an average grain size of 350 μm . They are highly elongate with an AR of 2.5 ($n=366$) and have their long axes rotated towards the S-plan. The porphyroclasts commonly contain randomly oriented biotite flakes, round quartz inclusions, and, less commonly, round inclusions of plagioclase. Most porphyroclasts show undulose extinction and bending of the twin planes, and some of them are fractured. Alkali feldspar also commonly forms fine-grained tails on the pressure shadows of feldspar porphyroclasts (white arrows Fig. 2.3b). The tails, containing also biotite, can extend for several hundreds of microns and contribute to the banded appearance of the rock.

Three kinds of muscovite can be identified based on texture and occurrence. (1) Large, typically 200-300 μm long fish define the S-plane foliation (Fig. 2.3c). These are commonly bent and kinked and in places have biotite occurring along the cleavage planes (Fig. 2.3e). (2) Tabular muscovite, between 50 and 100 μm , occurs within the mylonitic matrix and is not typically associated with biotite. (3) Fine-grained muscovite of around 50 μm in length occurs frequently along the outside rim of myrmekite lobes (Fig. 2.3f). These muscovites are tabular in shape and have straight contacts with the myrmekites. A few of these finer grained muscovite grains have thin cleavage parallel grains of ilmenite. The finer grained muscovites near myrmekite are generally not closely associated with biotite.

Similarly, three kinds of biotite are differentiated based on their morphology and occurrence: (1) Strongly pleochroic biotite grains (200 μm) that are preserved within feldspar porphyroclasts are randomly orientated to the mylonitic foliation. (2) A few isolated large grains of strongly pleochroic brown biotite within the matrix that are bent and show a strong undulose extinction. This biotite is closely intergrown with muscovite and commonly has ilmenite occurring parallel to the cleavage planes (Fig. 2.3g). (3) Small (50-100 μm) biotites that are concentrated within the strain shadows of feldspars that have straight, tabular morphologies (Fig. 2.3h). In some samples there are large (mm- to cm-scale) chlorite retrogression zones which have no relation to the fabric in the rock.

2.4.2 Mylonite

The mylonite fabric is dominated by sparse porphyroclasts in a homogenous matrix (Fig. 2.4a) that makes up 86% of the modal mineralogy of the rock. Monomineralic quartz ribbons and strain shadow phenomena are only continuous for short distances (<300 μm) (Fig. 2.4b). A poor S-C fabric is developed in some places, marked by short, discontinuous zones of biotite, occurring at an acute angle to the main foliation. There are no large biotite grains and muscovite fish are reduced to less than 100 μm . Most feldspar grains are untwinned and do not show undulose extinction like in the protomylonite (Fig. 2.4a). Plagioclase porphyroclasts range from 50 to 600 μm , with an average 220 μm grain size and have an average AR of 1.9 ($n=275$). Very few grains contain inclusions of quartz or biotite as in the protomylonite. Within the mylonite, alkali feldspar porphyroclasts are reduced to making up less than 1% of the modal abundance (Fig. 2.2), attain a maximum length of 400 μm , and are on average 200 μm in size. They are elongate (AR= 2.3, $n=52$) and have their long axes \pm parallel to the main mylonitic foliation. Many feldspar grains are fractured and some of these fractures are filled with biotite or muscovite.

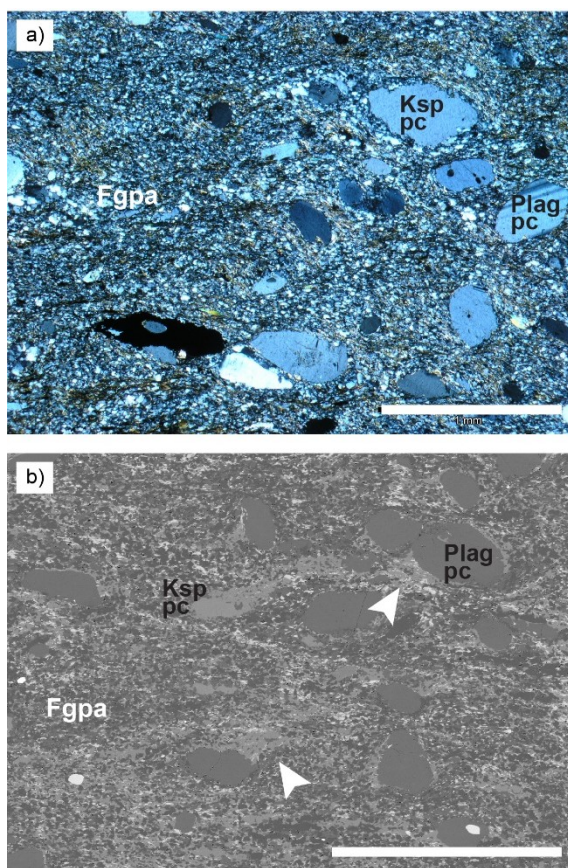


Fig. 2.4 Photomicrograph and SEM-BSE image of the mylonite. Scale bar is 1 mm. a) XPL photomicrograph of mylonite which has sparse porphyroclasts within a homogenous matrix. b) SEM-BSE image of mylonite shows the paucity of alkali feldspar porphyroclasts and the limited development of alkali feldspar tails (white arrows)

2.4.3 Myrmekite

2.4.3.1 *Morphology*

Two kinds of myrmekite were differentiated based on textural arguments: (1) 'Wormy' myrmekite that has a typical vermicular structure; and (2) 'recrystallised' myrmekite where quartz and plagioclase grains regularly form 120° grain boundaries. A myrmekite lobe or colony is here defined as a continuous growth of myrmekite with a common growth direction of the quartz rods. The wormy myrmekite lobes are convex towards the host alkali feldspar (Fig. 2.5a). These lobes are composed of neatly ordered elongate quartz rods within plagioclase that are oriented roughly perpendicular to the reaction surface with the host alkali feldspar. Within the wormy myrmekite the size and the spacing of the quartz rods is variable. There is a continuous range from where the quartz rods are large, up to 10 µm thick and 100 µm long, and have a greater spacing between them to in other places the myrmekite texture is unresolvable under SEM.

It is common to have two zones of myrmekite growth within a single myrmekite lobe, where the zones are differentiated by the size and spacing of the quartz rods. The thicker and more widely spaced quartz rods always occur on the outside of the colony and there is commonly an abrupt change to the inner portion of thinner and more closely spaced quartz rods (Fig. 2.5b). In contrast, in the recrystallised myrmekite, the quartz grains are more compact and have a regular granular size of between 5-10 µm. The plagioclase and quartz grain boundaries are commonly the site of triple-point or quadruple-point junctions (Fig. 2.5c). In places these quartz and plagioclase aggregates have a shape preferred fabric with the plagioclase grains being elongate parallel to the S-plane (Fig. 2.5d).

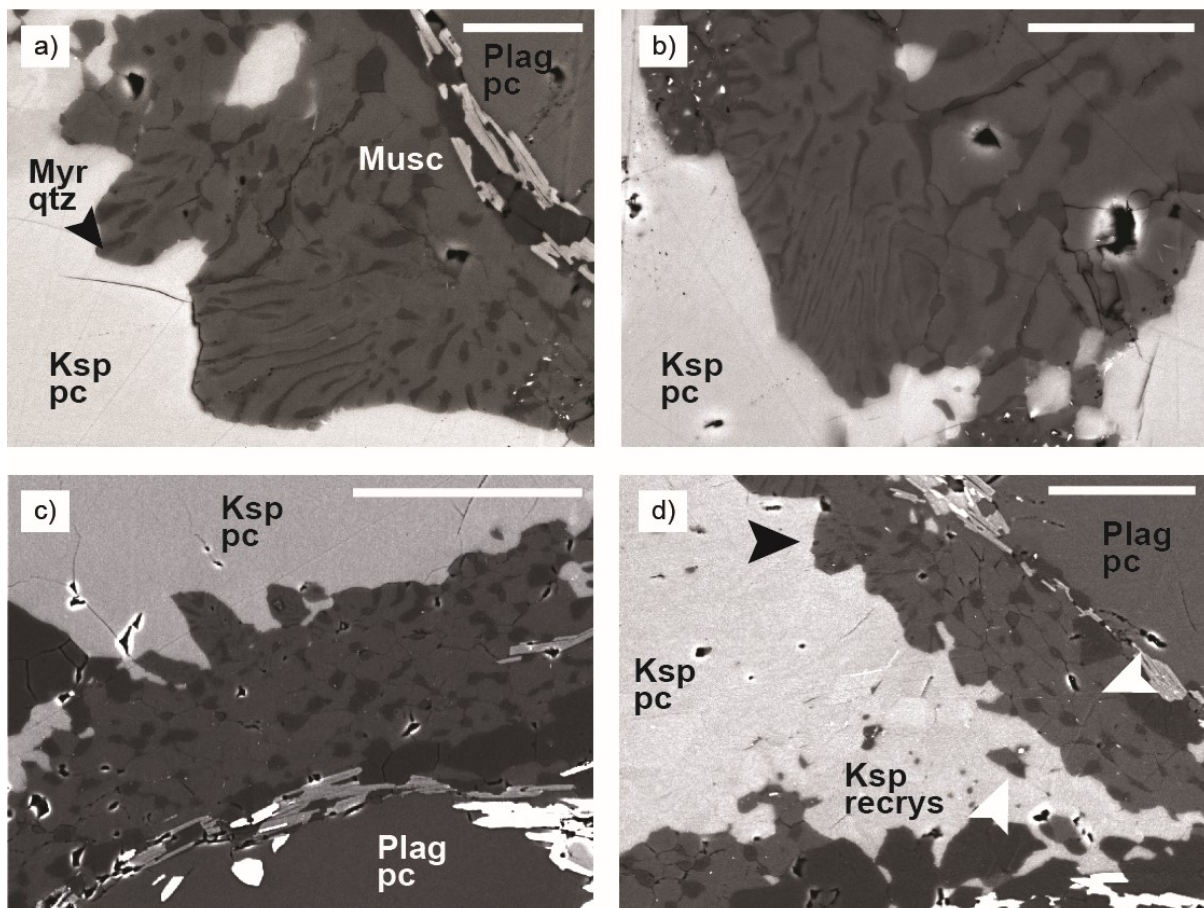


Fig. 2.5 SEM-BSE images of the morphology of the two kinds of myrmekite. a) Wormy myrmekite is composed of elongate rods of quartz within plagioclase in a convex lobe towards the alkali feldspar host. Scale bar is 20 μm . b) Wormy myrmekite shows a decreasing thickness and spacing of quartz rods within a single colony. Scale bar is 20 μm . c) The quartz grains within recrystallised myrmekite are coarser and have a regular thickness of 5-10 μm and are commonly the site of triple-junction grain boundaries. Scale bar is 100 μm . d) Recrystallised myrmekite (white arrows) showing a shape preferred fabric of the quartz and plagioclase. Black arrow indicates wormy myrmekite. Scale bar is 50 μm . Myr qtz: Myrmekite quartz. Myr plag: Myrmekite plagioclase. Ksp recryst: Recrystallised alkali feldspar

2.4.3.2 Occurrence

The orientations of the myrmekite reaction front and their widths at these locations were measured for alkali feldspar porphyroclasts in contact with the matrix, in contact with plagioclase and within intragranular fractures (Fig. 2.6). The myrmekite reaction front is here defined as the average direction of the feldspar-myrmekite boundary, with the long axes of the quartz grains typically oriented perpendicular to this. Orientations and thicknesses were calculated on coherent myrmekite rims approximately every 100 μm .

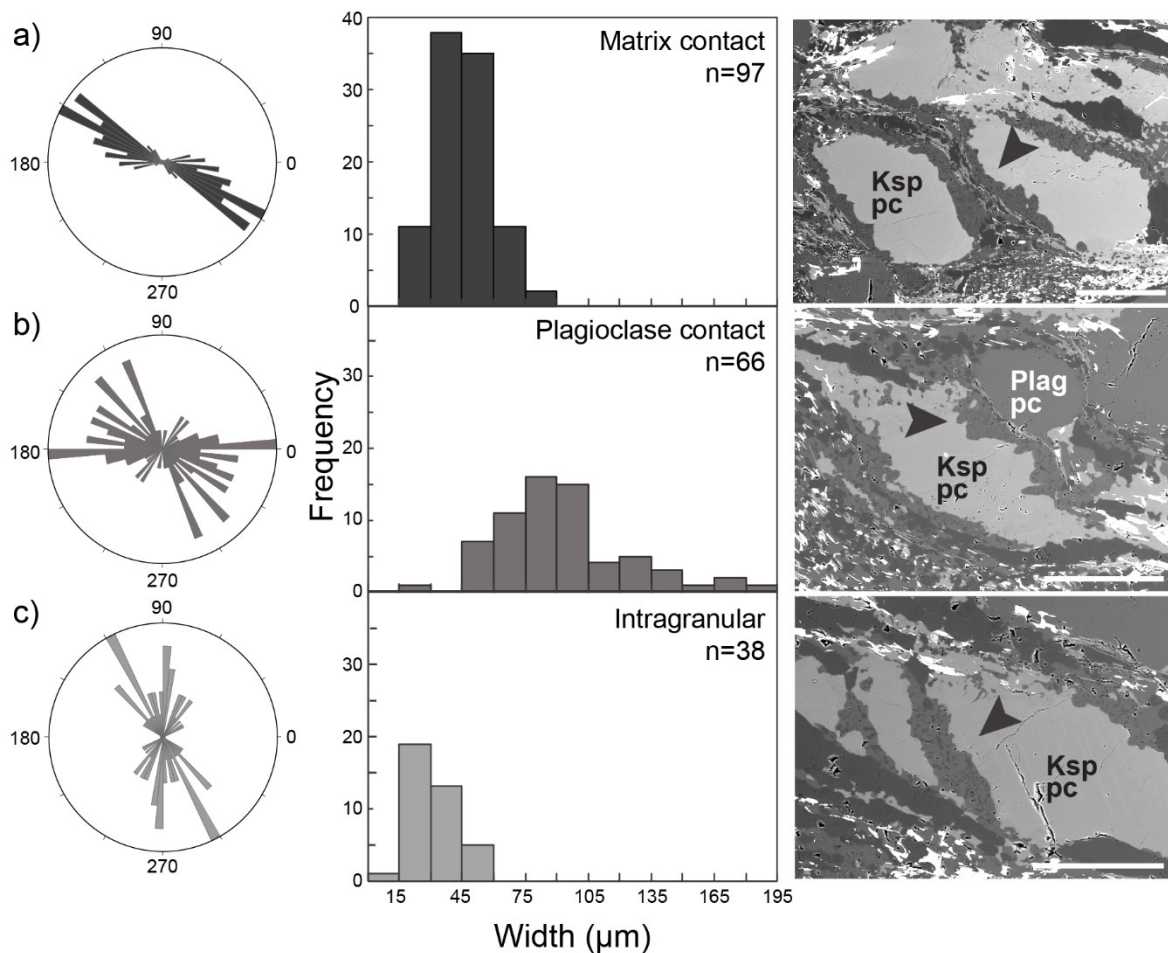


Fig. 2.6 Rose diagrams of the myrmekite reaction surface orientation at different structural sites with associated frequency plots of the width of the myrmekite lobes at these locations and an accompanying SEM-BSE image. Black arrows indicate the relevant myrmekite formation. Foliation and lineation are horizontal. Scale bar is 200 μm in all images. a) When the porphyroclast is surrounded by the matrix, the myrmekite lobes are preferentially located along the S-plane. b) Myrmekites that occur immediately adjacent to plagioclase porphyroclasts have a wide spread in their orientations and are markedly thicker. c) Myrmekites occurring along intragranular fractures occur at a high angle to the mylonitic foliation and are the thinnest. Note the parallel crack occurring to the right of the myrmekites

The myrmekites in contact with the matrix have a narrow range of orientations, strongly following the S-plane (Fig. 2.6a) and have an average width of 45 μm ($n=97$). The orientation of myrmekites in contact with plagioclase grains scatter more (Fig. 2.6b). They do not have a well-defined preferred orientation and closely wrap around the adjacent plagioclase porphyroclast (see black arrows Fig. 2.6b). Additionally, these myrmekites are markedly thicker, reaching up to 180 μm . The rare intragranular myrmekites are generally oriented at an angle to the mylonitic foliation and are the thinnest, with an average lobe thickness of 30 μm ($n=38$). Intragranular myrmekites parallel fractures

within the host alkali feldspar (Fig. 2.6c). Myrmekite rarely occurs along the interior of grains, even where alkali feldspar contains an inclusion of round plagioclase. Myrmekite is closely associated with muscovite. The muscovite occurs along the outside of the myrmekite parallel to the S-plane foliation (Fig. 2.7a). Myrmekites also occur within the tails of porphyroclasts. These myrmekites are mostly of the recrystallised myrmekite variety and often occur along the outside of the fine-grained recrystallized tails (Fig. 2.5d). These cohesive masses of recrystallised myrmekite are then progressively dismembered into the matrix. (Fig. 2.7b, c). Within the interior of some recrystallised alkali feldspar tails, angular fragments of wormy myrmekite colonies can be identified by their fine-grained quartz intergrowths (black arrow in Fig. 2.7c). Where the two kinds of myrmekite occur adjacent to one another, the wormy myrmekite always occurs towards the centre of the alkali feldspar grain whereas the recrystallised myrmekite occurs on the outer rim (Fig. 2.7d).

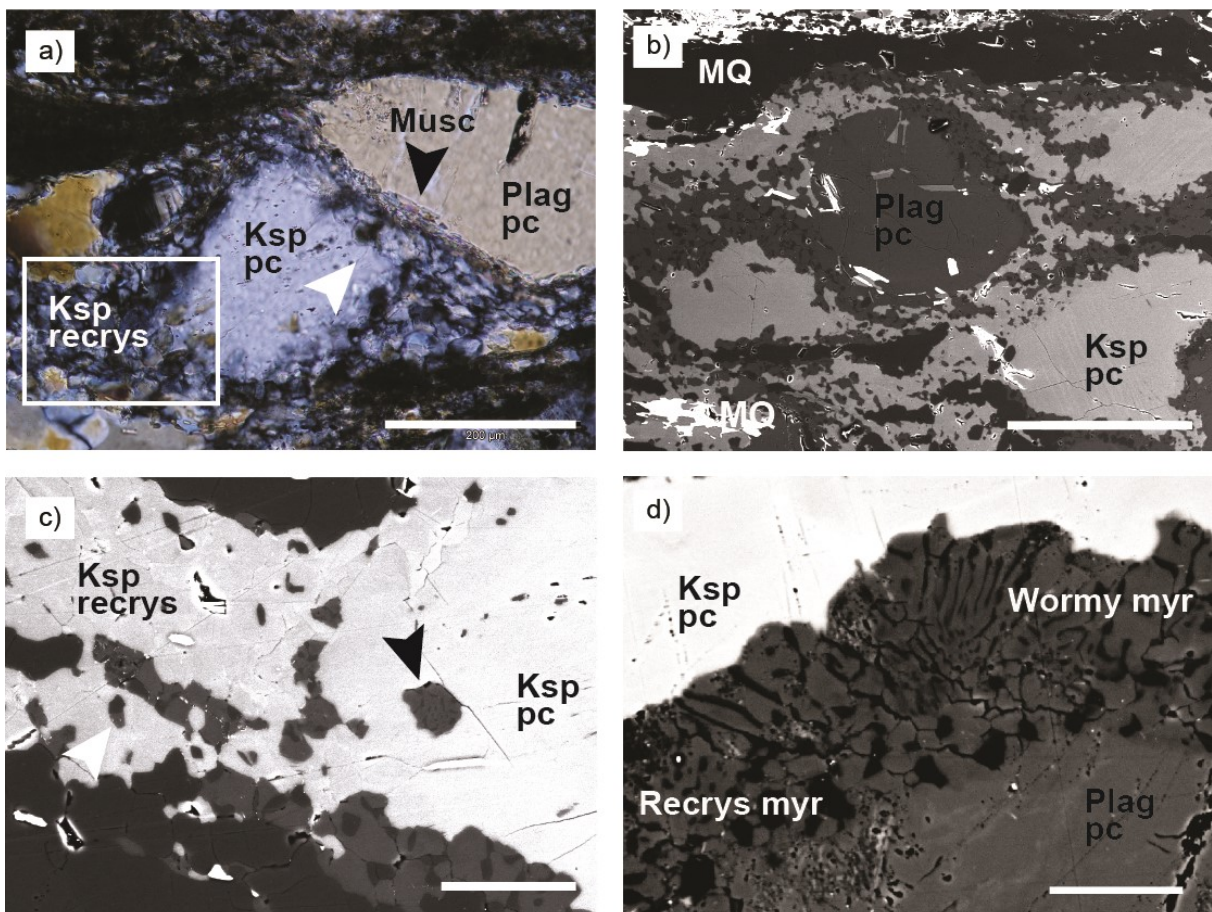


Fig. 2.7 Preceding page. Photomicrographs and SEM-BSE images of myrmekite occurrence. a) XPL photomicrograph of myrmekites well developed along the contact with a plagioclase porphyroclast (white arrow) with muscovite growing in-between. Scale bar is 200 μm . b) Coherent recrystallised myrmekite lobes being progressively dismembered and incorporated into the mylonitic matrix. Scale bar is 200 μm . c) Close up of the white rectangle in (a) showing a chunk of wormy myrmekite (black arrow) being incorporated into the recrystallised alkali feldspar tail. Scale bar is 50 μm . d) SEM-BSE image showing that wormy myrmekite occurs nearest to the alkali feldspar host while recrystallised myrmekite is always on the outer rim. Scale bar is 40 μm . Recrys myr: Recrystallised myrmekite. Wormy myr: Wormy myrmekite

2.5 MINERAL CHEMISTRY

2.5.1 Feldspars

Alkali feldspar and plagioclase porphyroclasts are not chemically zoned. The chemical compositions of porphyroclast plagioclase (n=52) show a tight range varying between An_{28-31} . They are consistently more anorthite-rich than the myrmekite and matrix plagioclase (Fig. 2.8a). The recrystallised myrmekite (n=33) and the plagioclase grains dispersed in the matrix (n=69) are chemically indistinguishable (An_{23-27}). The chemistry of the wormy myrmekite (An_{17-27} , n=39) yielded a range that extended to lower Ca contents, but most analyses were within the range of An_{23-27} , similar to the recrystallised myrmekite and the plagioclase grains in the matrix. Alkali feldspar compositions are within a restricted range of Or_{91-97} but do contain small, systematic variations linked to different textural occurrences (Fig. 2.8b). Alkali feldspar porphyroclasts (n=98) have proportionally more Na (Or_{91-94}) than the new alkali feldspar within strain shadows (Or_{93-97} , n=37) and alkali feldspars within plagioclase grains (Or_{95-96} , n=12).

Narrow zonation in plagioclase is restricted to contacts with myrmekite (Fig. 2.8c). Element distribution maps reveal a depletion of Na and enrichment of Ca relative to both, the myrmekite plagioclase it is in contact with, and the porphyroclast it is hosted in. The myrmekite itself shows little chemical zonation save for a thin rim of Na enrichment at the contact with the host alkali feldspar with a corresponding zone of Na depletion of the same width along the alkali feldspar side (Fig. 2.8c). These enrichment or depletion zones are of the same width.

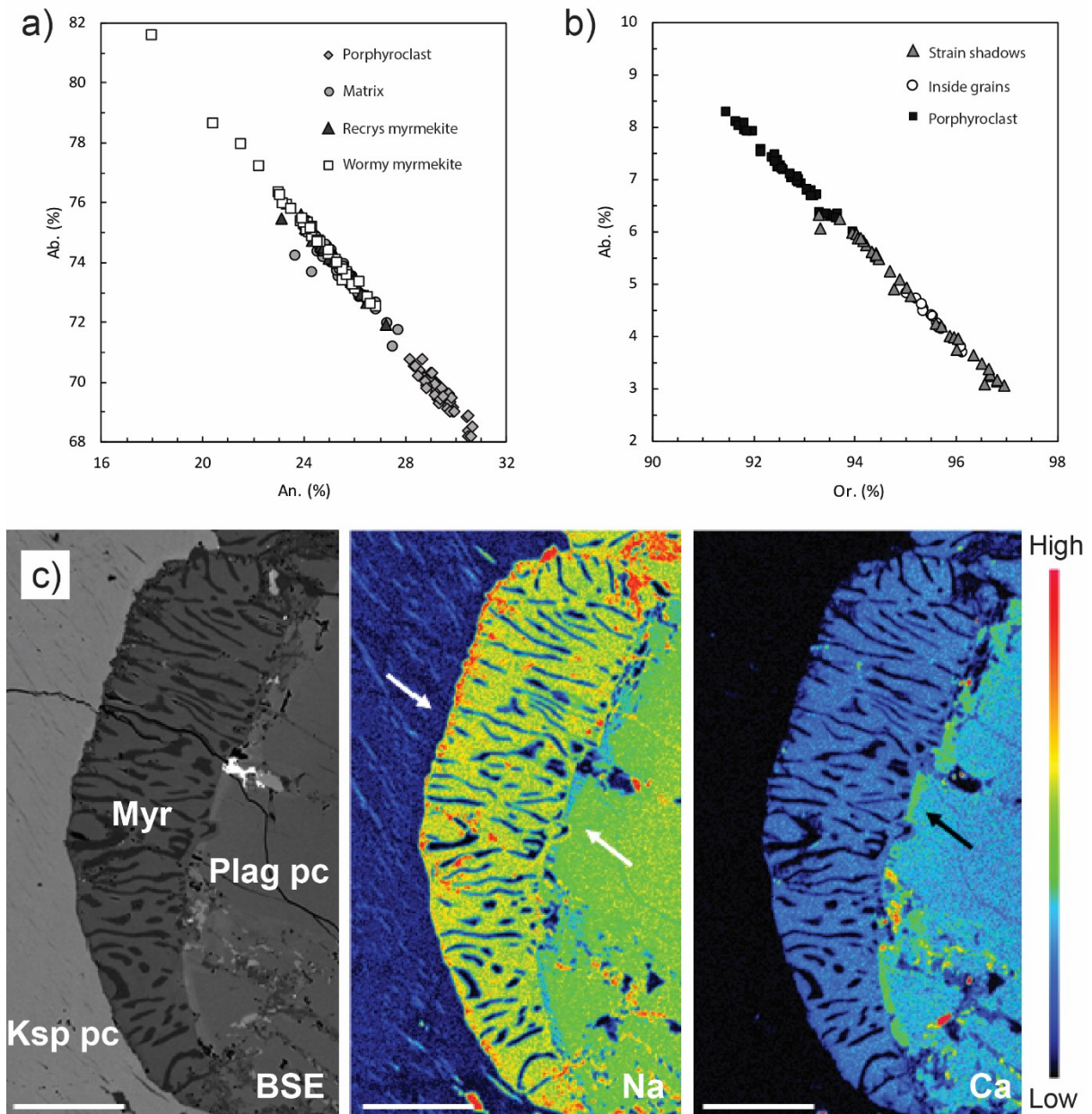


Fig. 2.8 Feldspar chemistry plots and X-ray compositional maps of a single myrmekite lobe in contact with a porphyroclast plagioclase. a) Plagioclase anorthite content showing the clear difference between porphyroclasts and rest of the plagioclase population. Wormy myrmekite, recrystallised myrmekite and the plagioclase in the matrix are chemically indistinguishable. b) Alkali feldspar orthoclase plot shows recrystallised grains have slightly lower Or %. c) SEM-BSE image and X-ray compositional maps of Na and Ca shows a strong zonation within the porphyroclast plagioclase that follows the contact with the myrmekite lobe. White arrows indicate the slight Na depletion on both sides of the myrmekite lobe and black arrow indicates Ca enrichment between the myrmekite plagioclase and the porphyroclast plagioclase. Scale bar is 50 μm

2.5.2 Muscovite and Biotite

Type 2 muscovite (n=19) showed the widest chemical variability and the widest range in celadonite substitution resulting in a Si-range of 3.10 to 3.28 Si pfu. The large muscovite fish (type 1) are differentiated chemically from type 3 muscovites occurring intergrown with the myrmekites (Fig. 2.9a). Type 1 (n=55) is characterised by having a lower, but better-defined range of phengite content, with silica between 3.07- 3.16 Si pfu, and subtle but reproducibly higher Ti contents (0.06 pfu vs 0.04) (Fig. 2.9b) and a wider range and higher proportion of Na (0.02 - 0.05 pfu). The phengite substitution of the type 3 (n=54) ranges from 3.08 to 3.23 Si pfu and Na contents are tightly constrained to between 0.02 and 0.03 pfu. There is no variability in K content between the three muscovite groups. The compositions of the biotites are overlapping. The only systematic differentiation between them was exhibited by type 1 biotite grains preserved within the feldspars (n=38) having reproducibly lower Mg contents and a median Ti content equal to or higher than the 75th percentile of the rest of the biotites (Fig. 2.9c, d). There was no systematic variation in all other elements analysed.

2.6 THERMOBAROMETRY

Mineral equilibria calculations were performed in the $K_2O-Na_2O-CaO-FeO-MgO-Al_2O_3-SiO_2-H_2O$ (KNCFMASH) model system. Thermometry and barometry were calculated for only the protomylonite, as the paucity of alkali feldspar and associated myrmekite in the mylonite made it unfeasible to calculate P-T conditions for the mylonite. For the initial pseudosections calculated for the phengite barometry, the protomylonite phase equilibria was calculated for fluid-saturated conditions (H_2O in excess). T-MH₂O pseudosections were calculated for both rocks by assuming that whole rock chemistry is constant, with the exception of the amount of water added.

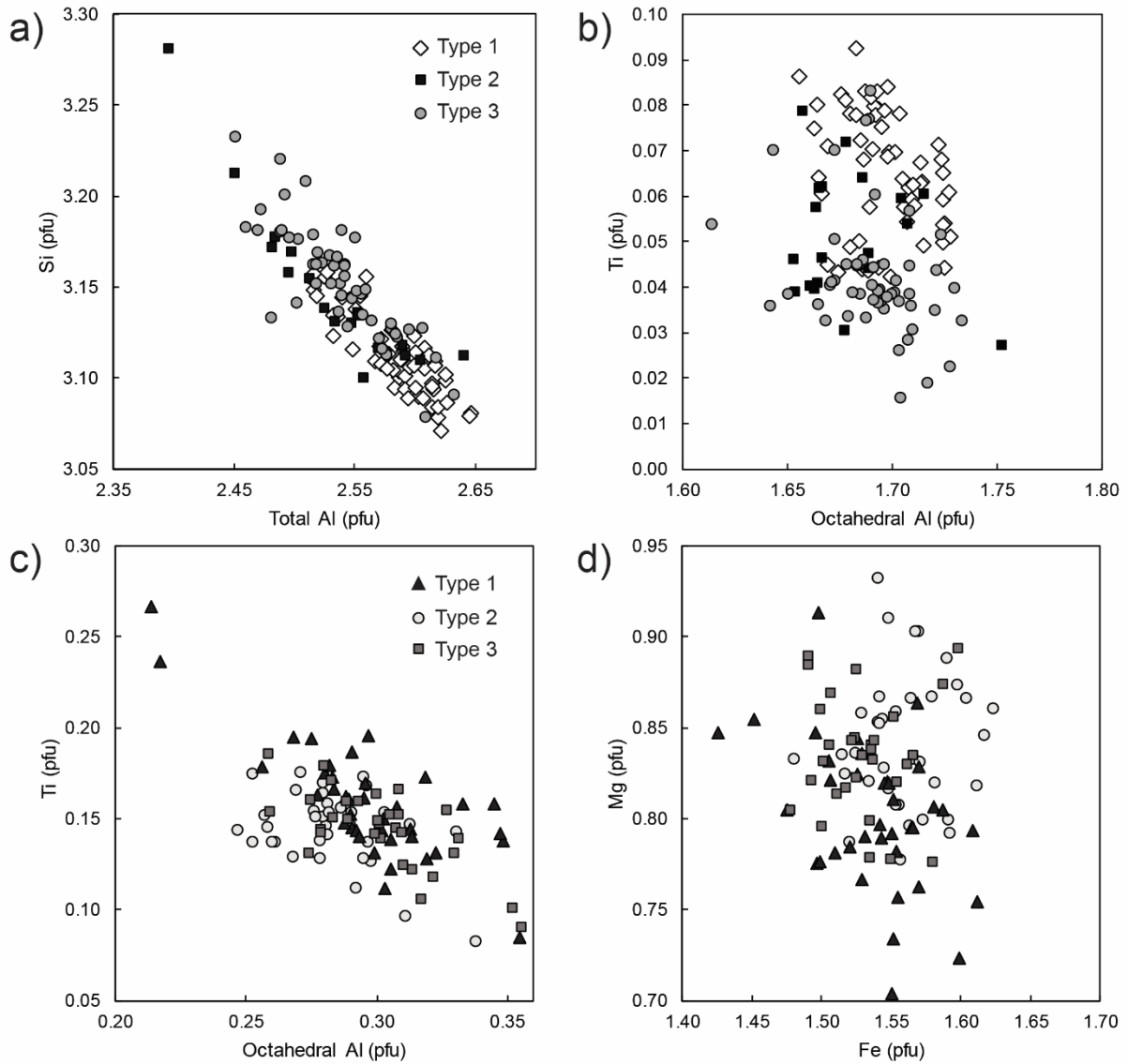


Fig. 2.9 Muscovite and biotite chemistry. a) Si vs Al in muscovite showing generally higher Si pfu for muscovite associated with myrmekite (type 3). b) Ti vs Octahedral Al plot for muscovites indicate that muscovites associated with myrmekite have lower Ti values compared to mica fish (type 1). Type 1 = Muscovite Fish. Type 2 = Muscovite defining S-plane foliation. Type 3 = Muscovite associated with myrmekite. c) Ti vs Octahedral Al plot for biotite shows a slight Ti enrichment of type one biotites found inside feldspars. d) Biotites Fe vs Mg plots show no variation in Fe, however show lower Mg for preserved biotite grains (type 1). Type 1 = Biotite grains occurring within feldspars. Type 2 = Biotite Fish. Type 3 = Biotites occurring within strain shadows of feldspars

2.6.1 Two-feldspar thermometry

As the alkali feldspar and the adjacent myrmekite plagioclase produced in the reaction are assumed to be in equilibrium, two-feldspar thermometry has been used on myrmekites to calculate temperatures of deformation (Tsurumi *et al.*, 2002; Ree *et al.*, 2005; Yin *et al.*, 2017). Although the structural states of the feldspars are not known, the feldspar thermometer employed here (Whitney and Stormer, 1977) assesses maximum order in feldspar structural states and is suitable for low anorthite/high orthoclase component pairs. 47 alkali feldspar myrmekite plagioclase pairs were calculated at assumed pressures of 0.3, 0.4 and 0.5 GPa. These calculations yielded a range of temperatures, from ~370 °C to ~500 °C, with most temperature estimates falling between 420-480 °C (Fig. 2.10). The pressures used are slightly lower than the 0.6 GPa PSZ pressure estimates at the same position along strike calculated from aluminium-in-hornblende geothermobarometry proposed by Melosh (2015). Calculations at this pressure did not yield significantly different temperatures and 0.6 GPa would result in P-T estimates located outside the biotite-phengite-two feldspar and quartz field. Based on subsequent mineral equilibria modelling presented below, 0.5 GPa was chosen as a maximum pressure for calculation.

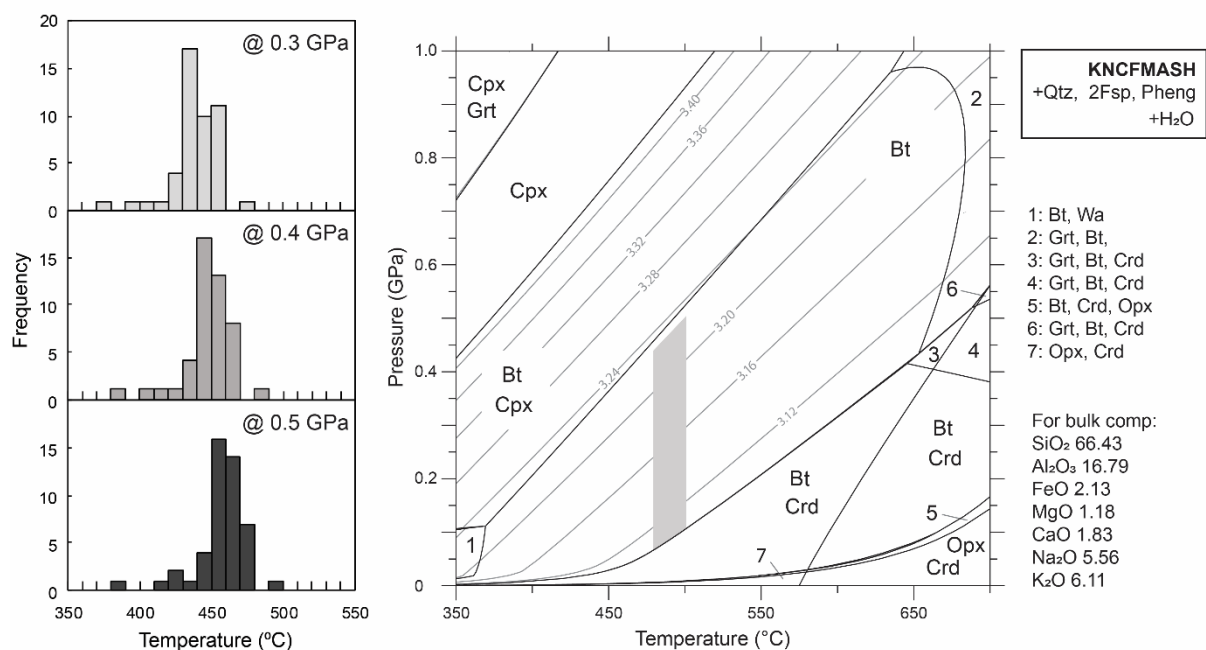


Fig. 2.10 *Preceding page. Thermobarometry results for the protomylonite. a) Results of the two-feldspar thermometry of Whitney and Stormer (1977) applied to myrmekite plagioclase and adjacent alkali feldspar calculated for assumed pressures of 0.3, 0.4 and 0.5 GPa. b) Phase diagram calculated at water-saturated conditions with superimposed Si pfu isopleths for use in phengite barometry. The shaded grey polygon represents the range of pressure given by phengite barometry assuming maximum temperatures of 480 to 500 °C. See text for explanation. Cpx: Clinopyroxene. Pheng: Phengite. Wa: Wairakite. Grt: Garnet. Crd: Cordierite. Opx: Orthopyroxene. Calculations used the modified Berman et al. (1988) database, with the modification distributed with the Domino software (De Capitani and Petrakakis, 2010)*

2.6.2 Phengite barometry

Muscovite that is intimately intergrown with the myrmekite can easily be differentiated chemically from the rest of the muscovite population, having a higher Si pfu and a generally lower Ti content (Fig. 11). The chemistry, its structurally controlled occurrence on the outside of myrmekite and its euhedral shape, indicates that it grew syn-kinematically and concomitantly with the myrmekite. This offers the opportunity to additionally calculate the pressures of formation of the myrmekite using phengite barometry. Using the maximum temperatures of deformation at 0.3 – 0.5 GPa of 480-500 °C calculated above from two-feldspar thermometry, the range of Si pfu of the only the muscovite intergrown with myrmekite yields pressures of 0.05 – 0.5 GPa (Fig. 2.10). Reduced water activities would result in slightly higher pressures for the phengite barometer and would shift the first appearance of clinopyroxene to slightly higher pressures at a given temperature.

2.6.3 T-MH₂O Pseudosections

The influence of fluid-saturation on phase equilibria can be evaluated using T-MH₂O pseudosections (Fig. 2.11). A peak pressure of 0.5 GPa, as calculated above, was used to constrain the H₂O content at peak-to-retrograde conditions over the range of temperatures suggested by two-feldspar thermometry. The T-MH₂O pseudosections were constructed for values of 1.5 – to 5 mol % to bracket the transition from fluid-undersaturated to fluid-saturated conditions in the protomylonite and mylonite. The topology of the pseudosections for both rocks are very similar; the inferred equilibrium assemblage biotite-muscovite-2-feldspar-quartz at fluid-undersaturated conditions is stable in a

narrow range close to ~2 mol % H₂O above 410 – 420 °C and the equivalent fluid-saturated assemblage is stable above 2 mol % H₂O and 490 °C.

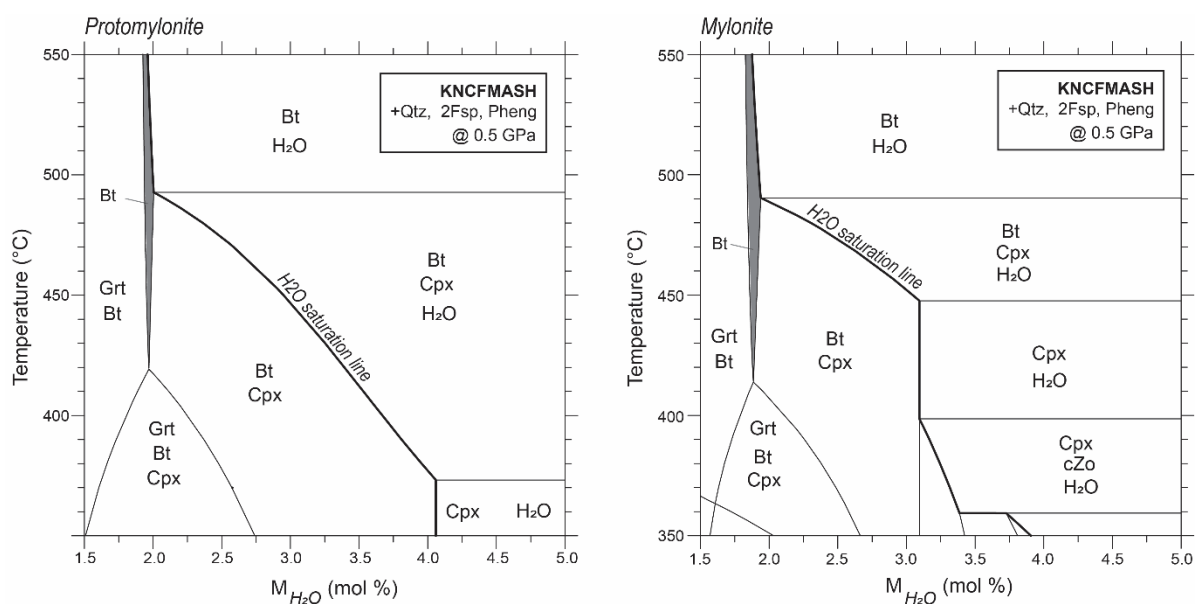


Fig. 2.11 *T–M_{H2O} pseudosections for the protomylonite and mylonite. Quartz, plagioclase and alkali feldspar and muscovite are stable across the whole pseudosection. Thick black line separates water-saturated assemblages from water-undersaturated assemblages. Grey shaded rectangle indicates the inferred equilibrium assemblage. Protomylonite bulk composition: SiO₂ 66.43, Al₂O₃ 16.79, FeO 2.13, MgO 1.18, CaO 1.83, Na₂O 5.56, K₂O 6.11, O 170.26 - 174.01. Mylonite bulk composition: SiO₂ 65.14, Al₂O₃ 18.61, FeO 1.32, MgO 0.73, CaO 2.34, Na₂O 7.06, K₂O 4.80, O 169.77 - 173.52*

2.7 DISCUSSION

The S-C fabric of the rock, the asymmetry of strain shadows, and the orientation of muscovite fish indicate a sinistral sense of shear within the metagranite. This is not consistent with the dextral kinematic indicators of surrounding rocks and the well-established dextral shear sense of the PSZ. The surrounding rocks are generally more biotite-rich and preserve a strong pre-existing fabric inherited from the Namaqua Orogeny. The opposing shear sense indicators could therefore be related to local inhomogeneities such as viscosity contrast between adjacent layers leading to strain partitioning and the preservation of domainal fabrics (Hippertt and Tohver, 1999). The S-C fabric of the protomylonite, allows for estimations of the *local* shortening direction to be made. Within alkali feldspar phenocrysts

in contact with the polymineralic matrix, myrmekite lobes are preferentially located along the S-plane of the shear fabric (Fig. 2.6). This is consistent with the nucleation of myrmekite at contractional sites and is strong evidence that they are deformation induced. With the syn-kinematic nature of myrmekite development established, the following discussion will focus on first evaluating the fluid conditions active during deformation to aid in the formulation of a myrmekite formation model. Thereafter the contribution of myrmekite to deformation, the P-T conditions of deformation suggested by myrmekites and other microstructures and finally the broader implications for PSZ deformation can be discussed.

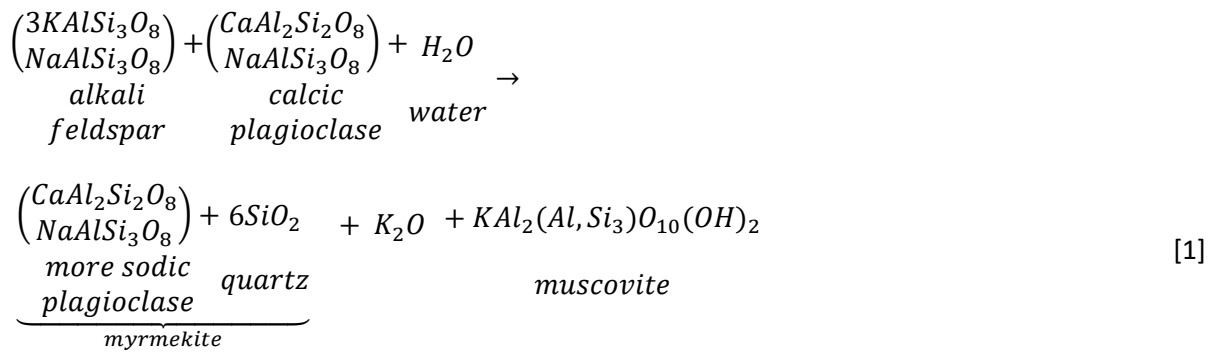
2.7.1 Fluid conditions during deformation

The reaction of alkali feldspar (approximately $Or_{93}Ab_7$) to myrmekite plagioclase (approximately $Ab_{75}An_{25}$) plus quartz is not isochemical. However, other syn-kinematic reactions within the rock balance the reaction. The small tabular biotite grains which are defining the foliation and occurring within the pressure shadows of feldspar porphyroclasts (type 3), are interpreted to be newly grown. Although they have an overall slightly higher Mg to Fe ratio, these new grains are chemically quite similar to the original biotite from which they are derived (type 1). The lower modal abundance of biotite in the mylonite compared to the protomylonite is likely due to biotite having reacted to muscovite and ilmenite, with the Ti necessary for ilmenite growth obtained from the biotite and supported by the slight change in Ti content of the old to the new biotite. While biotite to muscovite is a hydration reaction, the paucity of newly grown muscovite and the lack of retrogression of the feldspars, suggested that deformation within this granite may have occurred under relatively fluid-poor conditions. To investigate the degree of fluid saturation within the protomylonite and mylonite, an analysis of T-MH₂O pseudosections is employed.

From the T-MH₂O pseudosections it is immediately clear that no additional fluid input is necessary for progressive deformation from protomylonite to mylonite as the biotite-muscovite-2-feldspar-quartz equilibrium assemblage becomes stable at approximately the same fluid conditions (Fig. 2.11). Neither

the protomylonite nor the mylonite contain garnet or clinopyroxene, clearly demonstrating that fluid conditions were close to saturation or saturated. At 0.5 GPa, two-feldspar thermometry results range from 380 – 500 °C, with most temperatures between 440 to 480 °C. At peak temperature and pressure conditions, the biotite-muscovite-2-feldspar-quartz equilibrium assemblage is stable above M (H₂O) contents of >2 mol % H₂O for fluid-saturated conditions. However, for the rocks to maintain the equilibrium assemblage without developing clinopyroxene with decreasing temperatures below 490 °C, implies deformation below the water-saturation line along a narrow range of water contents around 2 mol % H₂O. External fluid influx at temperatures below this would shift the equilibrium and clinopyroxene would form. Since this is not the case, deformation is therefore proposed to have occurred in a closed system under decreasing fluid content with progressive deformation until fluid conditions were around 2 mol % H₂O, which indicates fluid saturated or slightly undersaturated conditions. Therefore, *local* sources and sinks for the cations involved in myrmekite formation need to be considered and the pathways for transporting them need to be identified.

Local mass transfer associated with the alkali feldspar- oligoclase reaction during myrmekite generation can be assessed from composition volume calculations (Gresens, 1967) assuming constant aluminium (e.g. Al-immobility; (Carmichael, 1969; Fisher, 1973; Mongkoltip and Ashworth, 1983). For every 100g of alkali feldspar transformed into myrmekite plagioclase, an input of 4g of CaO and 6g of Na₂O is needed, while 16g of K₂O needs to be removed (Fig. 2.12). The surplus K₂O budget is readily interpreted as contributing to alkali feldspar precipitation in strain shadows and within fractures in plagioclase. Magmatic plagioclase within this granite is the only significant Ca and Na bearing phase that could provide both cations. Both the myrmekite plagioclase and the plagioclase in the matrix are distinctly more anorthite poor (An₂₃ to An₂₇) than the magmatic plagioclase (An₂₈ to An₃₁). The close association with muscovite, especially within cracks or between adjacent alkali feldspar grains, has been linked to the transformation of alkali feldspar under retrograde conditions and can be approximated by the equation (Phillips *et al.* 1972):



The zonation within relict plagioclase that is restricted to contacts with myrmekite provide compelling evidence towards a reaction between the alkali feldspar and plagioclase during myrmekite formation. Alkali feldspar is known to be readily deformed via dissolution-precipitation mechanisms under mid-crustal conditions (Wintsch and Yi, 2002; Menegon *et al.*, 2006; Fukuda *et al.*, 2012) and the extensive development of pressure shadow phenomena within this rock is a strong indicator that this was active. Plagioclase has similarly been reported to undergo dissolution and precipitation processes in ductile shear zones (Imon *et al.*, 2002; Fukuda and Okudaira, 2013; Mukai *et al.*, 2014).

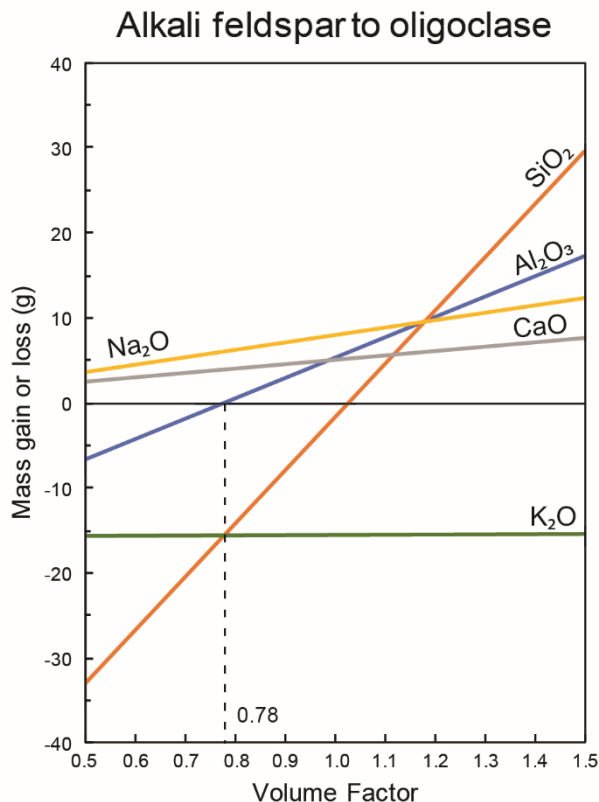


Fig. 2.12 Volume-composition relationship of alkali feldspar to oligoclase reaction during myrmekite formation based on a set of equations by Gresens (1967). See text for explanation

2.7.2 The myrmekite-formation model

The myrmekite forming reaction is seen as a deformation induced interface-coupled dissolution-precipitation reaction, where dissolved cations from relict magmatic plagioclase are effectively reprecipitated within the alkali feldspar reaction front. The excess K^+ precipitates as alkali feldspar within low-pressure sites, such as within the strain shadows of minerals, and contributes to the associated muscovite growth. When in contact with plagioclase porphyroclasts, the myrmekite lobes are much thicker, and their orientation is more random, but they closely follow the plagioclase boundary (Fig. 2.6b). The increased width of the myrmekite lobes when in direct contact with plagioclase indicates that proximity to the source of the dissolving plagioclase is an important factor. So while dissolution-precipitation processes involved in the formation of symplectites are thought to need some fluid-mediation, especially where the symplectites are not isochemical such as the myrmekites in this study (Spruzeniece *et al.*, 2017), the amount of fluid needed to change a ‘dry’ silicate system into a ‘wet’ rock system doesn’t need to exceed tens of ppm (Milke *et al.*, 2013).

Additionally for the reaction to continue, there is a need for an open fluid transport pathway to the reaction interface and this is supplied through the generation of porosity in the product phase (Putnis and Putnis, 2007). Menegon *et al.* (2006) found microstructural evidence for this porosity in the myrmekite plagioclase that was turbid under the light microscope due to ultra-small fluid inclusions. Their study used the amount of quartz within the myrmekite to estimate whether there is a volume loss within the system. This can be done by ascertaining whether Si was also conserved, as there is a relationship between the amount of quartz within the myrmekite and the composition of the myrmekite plagioclase (Phillips and Ransom, 1968). Quartz proportionality can be calculated using the following equation [1] (Ashworth, 1972) where X_{An} refers to the molar fraction of anorthite in the myrmekite plagioclase:

$$\text{Quartz volume (\%)} = \frac{90.76X_{An}}{100.21 + 91.28X_{An}} \times 100 \quad [1]$$

In this study, the range of compositions within which most myrmekite analyses fell, An₂₃ to An₂₇, yielded theoretical quartz volume values of 17.22 – 19.63%. Using greyscale segmentation of BSE images, the quartz volume within the wormy myrmekites was calculated to be 20 – 22 % with a standard deviation of 0.89 %, which is in relatively good agreement with the theoretical values suggesting that silica is being conserved. Therefore, assuming both Al and Si immobility, the mass balance calculations and theoretical and calculated quartz volumes indicate that the negative volume change associated with the myrmekite forming reaction is around 0 – 4.5%. This is somewhat lower than results reported by Menegon *et al.* (2006) of 8.5% and 10% by Simpson and Wintsch (1989). While this study finds minimal evidence for preserved microporosity, porosity is a transient microstructure which may be destroyed by subsequent recrystallisation (Putnis, 2015), as was likely the case here. The marked thinness of myrmekites formed in intragranular fractures speaks to the difficulty in transporting the cations in a relatively fluid poor environment. The different orientation of the myrmekites within intragranular fractures could be due to their formation during a later stage of deformation in an increasingly brittle environment with a different local stress field.

2.7.3 Myrmekite contribution to deformation

The morphological differences between the two types of myrmekite described within this study, and their occurrence relative to one another are interpreted to represent two generations of myrmekite growth (Fig. 2.13). Two explanations are proposed. (1) The recrystallized myrmekite occurring furthest away from the alkali feldspar host initially had a vermicular shape, but deformation caused the recrystallisation of the quartz into coarser, more compact grains with triple point junctions to reduce their energetically unfavourable high surface area. Subsequently, wormy type myrmekite was formed and was protected from further deformation, preventing disruption of its vermicular structure. (2) Alternatively the lack of a vermicular structure within recrystallised myrmekite could be due to higher water contents during the initial phase of deformation which enhanced chemical mass transfer enough so that there was no need for a vermicular structure to minimise transport distances (Remmert *et al.*, 2018). With the formation of more hydrous phases such as muscovite, which

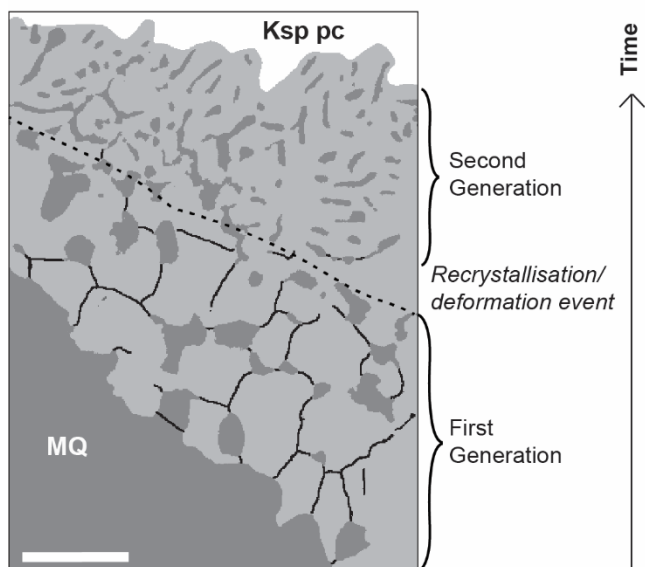


Fig. 2.13 Phase and grain boundary map showing the transition from recrystallised myrmekite to wormy myrmekite. Black lines show the grain boundaries that could reliably be identified, dark grey represents quartz with the lower portion of the image taken up by a monomineralic quartz aggregate, medium grey represents plagioclase and the white is the alkali feldspar host. Scale bar is 20 μm

consumed the available fluid, the creation of an ordered structure was needed to efficiently transport cations in and out of the reaction front. Whether or not the initially formed myrmekite was vermicular or not, it seems clear that deformation would polygonise the grains towards triple/quadruple-point boundaries as they are sheared.

(1) The ubiquity of myrmekite rims around alkali feldspar, (2) their progressive dismemberment into the mylonitic matrix, (3) the progressively smaller grain size of the porphyroclasts and (4) the reduction from 9% porphyroclasts in the protomylonite to 1% modal abundance of in the mylonite, suggests that myrmekite formation was an important grain size reduction mechanism within alkali feldspar as deformation proceeded. The occurrence of angular recognisable myrmekite blebs intermixed with recrystallised alkali feldspar along the edges of the tail of porphyroclasts, suggests that myrmekites can be sheared off from host porphyroclasts during deformation and become incorporated into the fine-grained matrix. Indeed, deformation induced myrmekite formation aids in the creation of fine-grained polymineralic aggregate, leading to reaction softening and further deformation in a positive feedback loop leading to strain localisation (Tsurumi *et al.*, 2002). Additionally, the homogenous fine-grained nature of the matrix in the mylonite (Fig. 2.4) points to some process promoting effective phase mixing. The effect of myrmekite formation during PSZ deformation is therefore two-fold: (1) contributing to the grain size reduction of alkali feldspar and (2)

promoting phase mixing and aiding in the generation of a fine-grained matrix which accommodates the majority of the strain (Ceccato *et al.*, 2018).

2.7.4 P-T conditions of deformation

Quartz-quartz grain boundaries within monomineralic quartz aggregates show a variety of crystal-plastic deformation features including undulose extinction, elongate subgrains, amoeboid grain boundaries and irregular shapes and sizes. The relative abundances of these features is indicative of some dislocation creep regime 2 but mostly regime 3 predominating (Hirth and Tullis, 1992) which corresponds to the sub-grain rotation/grain boundary migration transition which is estimated to occur around ~ 500 °C (Stipp *et al.*, 2002a). The combination of undulatory extinction, deformation twinning and myrmekite formation corresponds to Structural Zone 3 of Pryer (1993) and is indicative of temperature conditions between 450 and 500 °C. Microstructural observations and two-feldspar thermometry are therefore in good agreement and indicate that peak deformation conditions were around 450 and 500 °C. These peak temperature estimates are lower than the 593 ± 119 °C of the study by Melosh (2015) and could be related to the location of the study site on the outer margins of the high-strain core.

Additionally, the spacing of the quartz rods can be used to derive conclusions on the temperature conditions of myrmekite growth. Microstructural evolution of symplectites is controlled by the interplay of two processes: on the one hand, the chemical segregation of components by diffusion within the reaction interface, and on the other, the sum of the processes of bond breaking/forming and atomic rearrangement, i.e. the interface reaction (Gaidies *et al.*, 2017). The spacing of lamellae in symplectites is a thus function of the relative contributions of these two processes to overall resistance of the interface motion, with the main controlling factor being the diffusion rate, which depends on temperature (Vernon, 2004). Experimentally synthesised symplectites show that the increased spacing with increased temperature is due to the comparatively high activation energy for diffusion within the reaction front as opposed to the activation energy required for the interface reactions at

the reaction front (Remmert *et al.*, 2018). The relationship between temperature and the spacing of lamellae in symplectites is well established for a wide range of chemical systems in nature including symplectites composed of clinopyroxene and magnetite (Ashworth and Chambers, 2000) or amphibole and spinel (Mongkoltip and Ashworth, 1983).

Specifically within myrmekites, it is understood that decreasing temperatures leads to a decrease in the spacing of the quartz rods (Wirth and Voll, 1987; Harlov and Wirth, 2000; Abart *et al.*, 2014). The wide range of quartz rod sizes and spacing, as well as the successive decrease in their spacing towards the center of the host alkali feldspar crystal (Fig. 6b), suggests that myrmekites formed under decreasing temperature conditions as the rock was exhumed. The phengite barometry, which yielded pressures of 0.05 - 0.5 GPa, is consistent with myrmekite and muscovite growth during retrograde conditions over an extended period as the shear zone was exhumed.

2.7.5 Implications for deformation of the PSZ

The PSZ does not follow any pre-existing structures and its location is poorly understood. As the PSZ deforms mostly granite dominated terranes (Macey *et al.*, 2015), clearly establishing myrmekites as facilitators of deformation within its granitic rocks offers a clue as to why it nucleated in these locations. That the myrmekites can form under closed-system conditions implies that a rock need only have the correct mineralogy to start with, i.e. alkali feldspar and a source for Ca and Na, such as plagioclase, to form and deform myrmekite during shearing at these P-T conditions. Pegmatites occur widely across the length of the PSZ (Lambert, 2013), and myrmekite formation and subsequent recrystallisation in pegmatites elsewhere has been linked to aiding in their weakening (Pennacchioni, 2005). It is therefore important to investigate whether the surrounding quartzo-feldspathic lithologies also contain strain-induced myrmekites to investigate whether this is more than just a locally important feature. Additionally, this study documents myrmekites as forming continuously with decreasing temperature. It is therefore possible that myrmekite growth will be identified further down-strike under progressively lower-grade conditions of the differentially exhumed PSZ (see

Melosh *et al.* (2015) for a discussion of P-T conditions along the PSZ) as myrmekite growth elsewhere has been documented at temperatures as low as 340 °C (Tsurumi *et al.*, 2002; Ree *et al.*, 2005).

2.8 CONCLUSIONS

Within metagranites of the PSZ, myrmekite growth contributed to the grain-size reduction of alkali feldspar, promoted phase-mixing within the mylonitic matrix and hence potentially to the localisation of strain. Contrary to the findings that myrmekite production in granulite facies rocks necessarily requires external fluid input to catalyse myrmekite formation and subsequent facilitation of deformation (De Toni *et al.*, 2016), this study finds that myrmekite production and contribution to deformation within amphibolite facies rocks can take place within a relatively closed system. This is likely due to mid-crustal biotite rich rocks containing enough internal fluid that is buffered by local mineral reactions to create mm-scale fluid gradients which cause the preferential growth at selected high-strain sites. The myrmekite forming reaction is a deformation induced interface-coupled dissolution-precipitation reaction with cationic inputs from relict magmatic plagioclase reprecipitated at the reaction front with host alkali feldspar. The excess K₂O contributes to the formation of alkali feldspar tails within strain shadows and to associated muscovite growth. The close association of myrmekite with porphyroclast plagioclase is due to proximity to the cation donor plagioclase being important in fluid-poor conditions. This indicates that despite voluminous syn-kinematic pegmatite intrusions offering a large external fluid source, ductile deformation within metagranites of PSZ could have taken place in a closed system with myrmekite production aiding in deformation. The syn-kinematic mineral assemblage, quartz and feldspar microstructures, and two-feldspar thermometry indicate that peak metamorphic conditions were around 450-500 °C and 0.5 GPa. The successive decrease in quartz rod spacing towards host alkali feldspar and the wide range of pressures obtained from phengite barometry on associated muscovite reveals that myrmekite growth proceeded with deformation under successively lower P and T conditions as the shear zone was exhumed. This study highlights that myrmekites can successfully develop and contribute to grain-size reduction and strain localisation as deformation progresses under relatively fluid-poor conditions.

3 CHAPTER THREE: HETEROGENOUS DEVELOPMENT OF ALKALI FELDSPAR REPLACEMENT STRUCTURES: INFLUENCE OF LITHOLOGY AND FLUID INFLUX

3.1 INTRODUCTION

Within the previous chapter, the formation of myrmekites within granitic rocks of the PSZ was examined and the following was established: (1) myrmekites developed preferentially along high-strain grain boundaries, and in contact with plagioclase feldspar, indicated that they form syn-kinematically and that stress and proximity to reacting feldspar were important within a fluid-poor environment; (2) myrmekite formed due to closed-system reactions involving relict plagioclase and newly formed muscovite; (3) evolving myrmekite morphologies suggests their continued growth during deformation and (4) myrmekite facilitated deformation and aided in the creation of a weaker deforming polymineralic matrix. However, the PSZ is not just hosted within granitic rocks and it is important to consider whether myrmekite developed within surrounding lithologies. Within these surrounding rocks, other strain-induced alkali feldspar replacement textures such as flame perthites, are also developed. By evaluating the co-occurrence of myrmekite and other syn- to post-kinematic microstructures, the evolution of deformation within different rock units allows for an investigation into how fluid-influx and strain are partitioned over time.

A starting point for this analysis is a look into how these microstructures are developed within similar shear zones. The Grenville Front Tectonic Zone in Ontario, Canada is a crustal-scale reverse shear zone, deformed under retrograde upper amphibolite to sub-greenschist conditions (Haggart *et al.*, 1993) comparable to the PSZ. Pryer and Robin (1996) found myrmekites developed parallel to the S-plane within S/C mylonites deformed at amphibolite facies conditions, with flame perthite occupying the same position at low- to medium grades but rarely together. Flame perthite development is a strain-induced partial retrograde replacement of alkali feldspar through alkali exchange involving the internal recycling of Na and K components derived from various reactions involving plagioclase (Pryer and Robin, 1995, 1996). The dependence of flame orientation and growth on the local maximum

compressive stress, which varies, the normal perthite crystallographic plane (the Murchison plane) and the availability of water during deformation accounts for the variability in abundance and orientation of flame perthite (Pryer and Robin, 1996; Vernon, 1999).

Most studies into deformation-induced myrmekite have concentrated on their occurrence within granitic mylonites (eg. Simpson, 1985; Simpson and Wintsch, 1989; Stel and Breedveld, 1990; Tsurumi *et al.*, 2002; Menegon *et al.*, 2006; Ceccato *et al.*, 2018) with a small number of studies looking into myrmekites developed within metapelitic or previously deformed rocks (eg. Phillips *et al.*, 1972; Nold, 1984; Vernon, 1999; Harlov and Wirth, 2000). The occurrence of myrmekites developed within different rock units interleaved on a small scale with the metagranite gneiss of chapter 2 allows us to investigate differences in myrmekite evolution and associated deformation fabrics, while controlling for bulk P-T conditions. Combining this with an attempt to establish the timing relationships between replacement structures will allow us to investigate the control lithology and fluid influx has on microstructure development and, more broadly, on the evolution of rocks within the PSZ.

3.2 FIELD SITE CONTEXT

The mylonites and protomylonites examined in Chapter 2 are developed within a megacrystic granite, which had intruded into a migmatitic biotite gneiss and a quartzo-feldspathic gneiss, before the whole sequence was deformed by the PSZ (Fig. 2.1a). Exposures within the drag-folds of the PSZ show the clear intrusive relationship between the megacrystic granite and the migmatitic biotite gneiss (Fig. 3.1a). Within the mylonite pavement of the field site, contacts between the units are commonly the site of pegmatite intrusions and this is where deformation is localised. Mylonite zones developed within the megacrystic granite are much thinner (cm-scale) while mylonites developed within the migmatitic biotite gneiss span several meters. Along contacts between the metagranite and the migmatitic biotite gneiss, pervasive chlorite retrogression is limited to the latter (Fig. 3.1b). The quartzo-feldspathic gneiss has been extensively intruded by pegmatites, with mylonites progressively

dismembering these pegmatites, particularly at contacts with the migmatitic biotite gneiss (Fig. 3.1c). Late pegmatite intrusions also occur which cross-cut the foliation.

3.2.1 Migmatitic Biotite Gneiss

Migmatitic biotite gneiss is a rock unit that within less sheared outcrops preserves the stromatic cm-scale migmatitic banding clearly visible outside the PSZ (Fig. 3.1d). It correlates to the migmatitic grey gneisses of the regionally mapped Umeis Gneiss of the Orange River Group, where the strong migmatitic fabric was acquired during the amphibolite facies Namaqua Orogeny and predates shearing. This earlier fabric has been re-oriented and reworked during PSZ deformation. The migmatitic biotite gneiss is very heterogenous in outcrop (Fig. 3.1e) with a strong banded fabric defined by varying proportions of the main constituent minerals. The banding varies from strongly biotite- and muscovite-rich with a strong schistosity that in places shows a crenulation cleavage (Fig. 3.1f) to dominantly quartz and feldspar rich layers with a dominantly gneissic fabric. The orientation of the compositional banding, particularly of the leucosomes, and the parallel alignment of the platy biotite grains define the main foliation (Fig. 3.1g). Elongate aggregates of quartz and plagioclase feldspar, and less commonly hornblende, define the stretching lineation.

3.2.2 Quartzo-feldspathic Gneiss

Within the drag-folded wall rocks of the PSZ, the quartzo-feldspathic gneiss occurs as thick (>100m) homogeneous packages of rock that weather positively compared to surrounding lithologies. The gneiss most likely forms part of the quartz-feldspar gneisses of the Umeis Gneiss of the Orange River Group. It has an equigranular fine- to medium grained texture and is composed of dominantly quartz, plagioclase, alkali feldspar, biotite and minor chlorite. The quartzo-feldspathic gneiss has a weak compositional banding of quartz- and feldspar-rich layers to more biotite-rich compositions. The compositional layering and the interconnected biotite folia define the foliation. Elongate aggregates of quartz and feldspar define the stretching lineation (Fig. 3.1h).



Fig. 3.1 *Preceding page. Field photos of the migmatitic biotite gneiss and the quartzo-feldspathic gneiss. a) Intrusive contact between the megacrystic granite and the migmatitic biotite gneiss within the drag folded wallrocks. b) Contact between the deformed granite, below, and the migmatitic biotite gneiss, top, is the site of increased chlorite retrogression within the migmatitic biotite gneiss. c) Extensively developed mylonites dismember pegmatites intruding into the quartzo-feldspathic gneiss at the contact with the migmatitic biotite gneiss. d) Preserved stromatic cm-scale migmatitic banding preserved within the drag-folded wallrocks. e) Complex compositional banding of leucosomes and melanosomes of the migmatitic biotite gneiss. f) Micaceous melanosomes develop a crenulation cleavage. g) Mylonite zones developed adjacent to preserved ptigmatically folded leucosomes. h) Equigranular fine- to medium grained texture of the quartzo-feldspathic gneiss with the stretching lineation defined by elongate aggregates of quartz and feldspar*

3.3 PETROGRAPHY

The compositional homogeneity of the quartzo-feldspathic gneiss makes a description of the transition from protomylonite to mylonite a worthwhile exercise, as this would likely be representative of the general deformation pathway of this unit. In contrast, the petrographic description of the migmatitic biotite gneiss is limited to the description of a single set of thin-sections of a mylonite which truncates ptigmatically-folded leucosomes of a biotite-rich expanse of this unit. Alkali feldspar replacement microstructures are presented as a separate section on each rock. A brief overview of the thin-section scale kinematic indicators developed within these units is also provided.

3.3.1 Rock types

3.3.1.1 *Migmatitic Biotite Gneiss*

The sheared micaceous melanosomes of the migmatitic biotite gneiss are dominated by a well-developed S-C fabric defined by lozenge shaped muscovite fish that are truncated along C-planes (Fig. 3.2a). Elongate quartz aggregates contribute to the fabric and can be traced for hundreds of microns within thin sections (white arrow Fig. 3.2a). There is some mm-scale compositional banding (Fig. 3.2b) separating more quartzo-feldspathic bands from zones with predominantly muscovite fish in a homogenous biotite-rich, fine-grained matrix. Fe-oxide trails, which commonly nucleate on muscovite tips, define a late S-C' fabric (Fig. 3.2c). Accessory minerals include zircon, apatite, garnet and REE oxides.

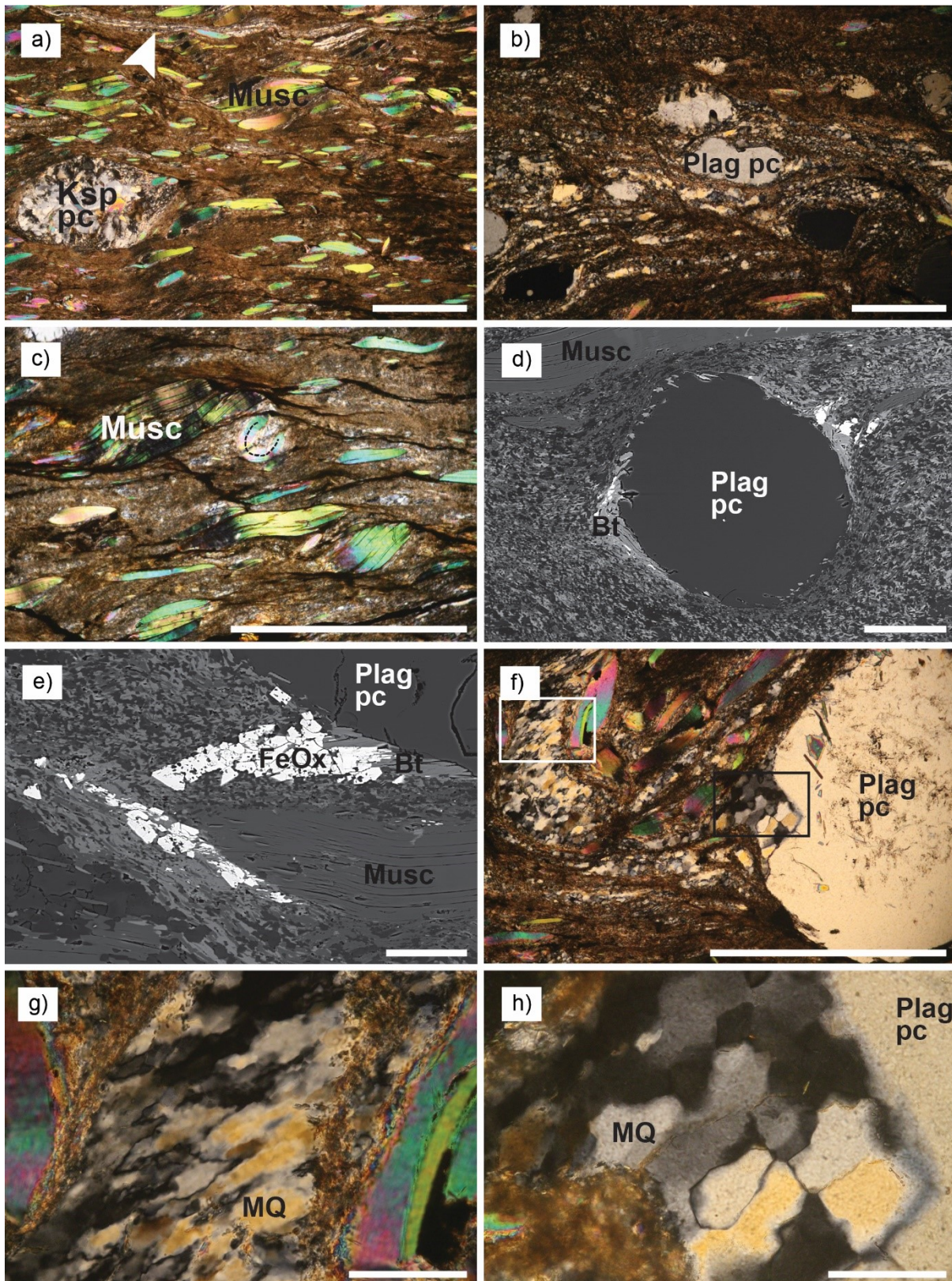


Fig. 3.2 Preceding page. SEM-BSE images and XPL photomicrographs of various microstructural features of the migmatitic biotite gneiss. Unless otherwise stated, foliation and lineation are horizontal. Scale bar in figures a-c) and f) is 1 mm. a) Augen shaped alkali feldspar porphyroclasts set within the S-C fabric of the micaceous melanosomes. b) Small-scale compositional banding from more muscovite fish rich zones to more quartzofeldspathic bands. c) Late S-C' fabric defined by Fe-oxide trails which commonly nucleate on the tips of muscovite fish. Stippled black line indicates a dextrally rotated single muscovite fish. d) Biotite preferentially precipitating within feldspar pressure shadows. Scale bar is 100 μm . e) Biotite closely associated with blocky Fe-oxide. Scale bar is 50 μm . f) Folded quartz aggregates well developed behind a large plagioclase porphyroclast. g) XPL photomicrograph of the same area as the white rectangle in f) showing quartz grains with a strong grain-shape preferred orientation oblique to the foliation. Scale bar is 100 μm . h) XPL photomicrograph of the same area as the black rectangle in f) showing coarser and more polygonal quartz grains. Scale bar is 100 μm . FeOx: Fe-oxide

Muscovite fish make up 15 - 30% of the modal abundance and isolated augen-shaped alkali feldspar and plagioclase porphyroclasts within the micaceous matrix contribute 10 – 15% to the rock volume. The micaceous matrix has a slight green pleochroism in plane polarised light indicating the presence of fine-grained chlorite. The mica fish range in size from 20 μm to over 1.5 mm long, have an average of 160 μm in length and are highly elongate with an average AR of 4.4 (n=244). The largest of these are strongly folded with a dominantly clockwise rotation (dashed line Fig. 3.2c). The muscovite typically splits along the hold-hinges of tight folds. These large grains have a sweeping undulose extinction that is less prevalent in smaller mica fish. Biotite occurs within the matrix as elongate 10-30 μm in length grains. Biotite preferentially occurs along the tips of mica fish and along the strain shadows of feldspar porphyroclasts (Fig. 3.2d). The biotite grains developed along strain shadows of minerals can reach up to 100 μm in length and are closely associated with blocky Fe-oxide (Fig. 3.2e). Quartz occurs dominantly as folded aggregates which are commonly 30 μm to 300 μm thick (Fig. 3.2f). The grains within these aggregates have a strong grain-shape preferred orientation, which is oblique to the foliation (Fig. 3.2g), as well as a strong lattice preferred orientation. Recrystallised grains and subgrains are about the same size, approximately 10 μm to 20 μm thick and 35 μm to 60 μm in length. Quartz grains developed along the strain shadows of large feldspar porphyroclasts, and hence presumably protected from deformation, are larger (40 μm to 80 μm across), polygonal with well-defined grain boundaries and with no grain-shape preferred orientation (Fig. 3.2h). Plagioclase occurs

as rounded porphyroclasts which range in size from 160 μm to 600 μm (Fig. 3.3a). There are a few isolated grains that can reach up to 3.5 mm in size and these large grains contain abundant quartz and mica inclusions (Fig. 3.3b). Plagioclase grains are sub-rounded to elongate with their long axes parallel to or at a slight angle to the foliation (Fig. 3.3c). Some of the larger grains show undulose extinction and deformation twinning, recognised by their tapering, non-through going twins. Most grains are strongly fractured (Fig. 3.3d), with minimal sericite alteration.

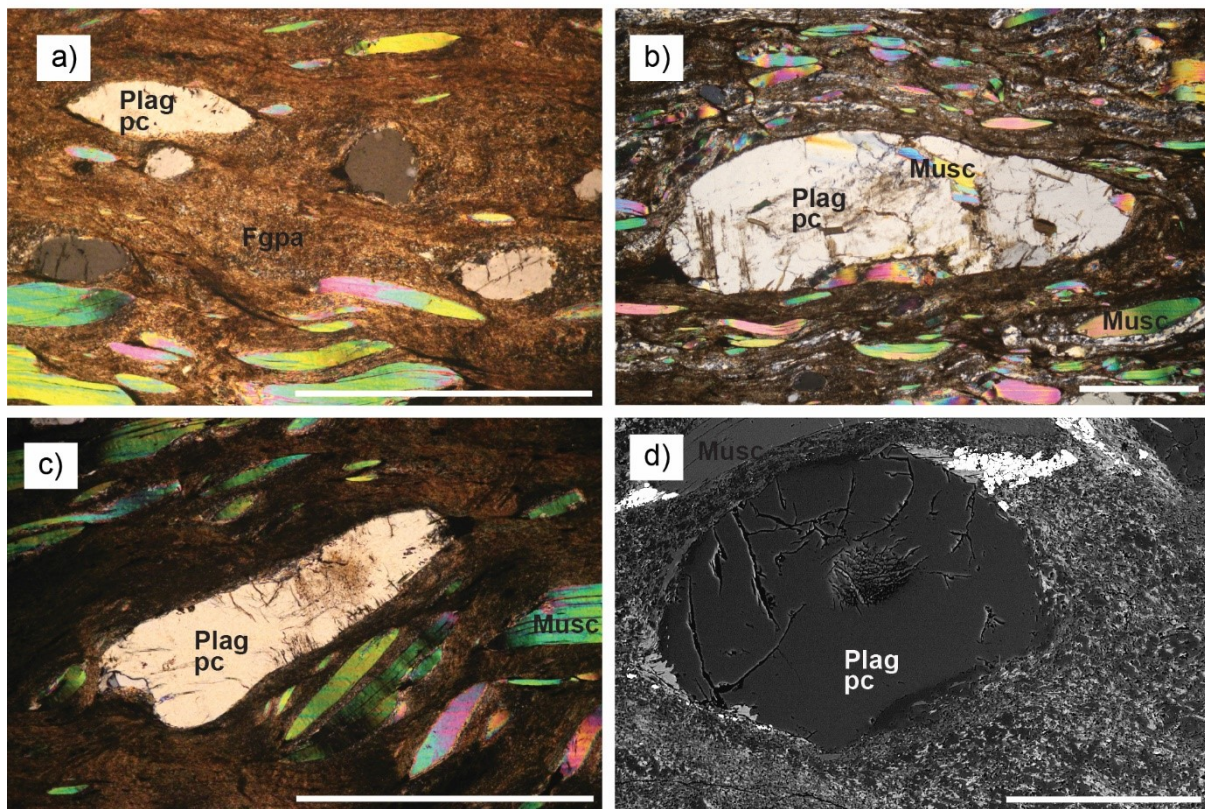


Fig. 3.3 XPL photomicrographs and SEM-BSE images of plagioclase microstructures within the migmatitic biotite gneiss. Scale bar is 1 mm in figures a-c) and in figure d) it is 200 μm . a) Variably sized plagioclase clasts with smooth grain boundaries to the mica-rich matrix. b) Large plagioclase porphyroclast with inclusions of tabular muscovite. c) Most plagioclase grains are sub-rounded and elongate with long axes parallel or inclined to the foliation parallel to muscovite fish. d) BSE-SEM image of a fractured plagioclase porphyroclast

3.3.1.2 *Quartzo-feldspathic Gneiss*

Protomylonite: The protomylonitic fabric is defined by thick (30 μm to 300 μm) quartz aggregates wrapping around rounded feldspars separated by thin discontinuous zones of fine-grained polymineralic matrix (Fig. 3.4a). Apatite and zircon are present as accessory minerals. Biotite makes up 10-15% of the rock volume and occurs as a weakly interconnected network anastomosing around feldspars and quartz aggregates. The biotite grains occur as elongate tabular laths and are highly pleochroic yellow to orange-brown. A large proportion of the biotite is retrogressed to strongly pleochroic green chlorite (Fig. 3.4b). Elongate fibrous muscovite also contributes to the foliation. The muscovite occurs mostly within the fine-grained polymineralic matrix between quartz aggregates (Fig. 3.6c). Quartz aggregates make up 40-45% of the rock and they form continuous ribbons which can be traced for hundreds of microns. The size of the quartz grains within these aggregates is strongly dependant on the thickness of the ribbons, with larger ribbons having larger grain sizes (Fig. 3.4c). The grain boundaries within these ribbons are amoeboid and irregular, but sharply defined (Fig. 3.4d). Some of the largest grains show undulose extinction and some subgrain development but the smaller grains are strain free.

Plagioclase porphyroclasts within the protomylonite make up 15 – 25 % of the rock volume, are rounded in shape and range from 50 μm to 1.2 mm, with an average grain size of $\sim 450 \mu\text{m}$. There are locally developed zones of increased plagioclase alteration, with alteration particularly well-developed along twin planes (Fig. 3.4e). The boundary between altered and unaltered zones is sharp (Fig. 3.4f). SEM-BSE images (Fig. 3.4g) reveal this alteration to be a complex mix of phases, including alkali feldspar, muscovite and albite. The altered plagioclase is full of pores while the unaltered plagioclase is not (Fig. 3.4f). Alkali feldspar porphyroclasts make up 10-15% modal abundance and are rounded and elongate in the direction of the foliation. They range in size from 40 μm to 1.8 mm, with an average grain size of $\sim 350 \mu\text{m}$. Alkali feldspar, besides precipitating within fractures in plagioclase, also precipitates within the strain shadows of feldspar porphyroclasts (Fig. 3.4h). These strain shadows are long ($>300 \mu\text{m}$) and contribute to the rock having a banded appearance under SEM-BSE imaging.

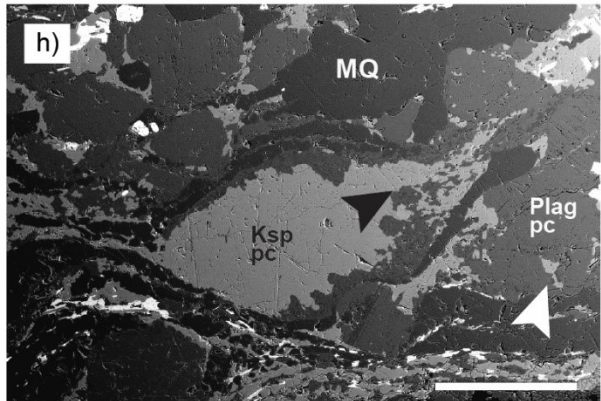
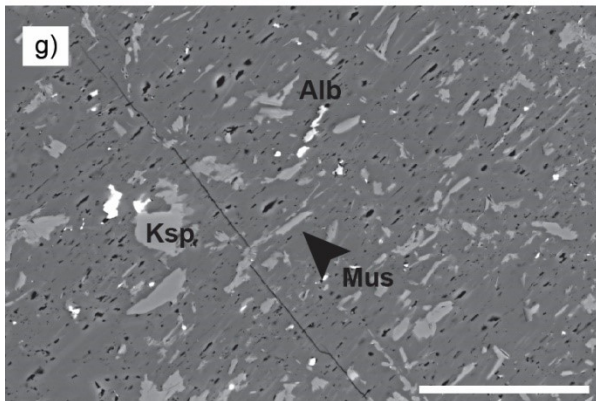
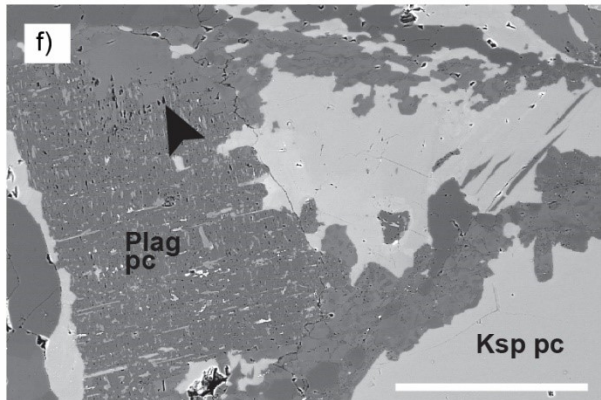
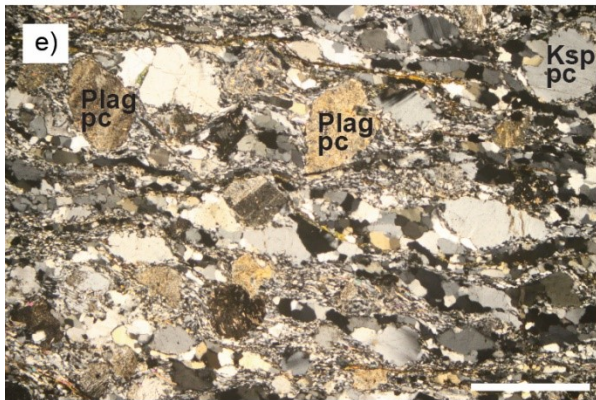
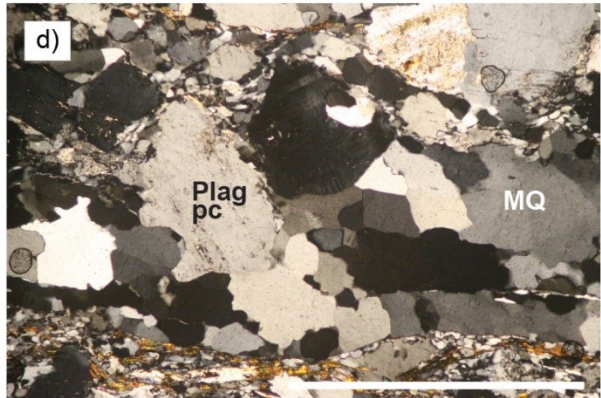
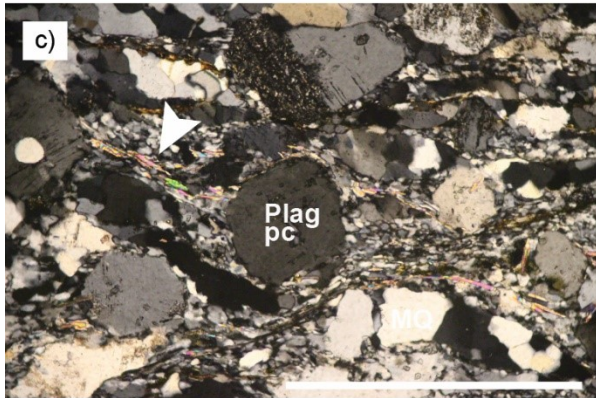
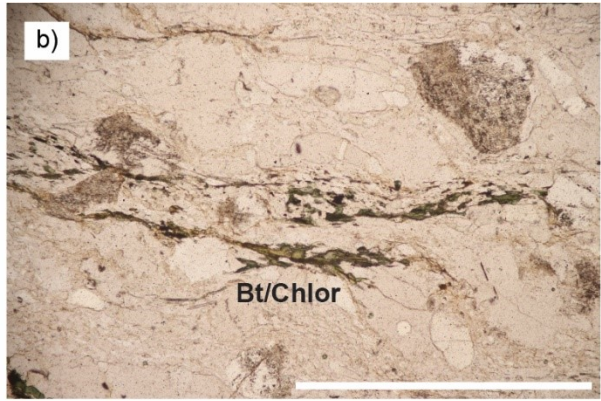
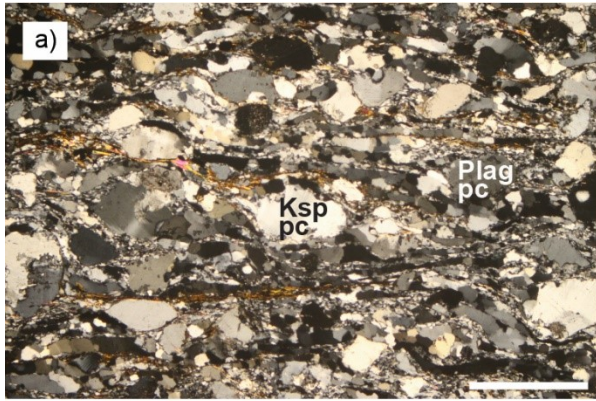


Fig. 3.4 Preceding page. XPL and PPL photomicrographs and SEM-BSE images of various microstructural features of the protomylonitic quartzo-feldspathic gneiss. Scale bar is 1 mm in figures a-e). a) XPL photomicrograph of quartz aggregates of variable thickness wrapping around feldspar porphyroclasts. b) PPL photomicrograph of elongate laths of biotite retrogressed to pleochroic green chlorite. c) XPL photomicrograph showing quartz grain sizes varying depending on the thickness of the monomineralic quartz aggregates which they are hosted in. White arrow indicates foliation parallel muscovite. d) XPL photomicrograph showing quartz grain boundaries are amoeboid and irregular. e) XPL photomicrograph of plagioclase grains showing significant seritisation. f) SEM-BSE image of altered plagioclase with black arrow indicating the sharp boundary between altered and unaltered plagioclase. Scale bar is 200 μm . g) SEM-BSE image of altered plagioclase. Scale bar is 50 μm . h) SEM-BSE image of alkali feldspar precipitating within the strain shadows of feldspars (black arrow) and within cracks in plagioclase feldspar (white arrow). Scale bar is 500 μm . Alb: Albite. Chlor: Chlorite

Mylonite: Within mylonites hosted within the quartz-feldspathic gneiss, the fabric of the rock is dominated by the fine-grained polymineralic matrix with isolated feldspar porphyroclasts. Monomineralic aggregates make up less than 5% of the modal mineralogy (white arrow Fig. 3.5a). Biotite grains within the matrix are small (50-100 μm) and tabular in shape, which suggests they are newly crystallized. Plagioclase porphyroclasts make up 10-15% of the modal percentage. Plagioclase porphyroclasts range in size from 40 μm to 800 μm , with an average grain size of 250 μm . Grains are well rounded and moderately elongate with an average AR of 1.7 (n=235), with the long axes of the porphyroclasts randomly distributed with regards to the mylonitic foliation (Fig. 3.5b). Most of the plagioclase grains in the mylonite are untwinned and do not show significant alteration to sericite. Many grains are fractured (Fig. 3.5c), with micas infilling the larger through going fractures or alkali feldspar precipitating within intragranular cracks (Fig. 3.5d). Alkali feldspar porphyroclasts within the mylonite are reduced to less than 1% of the modal abundance, have an average grain size of 200 μm and rarely reach more than 800 μm in length. They are elongate and more consistently orientated in the direction of the foliation than the plagioclase porphyroclasts (Fig. 3.5e). Most grains show undulose extinction (Fig. 3.5f). While not as extensively developed as within the protomylonite, alkali feldspar commonly forms tails on feldspar porphyroclasts (3.5d).

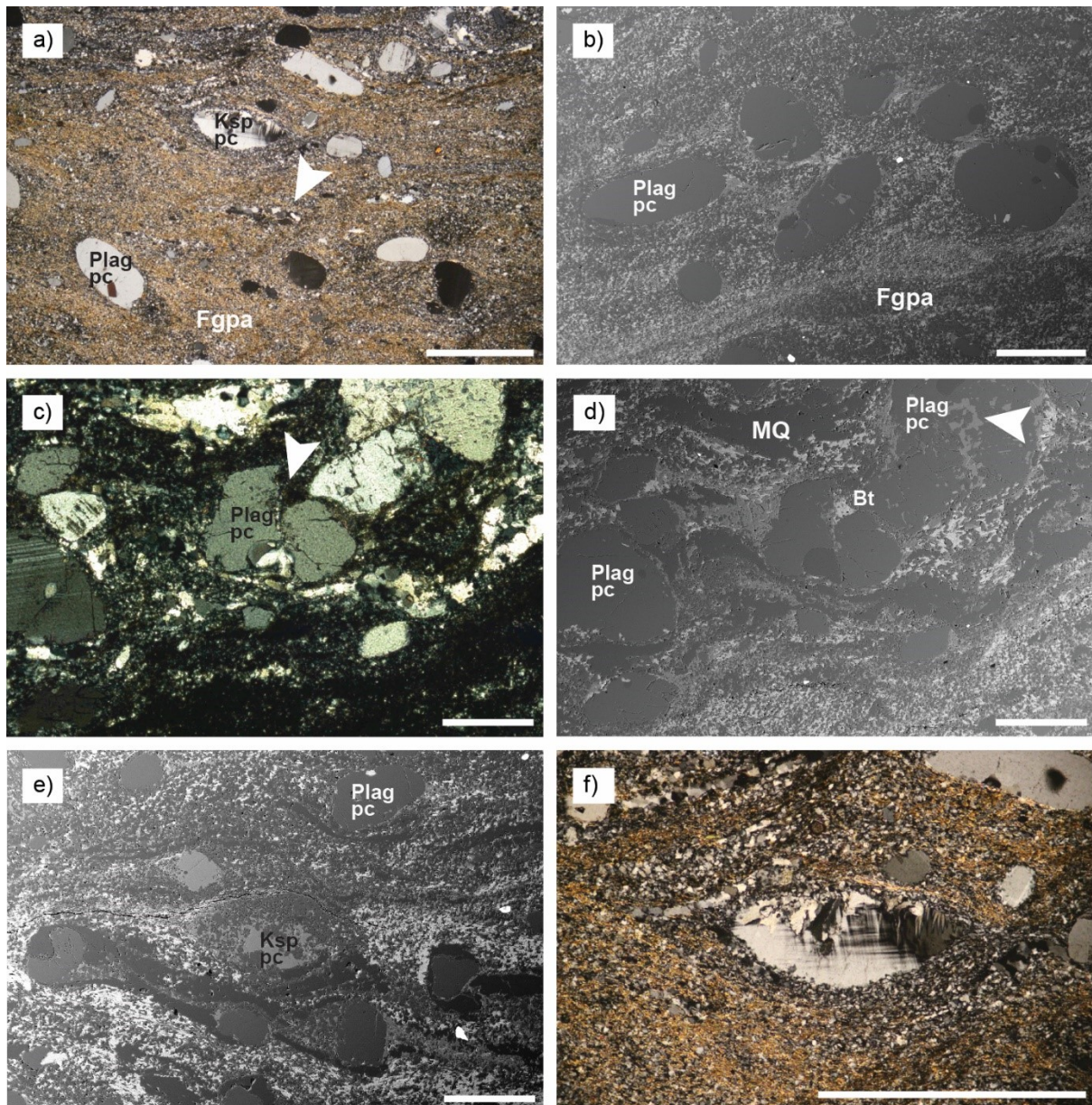


Fig. 3.5 XPL and PPL photomicrographs and SEM-BSE images of various microstructural features of mylonites hosted within the quartzo-feldspathic gneiss. a) XPL photomicrograph showing isolated feldspar porphyroclasts within the matrix, with limited development of monomineralic quartz aggregates (white arrow). Scale bar is 1 mm. b) SEM-BSE image of rounded, moderately elongate plagioclase porphyroclasts randomly orientated within the matrix. Scale bar is 500 μm . c) XPL photomicrograph with white arrow indicating a large offset within a fractured plagioclase grain. Scale bar is 500 μm . d) SEM-BSE image of the same area as c) showing the fracture is the site of biotite growth. Intragranular fractures within plagioclase show precipitation of alkali feldspar (white arrow). Scale bar is 500 μm . e) SEM-BSE image of rare alkali porphyroclasts orientated parallel to the foliation. Scale bar is 500 μm . f) XPL photomicrograph showing undulose extinction within an elongate alkali feldspar porphyroclast. Scale bar is 1 mm

3.3.2 Feldspar and myrmekite microstructures

3.3.2.1 *Migmatitic biotite gneiss*

Within the migmatitic biotite gneiss, alkali feldspar occurs as complex augens that range in size from 360 μm to 1.9 mm, with an average length of 850 μm . The larger grains show strong undulose extinction and contain an abundance of mica and round quartz inclusions (Fig 3.6a). Alkali feldspar is never found in contact with the polymineralic matrix. All alkali feldspar porphyroclasts show a rim of albitic plagioclase (Fig 3.6b) and some porphyroclasts are only composed of albitic plagioclase, with only interstitial amounts of alkali feldspar (Fig. 3.6c). Alkali feldspar porphyroclasts also commonly have tails of mostly albitic plagioclase. EDS analyses reveal these albitic plagioclase rims to be mostly Na-rich, with between 0.5 and 1.9 weight % Ca. These rims are fine-grained and are compositionally heterogeneous on a very small scale as revealed by varying signal intensities under high-contrast SEM-BSE imaging (Fig 3.6d). The grains within the albitic rims have variable crystallographic orientations, with some groups of grains within the same rim going extinct at the same time.

Flame perthite is extensively developed within most clasts (Fig. 3.6e). Some of the alkali feldspars have albitic cryptoperthite exsolutions, following the definition of Parsons *et al.* (2005) which are less than 1 μm thick. Flame perthites are often, but not always, parallel to these cryptoperthites (Fig. 3.6f). EDS analyses reveal the flames to be near pure albite in composition, with no Ca detectable or only very minor amounts of Ca (<0.4 weight % Ca). Flames make up between 5 and 50 % of the alkali feldspar porphyroclasts. Flame perthites within the same grain have the same crystallographic orientation but do not have the same crystallographic orientation as the host alkali feldspars within which they are hosted, with an average 5 – 10° difference. The flames are commonly 3 to 30 μm thick and are more abundant towards the rims of the porphyroclasts, with a tapering geometry. The flames also bifurcate in some places. The flames commonly nucleate on inclusions within the alkali feldspar such as quartz or muscovite. The orientation of the flames varies although they are generally orientated perpendicularly to the S-plane of the mylonitic fabric of these S/C mylonites.

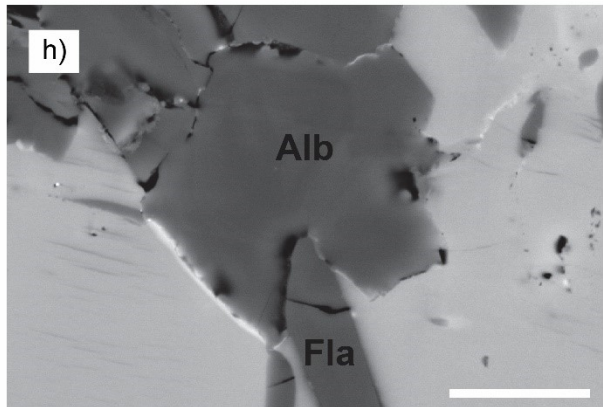
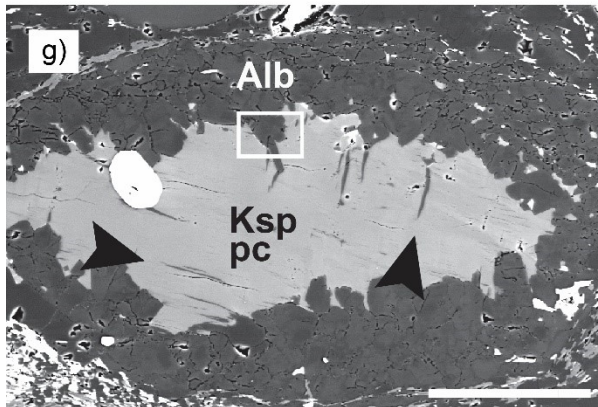
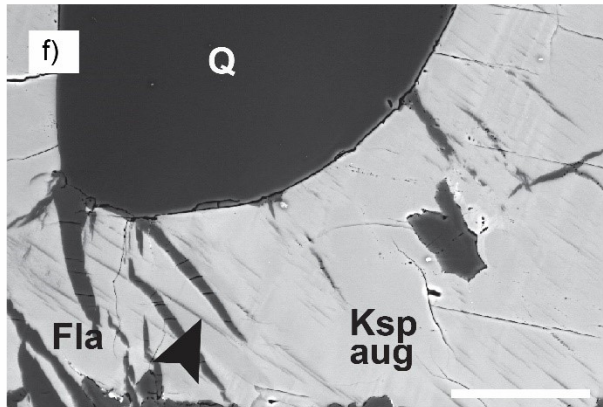
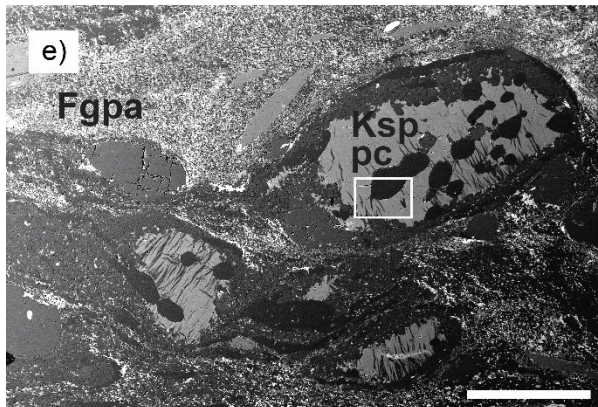
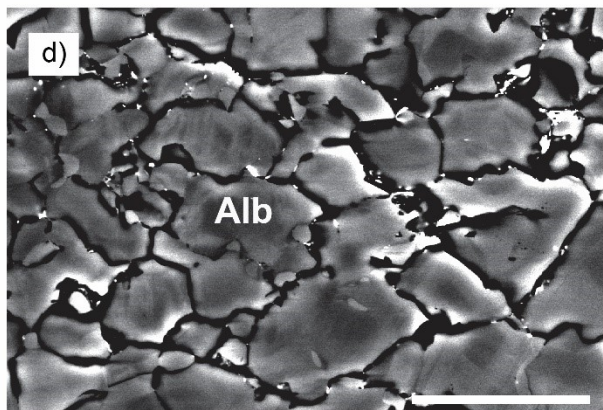
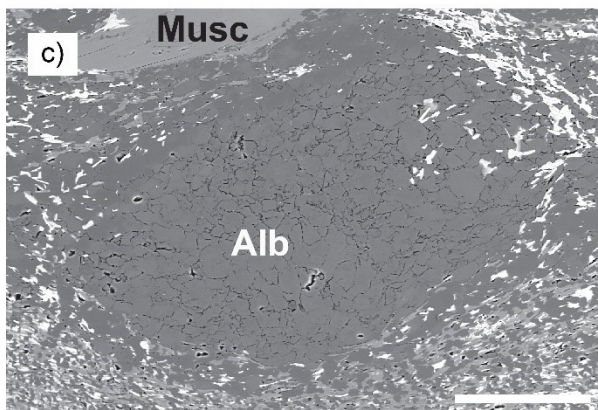
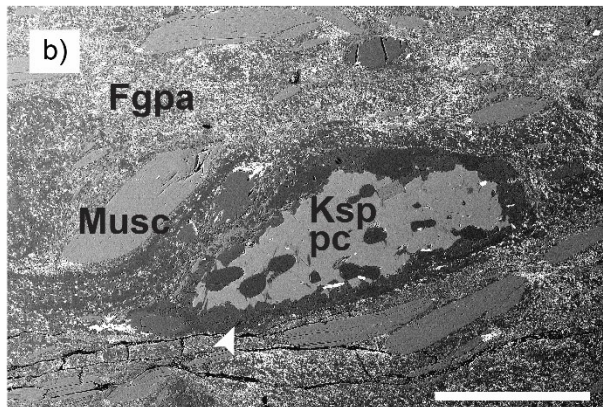
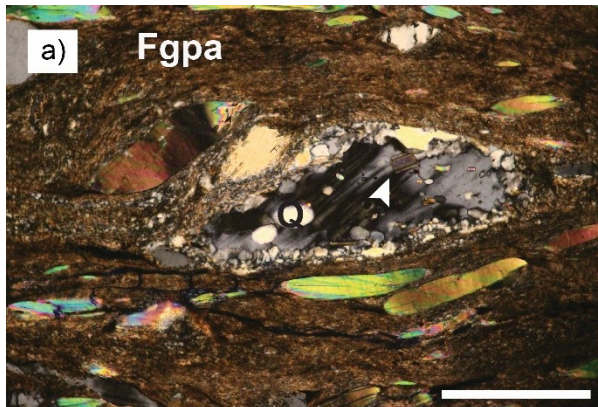


Fig. 3.6 SEM-BSE images and an XPL photomicrograph (a) of albitic rims and flame perthites developed within alkali feldspars of the migmatitic biotite gneiss. a) XPL photomicrograph shows alkali feldspar augens to contain many inclusions of quartz and muscovite (white arrow) and show undulose extinction. Scale bar is 500 μm . b) SEM-BSE image of approximately the same area as a) show the alkali feldspar augen to be completely mantled by an albitic plagioclase rim (white arrow). c) Alkali feldspar completely consumed by fine-grained albitic plagioclase. Scale bar is 100 μm . d) Close-up of the albitic plagioclase replacement in c) showing the compositional heterogeneity of the albitic rims. Scale bar is 20 μm . e) Various alkali feldspar augens with varying proportions of flame perthite which is generally orientated sub-perpendicular to the mylonitic fabric. Scale bar is 500 μm . f) Same area as the white rectangle in e) showing the relationship between cryptoperthites (black arrow) and flame perthites. Scale bar is 50 μm . g) Two orthogonally developed sets of albite flames (black arrows). Scale bar is 100 μm . h) Same areas as the white rectangle in g) showing flame perthite protruding into albitic rim. Scale bar is 10 μm . Fla: Flame perthite

Within most grains, there is a minor component of an orthogonally developed set of flame perthites (Fig. 3.6g). EDS analyses reveal these perpendicularly developed flames to have the same chemistry as the dominant set. Where flames and perthite rims are found to intersect, the flames appear to protrude into the albitic rims (Fig. 3.6h).

Although complicated by the overprinting albitic rims, recognisable myrmekite lobes are developed along the crystal faces perpendicular to the S-plane within the S/C fabric of the migmatitic biotite gneiss (Fig. 3.7a). The long axes of the best developed quartz rods are parallel to the direction of most compressive stress as within the metagranite of chapter 2 (Fig. 3.7b). Where several myrmekite lobes are developed, the plagioclase within each lobe has the same crystallographic orientation, but the crystallographic orientation varies slightly from lobe to lobe (Fig. 3.7c). SEM-BSE images reveal that cracks follow the grain boundaries between myrmekite lobes (Fig. 3.7d, e). Recognisable myrmekites, as indicated by a plagioclase/quartz intergrowth, are not commonly found along the short ends of alkali feldspar porphyroclasts, which are instead composed of fine-grained albitic plagioclase (Fig. 3.7f). EDS analyses reveal the myrmekite plagioclase to generally be more Ca-rich than these albitic rims, with between 1.9 and 2.9 weight % Ca.

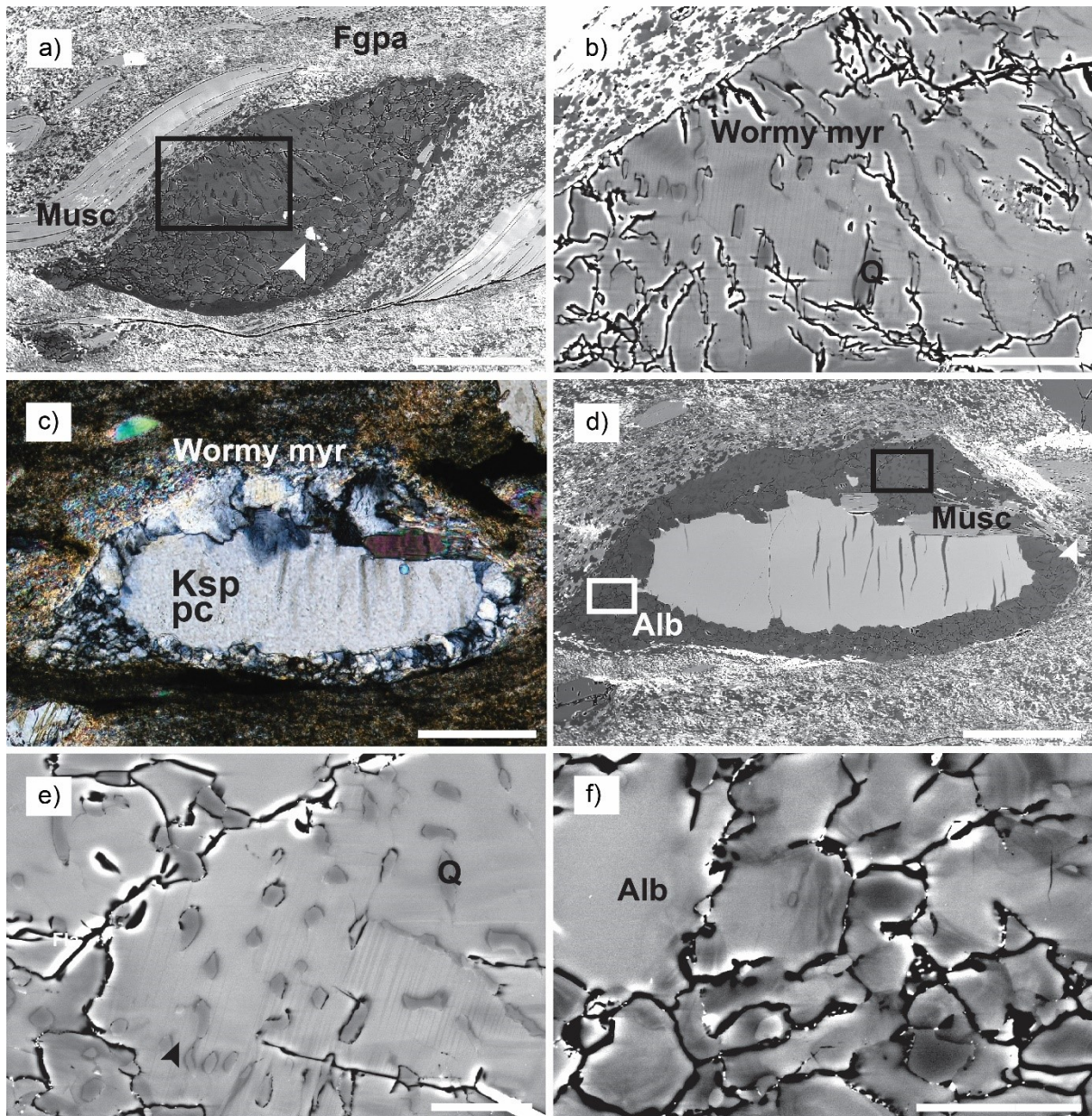


Fig. 3.7 SEM-BSE images and an XPL photomicrograph (c) of myrmekites developed within the migmatitic biotite gneiss. a) Sigmoidal shaped alkali feldspar grain completely replaced by myrmekite and albitic plagioclase rims with white arrow indicating interstitial alkali feldspar. Scale bar is 200 μm . b) Close up of the wormy myrmekites in a) showing the elongation of quartz rods perpendicular to the grain boundary. Scale bar is 50 μm . c) XPL photomicrograph of an alkali feldspar porphyroblast replaced by many lobes of myrmekite which each have a slightly different crystallographic orientation. Scale bar is 200 μm . d) SEM-BSE image of the same grain as in c) showing wormy myrmekites developed along shortening axes while albitic plagioclase occurs along short ends of the grain. Scale bar is 200 μm . e) Same area as black rectangle in d) showing myrmekites and that cracks follow grain boundaries of separate lobes. Scale bar is 20 μm . f) Same area as white rectangle in d) showing no recognisable myrmekite structure along the short-sides of alkali feldspar porphyroblast. Scale bar is 20 μm

3.3.2.2 *Quartzo-feldspathic gneiss*

Myrmekites developed within the quartzo-feldspathic gneiss show many of the same features as the metagranite. Myrmekite lobes are preferentially developed along the high-strain sides of elongate porphyroclasts (Fig. 3.8a). The myrmekites developed the furthest inwards towards the host alkali feldspar are of the wormy myrmekite type (Fig. 3.8b). The majority of the myrmekite developed is however of the recrystallised type and it is developed along the rims of alkali feldspar (Fig. 3.8c). The recrystallised myrmekite becomes progressively dismembered and incorporated into the alkali feldspar rich tails formed adjacent to host porphyroclasts (Fig. 3.8d).

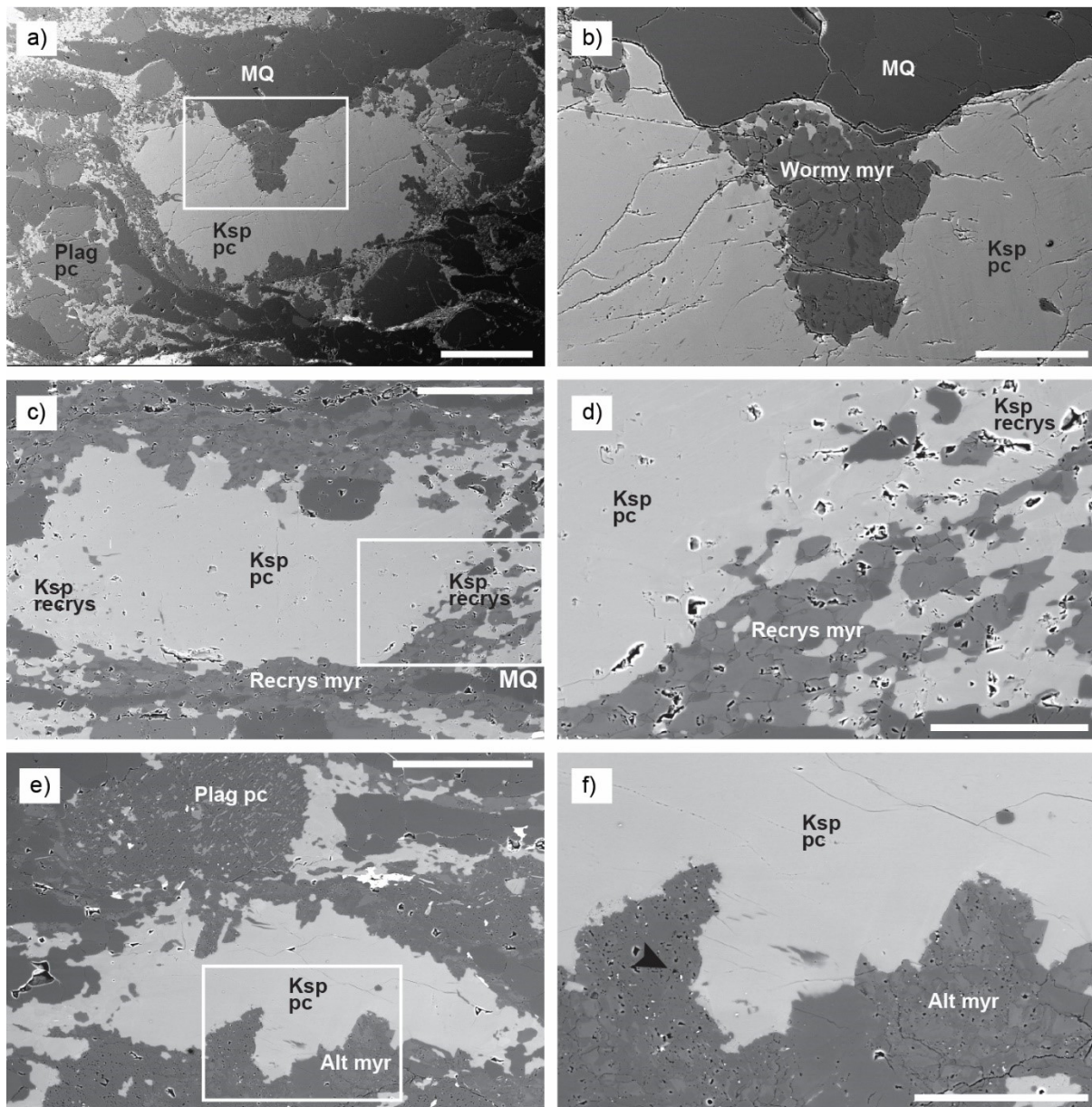


Fig. 3.8 Preceding page. SEM-BSE images of myrmekite developed within the quartzo-feldspathic gneiss. a) Alkali feldspar porphyroclast showing myrmekite preferentially developed on the sides parallel to the mylonitic foliation. Scale bar is 500 μm . b) Same area as the white rectangle in a) showing a wormy myrmekite texture. Scale bar is 200 μm . c) Recrystallised myrmekite developed along the rims of alkali feldspar. Scale bar is 200 μm . d) Same area as the white rectangle in c) showing how recrystallised myrmekite is dismembered and incorporated into alkali feldspar rich tail. Scale bar is 100 μm . e) Altered myrmekite situated close to altered plagioclase porphyroclasts. Scale bar is 200 μm . f) Same area as the white rectangle in e) showing altered myrmekites to be full of pores (black arrow). Scale bar is 100 μm . Alt myr: Altered myrmekite

Mostly within the protomylonites of the quartzo-feldspathic gneiss, some of the myrmekites are strongly altered and these altered myrmekites are always situated close to similarly altered plagioclase porphyroclasts (Fig. 3.8e). The altered myrmekites are full of pores (Fig. 3.8f). There are few flame perthites developed within alkali feldspars of the quartzo-feldspathic gneiss.

3.3.3 Kinematic Indicators

The migmatitic biotite gneiss hosts a range of kinematic indicators that are overwhelmingly dextral in nature. The micaceous melanosomes show a well-developed S-C fabric indicating a dextral sense of shear (Fig. 3.9a). Some parts of the rock show that a later S-C' fabric, with the C' shears typically truncating the tips of the lenticular mica fish (Fig. 3.9b). The composition of these C' shears is much more Fe-oxide rich than the rest of the matrix. The micaceous portions of the rock are dominated by lenticular mica fish orientated at an angle to the main foliation (Fig. 3.9a). Some large individual mica fish in places show a clock-wise fold direction (Fig. 3.9c). Ptygmatically folded quartz aggregates also have a fold-asymmetry which indicates a dextral vergence (Fig. 3.9d). The individual grains within quartz aggregates are elongate and are orientated oblique to the foliation, indicating a dextral sense of shear (Fig. 3.9e). Relict alkali feldspar augens almost completely replaced by myrmekite and albitic plagioclase form sigmoidal polycrystals orientated at an angle to the mylonitic foliation (Fig. 3.9f).

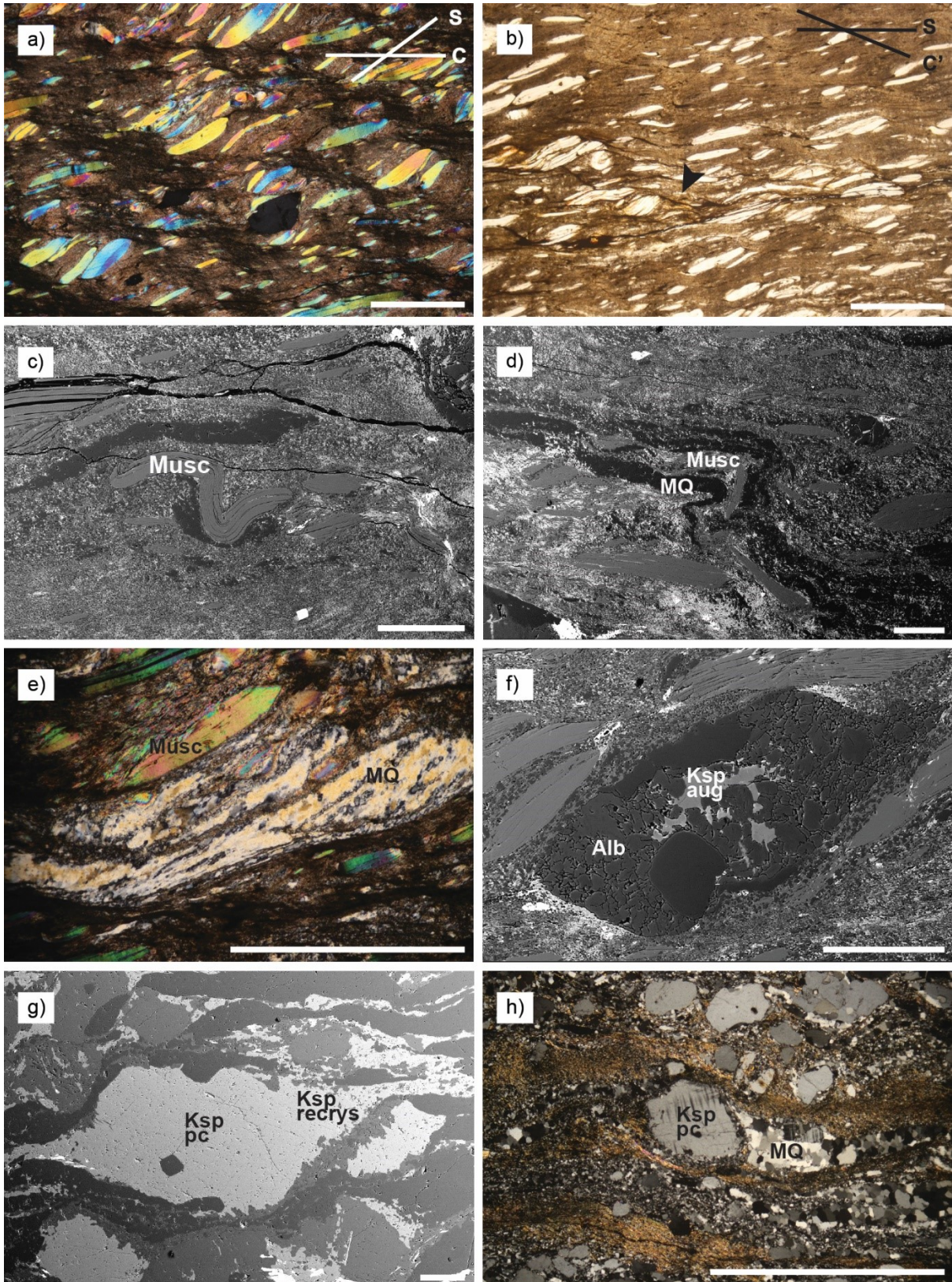


Fig. 3.9 Preceding page. XPL and PPL photomicrographs and SEM-BSE images of various dextral kinematic indicators developed within the migmatitic biotite gneiss (a-f) and the quartzo-feldspathic gneiss (g-h). Scale bar is 1 mm for images a, b and h and 200 μm for the rest. a) XPL photomicrograph showing a well-developed S-C fabric with C-planes truncating the tips of oblique lenticular muscovite fish. b) PPL photomicrograph showing a late S-C' fabric developed with the C' fabric composed of dominantly iron oxide (black arrow). c) SEM-BSE image of a dextrally rotated muscovite fish. d) SEM-BSE image of dextrally rotated layers of monomineralic quartz aggregate and muscovite fish. e) XPL photomicrograph showing quartz grains within monomineralic aggregates that are elongate and oblique to the foliation. f) SEM-BSE image of a sigmoidal polycrystal composed of alkali feldspar and albitic plagioclase orientated oblique to the foliation. g) SEM-BSE image of an alkali feldspar porphyroclast which has developed asymmetrical alkali feldspar pressure shadows. h) XPL photomicrograph of dextrally rotated quartz-rich wings developed on an alkali feldspar porphyroclast

While kinematic indicators are not as well developed in the quartzo-feldspathic gneiss as the migmatitic biotite gneiss, pressure shadows surrounding feldspar porphyroclasts within the quartzo-feldspathic gneiss typically contain a subtle stair-step geometry indicative of dextral kinematics (Fig. 3.9g). While most of the mantled clasts are symmetrical, there are a few feldspars with apparently dextrally rotated wings (Fig. 3.9h).

3.4 DISCUSSION

3.4.1 Deformation origin for myrmekites and flame perthites

The development of myrmekite within the quartzo-feldspathic gneiss is broadly similar to that of the metagranite for the following reasons: (1) myrmekites are preferentially concentrated along the grain boundaries parallel to the shortening direction; (2) myrmekite lobes can be seen to be dismembered and incorporated into the alkali feldspar rich tails which (3) are very common around feldspar porphyroclasts. Additionally, the modal abundances of alkali feldspar porphyroclasts are greatly reduced going from protomylonite to mylonite. This suggests that like in the metagranite of chapter 2, myrmekites within the quartzo-feldspathic gneiss are strain-induced dissolution-precipitation replacement structures. Myrmekite formation aids in reducing the grain size and modal abundance of alkali feldspar and contribute to the generation of a weaker polymineralic matrix (Ree *et al.*, 2005; Ceccato *et al.*, 2018).

EDS analyses on the myrmekites within the quartzo-feldspathic gneiss reveal them to contain both Na and Ca, and so the chemistry of the myrmekite forming reaction is assumed to be largely similar as to that presented in chapter 2. Myrmekite formation requires both a source for Ca and Na, and a sink for K. The Ca and Na can be sourced directly from dissolving adjacent plagioclase, which occurs in abundance. There is some muscovite forming within and adjacent to myrmekite, however this is not as common as within the metagranite. There are however abundantly developed alkali feldspar tails occurring around most feldspar porphyroclasts and this was most likely the main sink for K. As the sources as sinks for this rock can be reliably identified, the myrmekite forming reaction could potentially be a closed-system reaction on a mm-scale within the quartzo-feldspathic gneiss.

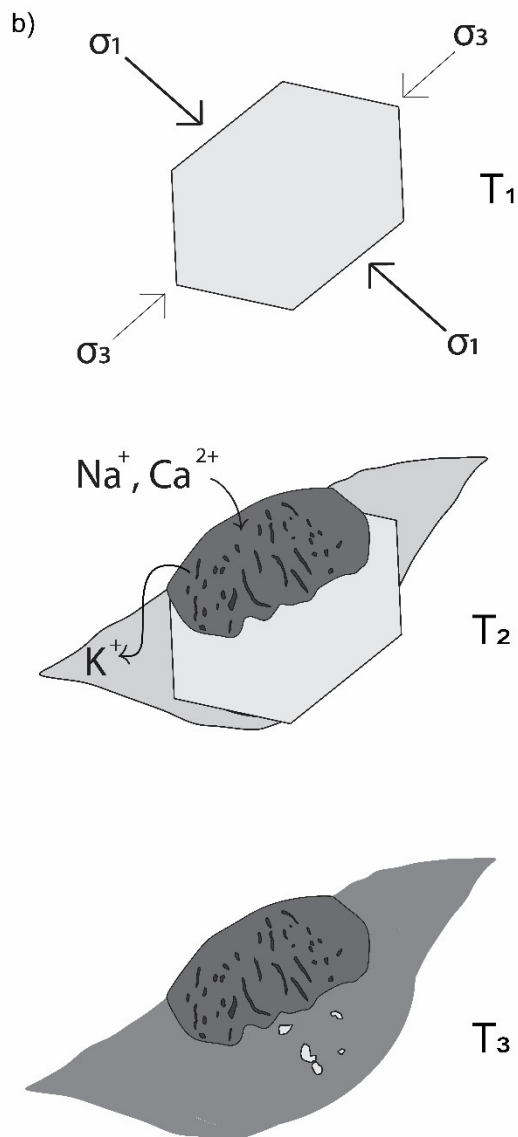
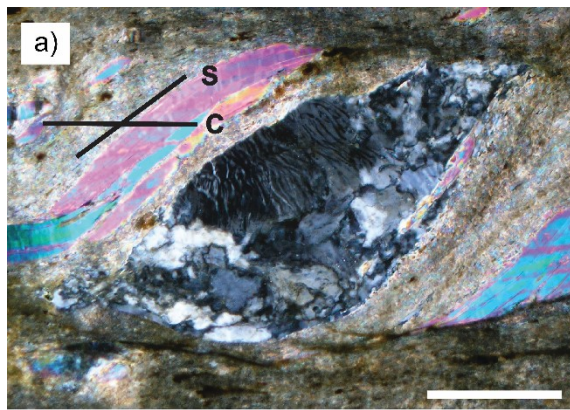
The drivers for myrmekite growth within the migmatitic biotite gneiss are harder to establish. Ascertaining the occurrence and orientation of myrmekites within this rock is complicated by the presence of albitic rims which have replaced alkali feldspar porphyroclasts from all sides. Careful high-contrast SEM-BSE imaging and EDS analyses reveal that plagioclase and wormy quartz intergrowths are preferentially developed on the sides of grains facing the shortening axes within the S/C fabric of the rock. No quartz grains were found within the short ends of alkali feldspar porphyroclasts. This indicates that myrmekite generation within the migmatitic biotite gneiss was also structurally controlled, driven by stress and strain considerations and syn-kinematic to deformation. The occurrence of albite rich tails on the myrmekite bearing polycrystals could potentially be pseudomorphs of alkali feldspar strain shadows which developed due to myrmekite reaction producing excess K. A conceptual model is presented below. The lack of large amounts of alkali feldspar to generate myrmekite mean that myrmekite formation was not a significant strain-accommodation process within the migmatitic biotite gneisses.

The great abundance of flame perthites developed within many alkali feldspar porphyroclasts within the migmatitic biotite gneiss allows for an estimation of their average orientation. The preferential orientation of flames subparallel to the maximum shortening direction as inferred from the S/C fabric,

and their common nucleation on high-stress points such as grain boundaries, indicates that they are contemporaneous with, and driven by deformation. The flames typically have the same orientation as the cryptoperthites, although in places they are transgressive (Fig. 3.6f). This suggests that as in the stress-induced model of Pryer and Robyn (1995, 1996), flame perthites propagate congruently, parallel to the orientation of least lattice misfit between alkali feldspar and albite. However, contrary to Pryer *et al.* (1995) who found a difference of less than 5° between flame and host, observations with the optical microscope indicate that while all flames within the same grain have approximately the same crystallographic orientation, they are at an angle to the host alkali feldspar. EBSD analysis of the flame perthites, the cryptoperthites and the host alkali feldspar within the migmatitic biotite gneiss could better clarify whether there is indeed a crystallographic control on the occurrence of flame perthites within these rocks.

3.4.2 Relative timing of replacement textures

Within both gneisses, flame perthites and myrmekites occur together. Other authors have found the co-occurrence of these two alkali feldspar replacement structures; structurally oriented flame perthite nucleates on lobes of myrmekite developed within high-grade migmatitic gneisses of pelitic protoliths (Vernon, 1999) indicating that myrmekite growth came first. Conversely, Menegon *et al.* (2006) found myrmekites and flame perthite developed together within deformed granitoids but inferred that flame perthite development predated the onset of shearing and myrmekite formation as they had no relation to the kinematic framework of the rock. The paucity of flame perthites within the quartzo-feldspathic gneiss and the replacement of most myrmekites by mostly albite rims within the migmatitic gneiss has obscured cross-cutting relationships between flame perthites and myrmekites and makes establishing relative age relationships difficult. While their preferential orientations established both textures as developing syn-kinematically, it is difficult to imagine that these developed concurrently with one another as they have differing chemistries.



Albite rims within the migmatitic biotite gneiss show no relationship to the kinematic framework, instead surrounding alkali feldspar from all sides. That albite rims also replace myrmekite lobes and have a cross-cutting relationship with flame perthites (Fig. 3.6h) shows that albization post-dates both myrmekite and flame perthite generation. That the sigmoidal shape of host alkali feldspar crystals was still preserved suggests that the albite replacement was much later, post-dating active deformation that would have destroyed the sigmoidal shape. Figure 10 is a conceptual model for explaining the formation of the complex polycrystalline sigmoidal crystals within the migmatitic biotite gneiss. At T_1 an alkali feldspar porphyroclast is differentially stressed and at T_2 develops myrmekites on the sides facing the incremental shortening direction. The long axes of quartz rods are parallel to the direction of reaction front propagation. The excess K from the myrmekite reaction migrates to sites of low stress, i.e. the pressure shadows of the porphyroclasts,

Fig. 3.10 XPL photomicrograph of a sigmoidal polycrystal and a conceptual model for its genesis. a) Alkali feldspar porphyroclast almost completely replaced by myrmekite and subsequently albitic plagioclase. Scale bar is 200 μm . b) Conceptual model for crystal in a) from time T_1 where an alkali feldspar porphyroclast is differentially stressed to T_2 where it develops structurally controlled myrmekite and alkali feldspar pressure shadows to T_3 where almost all the alkali feldspar is replaced by albitic plagioclase

and precipitates as fine-grained alkali feldspar in an equivalent way to textures seen within the quartzo-feldspathic gneisses. At some later time, T_3 , the ingress of a Na-rich fluid causes the pseudomorphic replacement of the alkali feldspar porphyroclast as well as the pressure shadow tails, with only interstitial amounts remaining within the interior of the porphyroclast. The tails on all porphyroclasts are completely replaced, likely aided by the fine-grain sizes of alkali feldspars precipitating there during deformation.

3.4.3 Fluid-conditions during shear zone evolution

The three co-occurring alkali feldspar replacement reactions within the migmatitic biotite gneiss, myrmekites, flame perthites and albite rims, each have a different chemistry as revealed by EDS analyses. Myrmekite generation requires Na and Ca bearing fluids, flame perthites only Na and the albitic rims mostly Na with minor Ca. While this would ideally be better resolved by using an electron probe microanalyzer (EPMA), semi-quantitative differences between these are enough to suggest that the migmatitic biotite gneiss equilibrated with fluids of different compositions at different times. The observation that there are no alkali feldspar porphyroclasts directly in contact with the matrix, and that these are always completely surrounded by mostly albitic rims, clearly establishes that alkali feldspars within the migmatitic gneiss were out of equilibrium with the surrounding fluid. Only the largest alkali feldspar clasts contain a recognisable core of relict alkali feldspar. The embayment from all sides indicates that this is an example of fluid-driven feldspar replacement structure. The sharp reaction front between the alkali feldspar and the albite rims is a feature characteristic of mineral replacement reactions induced by fluids (Engvik *et al.*, 2008). The great abundance of these albite rims, and the lack of any clear reactions within nearby Na-bearing minerals such as plagioclase, strongly suggest that there was ingress of externally buffered Na-bearing fluids. Further evidence of external fluid influx is found in the biotites well developed along the strain shadows of porphyroclasts being associated with blocky Fe-oxide, which suggests a large amount of excess iron, and field observations showing increased chloritisation along mylonite zones within this unit.

All three alkali feldspar replacement reactions imply Na for K exchange. With the exception of very low temperature brines, K/Na ratios across all crustal fluids, including oilfield brines, metamorphic and magmatic fluids, vary systematically with temperature (Yardley *et al.*, 2003). Na-metasomatism arises from fluids flowing up-temperature (Yardley, 2013). Because dissolution-precipitation reactions occur at the parent-product interface, and only small amounts of material are in solution at any one time, these mineral replacement reactions are governed by the relative and not absolute solubilities of phases (Putnis, 2009). Experimental work into the solubility of an albite + alkali feldspar + muscovite + quartz assemblage from 400 ° to 600 °C at 0.2 GPa and 1 m total chloride by Pak (1998), offers a plausible comparison in terms of composition and P-T conditions. Their results indicated that the K/Na ratio in the fluid phase decreases with decreasing temperature, similarly indicating that to dissolve a K-bearing phase and precipitate a Na-bearing phase would require a fluid moving up-temperature.

Albitisation within high-grade metamorphic terranes is often thought to occur late, during the uplift phases (Munz *et al.*, 1995; Kent *et al.*, 2000), and dominantly through the penetration of sedimentary brines, as confirmed by isotope studies (Gleeson *et al.*, 2003; Kendrick *et al.*, 2008). Another possible metasomatising agent is fluids from igneous intrusions, the compositions of which will depend strongly on the magmas composition, and will likely be strongly buffered by the rock composition in terms of Fe, K and Ca (Yardley, 2013). Syn- to post-deformational pegmatites occurs widely within the field area and are dominantly composed of quartz, microcline and oligoclase (Lambert, 2013). While mylonite zones are often preferentially located along pegmatite contacts, the albite rims most likely post-date active deformation and there was no indication in the field of increase fluid-rock interaction adjacent to the later pegmatites which cross-cut the foliation. Fluids in equilibrium with an oligoclase bearing pegmatite could potentially contain dissolved Na but constraining the source of the external fluids is at this point highly speculative.

3.4.4 Alkali feldspar weak, plagioclase strong?

The replacement of alkali feldspar at high-stress sites by myrmekites and extensive development of alkali feldspar pressure shadows on porphyroclasts suggests significant dissolution/precipitation of alkali feldspar as deformation progressed. Dissolution-precipitation creep of alkali feldspars has been documented at 450 - 500 °C within similar myrmekite-bearing granitic mylonites (Menegon *et al.*, 2008). While alkali feldspar modal abundances within these quartzo-feldspathic rocks can be seen to be reduced during deformation to less than 1%, the same cannot be said for plagioclase porphyroclasts. Within the metagranite and quartzo-feldspathic gneiss, plagioclase porphyroclasts persist within the matrix of the most highly strained rocks. Most grains are internally fractured, with alkali feldspar commonly precipitating within these fractures, and some larger offsets are preserved (Fig. 3.5c). This, coupled with evidence of plastic deformation from undulatory extinction and the presence of deformation twinning, shows that deformation within plagioclase was transitional between frictional and plastic.

The transition from brittle frictional sliding to crystal-plastic flow in plagioclase is understood from studies into naturally (Hanmer, 1982; Pryer, 1993; Wintsch and Yi, 2002) and experimentally (Rybacki and Dresen, 2000) deformed rocks to occur at 450 - 500°C. While there was likely some dissolution-precipitation of plagioclase at high-strain sites with alkali feldspar to form myrmekite, the lack of plagioclase overgrowths into extensional sites, an important criteria in identifying dissolution and replacement creep (Wintsch and Yi, 2002), points to dissolution-precipitation processes not being as significant a process as for alkali feldspar. Additionally, as recrystallisation in plagioclase takes place at higher temperatures than alkali feldspar (Srivastava and Mitra, 1996), all deformation processes active within plagioclase were not as efficient at reducing the grain-size as myrmekite formation was within alkali feldspar. As granitoids are often considered mechanically to be two-phase mixtures of weaker quartz and stronger feldspar at low to medium metamorphic grades (Fitz-Gerald and Stünitz, 1993) this has implications for the modelling of mylonites within the PSZ, as plagioclase alone would be the load-bearing phase if these mylonites were to be modelled as two-phase systems.

3.4.5 Strain-partitioning

Within chapter 2, the quartz-quartz grain boundaries within the metagranite were established to indicate that deformation occurred at the sub-grain rotation (SGR)/grain boundary migration (GBM) transition which is estimated to occur around ~ 500 °C (Stipp *et al.*, 2002b). Within the deformed gneisses however, the predominance of quartz textures is slightly different. Quartz grains within the quartzo-feldspathic gneiss are highly irregular in size and shape, depending on the size of the quartz ribbons they are hosted in. There is minimal evidence for the formation of subgrains. Deformation within the quartzo-feldspathic gneiss therefore was likely to be highly similar to that of the metagranite and is suggestive of GBM or regime 3 of Hirth and Tullis (1992) which indicates deformation at high temperatures/low stress conditions (Hirth and Tullis, 1992; Stipp and Kunze, 2008).

There are two distinct types of quartz-quartz textures preserved within the migmatitic biotite gneiss. Within the strain shadows of the largest plagioclase porphyroclasts, quartz grains are coarse and polygonal in shape. This texture is reminiscent of an 'equilibrium-fabric' with interfacial angles approaching 120° produced during grain boundary area reduction (Passchier and Trouw, 2005). This is a higher temperature structure and due to its limited preservation within structural sites where it was presumably protected from deformation, it is likely a relict structure from the higher temperature amphibolite facies Namaqua Orogeny deformation. These are qualitative inferences as temperature and strain rate are not the only parameters affecting quartz deformation behaviour; the amount of water present during deformation is also a critical factor (Hirth and Tullis, 1992; Stipp *et al.*, 2002a, 2006; Law, 2014).

The majority of the quartz-quartz grain boundaries within folded aggregates within the migmatitic biotite gneiss have well developed subgrains elongate at an angle to the foliation with a strong LPO. This is suggestive of dynamic recrystallisation by dominantly SGR. This is supported by the average grain size of the sub-grains and the newly crystallised grains being approximately the same size (Platt

and Behr, 2011). This indicates that within the migmatitic biotite gneiss, deformation continued at lower temperatures and/or higher stress conditions. There was therefore likely some degree of lithology based strain-partitioning within these rocks and this is supported by the opposing shear sense indicators within the metagranite discussed in chapter 2, which possibly arose due to the viscosity contrast between these lithologies (Hippertt and Tohver, 1999).

3.5 CONCLUSIONS

While the orientation of the myrmekites within the migmatitic gneiss suggests that they are syn-kinematic, recrystallised myrmekites could not be observed to be incorporated into alkali feldspar tails or the matrix due to the late albitisation overprint. Regardless, the low modal abundance of alkali feldspar within mylonites developed along micaceous melanosomes of the migmatitic biotite gneiss, precludes myrmekite generation from being an important facilitator of deformation within this unit. This contrasts with the quartzo-feldspathic gneiss which preserves abundant evidence for myrmekite generation being of principal importance in the deformation of alkali feldspar and in contributing to generating a fine-grained matrix. The importance of syn-kinematic myrmekite growth to deformation is therefore strongly lithologically controlled. The quartz microstructures developed within these two units suggest that strain was preferentially partitioned into the migmatitic biotite gneiss to lower temperatures and/or higher strain-rates.

Petrological and field-based evidence for pervasive external influx is limited to the migmatitic biotite gneiss. Alkali feldspars within this unit show three different replacement reactions: (1) Pure Na for K-exchange generated flame perthites that are sub-parallel to the maximum compressive stress, (2) Ca-Na myrmekites are preferentially orientated along the sides of grains perpendicular to the maximum compressive stress, in the same context as the flame perthites and (3) albitic rims pseudomorphically replace alkali feldspars such that porphyroclasts are never directly in contact with the matrix. The varying chemistry of these replacements and their temporal relationships to one another points to equilibration with fluids of varying compositions over time.

4 CHAPTER FOUR: CONCLUSIONS

A quantitative evaluation of the preferred orientation for myrmekite growth showed a clear relationship to the local kinematic framework. This established myrmekites within granitic rocks of the PSZ as being strain-induced dissolution-precipitation reaction textures. Their textural evolution from delicate wormy intergrowths to recrystallised polygonal aggregates that can be seen to be sheared off and incorporated into the polymineralic matrix, indicates that myrmekites are part of how these granites accommodated strain. Thermobarometry calculations using two-feldspar thermometry and phengite barometry showed myrmekite growth to be stable across a range of temperatures and pressures, from 370 °C to 500 °C with a continuous range of pressures from 0.05 -0.5 GPa. The wide variations in the spacing of quartz rods and their successive spacing decrease towards host alkali feldspar is an indication that deformation-induced myrmekite growth continued under lower-grade conditions as the PSZ was exhumed. The documentation of strain-induced myrmekites within surrounding poly-deformed gneisses of varying compositions suggests that myrmekite formation and subsequent contribution to deformation is not just a locally important feature of deformed granites but could potentially be of importance within all broadly quartzo-feldspathic gneisses of the PSZ.

Synkinematic reactions within the metagranite, including myrmekite formation, were established to be driven by the internal recycling of components, and T-H₂O pseudosections supported that there was not a need for significant external fluid input. On the contrary, the migmatitic biotite gneiss it is in contact with shows pervasive fluid-driven retrogression in the field and under the microscope. The alkali feldspars within this unit are host to three different replacement microstructures: flame perthites, myrmekites and albitic rims. Similarly, within protomylonites of the quartzo-feldspathic gneiss, there were millimetre-scale zones where plagioclase porphyroclasts as well as myrmekite plagioclase were albitised and sericitised along sharp fronts. The heterogeneity of these replacement reactions suggests that the fluid composition these rocks were in contact with varied over time. While the exact evolution cannot be constrained presently, this study highlights how fluid infiltration and

composition within shear zone systems, even across tens of meters, is highly variable over both space and time. This fluid influx will promote mineral replacements that obliterate previous deformation or mineralisation events that would not have been recognised had there not been incomplete equilibration.

The different mineral replacement reactions and deformation conditions suggested by quartz microfabrics between the quartzo-feldspathic gneisses and the migmatitic biotite gneiss, indicate that there was some degree of strain partitioning as well as fluid-localisation that was controlled by lithology. That deformation continued at lower-temperatures and or higher strain-rates within the migmatitic biotite gneiss, and that this unit was the locus for increased fluid-influx and retrogression reactions, is possibly due to its higher mica content and strong pre-existing migmatitic fabric. While potentially obscured by re-crystallisation during albitisation, myrmekite formation does not seem to be of principal importance within the migmatitic biotite gneiss.

4.1 FUTURE WORK

The various alkali feldspar microstructures encountered in the migmatitic biotite gneiss strongly suggest that dissolution-precipitation processes were the main drivers for mineral replacements. Several questions remain. Pryer *et al.* (1995) argued that the growth of albite in the flame perthite replacement reaction occurs by replacement of K by Na without migration of Al, Si and O, as suggested by the topotaxial relationship between alkali feldspar host and albite flames. This was thought to require dry conditions where dissolution-precipitation processes would be inefficient operating along the incoherent interfaces created by new grain boundaries (Pryer and Robin, 1996). However experimental work on oxygen-isotope exchange during feldspar replacement reactions suggest a different perspective. Starting with the experimental work of O'Neil and Taylor (1967), which used ^{18}O as tracers in the reaction between albite ($\text{NaAlSi}_3\text{O}_8$) and KCl in hydrothermal solution to produce sanidine (KAlSi_3O_8), complete oxygen isotope equilibration between solution and feldspars was found. This suggested that the Si-O and Al-O must have been broken during feldspar replacement reactions.

In a more recent but similar study (Labotka *et al.*, 2004), albite was reacted with an O^{18} enriched solution of KCl and after 6 days showed rims where Na was nearly fully replaced by K, and the O within this rim was strongly enriched in O^{18} , indicating the wholesale restructuring of the feldspar. Natural hydrothermally altered feldspars show rims low in $\delta^{18}O$ indicating interactions with meteoric water (Cole *et al.*, 2004) further illustrating that replacement reactions involve restructuring of the whole crystal lattice and not just simple cationic exchange. Secondly, dissolution-precipitation reactions also maintain crystallographic continuity between product and parent through epitaxial nucleation (Putnis and Putnis, 2007; Ruiz-Agudo *et al.*, 2014). Alkali feldspars experimentally reacted with NaCl solutions show saw-tooth shaped replacements by albite via dissolution-precipitation processes (Norberg *et al.*, 2011) which highly resemble flame perthites. Thus, flame perthite generation potentially also occurs through a dissolution-precipitation process.

In-situ ion probe measurements of $\delta^{18}O$ values offer a possible avenue of enquiry into the mechanism of formation of flame perthites and whether the alkali feldspar replacements in these rocks were precipitated by fluids of varying compositions. For example, as the syn-kinematic reactions of the metagranite could be internally balanced, one would expect the isotopic signature of that rock to be fairly homogenous. Within the migmatitic biotite gneiss, looking at the isotopic composition of the alkali feldspar host, the flame perthites, the preserved myrmekites and the albitic rims could offer insight into various questions: (1) If flame perthite generation proceeds through pure Na for K exchange, without breaking of the Si-O-Al bonds as proposed by Pryer *et al.* (1995), then one would expect the isotopic composition of the host alkali feldspar and the albite flames to be the same. If this is not the case, this would be strong evidence towards these microstructures being another example of coupled dissolution-precipitation reactions. (2) Myrmekites and flame perthites are both developed syn-kinematically within the same structural position. They however have differing chemistries, with myrmekites suggesting interaction with a Na, Ca bearing fluid while flame albitic rims only requiring a source for Na. Are these reactions driven by the same fluids and are these fluids internally derived and thus bear the same isotopic signature as nearby feldspars? (3) Both myrmekites and flame perthites

have then subsequently been overprinted by pervasive albite rims that embay alkali feldspar grains and have no clear relationship to the kinematic framework and are thus proposed to be a much later event. Plagioclase porphyroclasts within this rock show minimal evidence for being the source of the needed cations and the great volume of the albite rims suggests an externally buffered Na-bearing fluid reservoir. Do these late albite rims preserve a different isotopic signature to either the flame perthites and the myrmekites and could this be used to constrain the isotopic evolution of the fluids interacting within these rocks? (4) Plagioclase porphyroclasts and myrmekites within the quartzofeldspathic gneiss are locally replaced and altered and still preserve evidence for pores that have not been subsequently closed by deformation or compaction. This suggests that these replacement textures are very late overprints. It would be of interest to test whether the isotopic composition of the altered vs unaltered plagioclase varies systematically and to test whether these fluids are of meteoric origin as indicated by low $\delta^{18}\text{O}$ values (Cole *et al.*, 2004).

REFERENCES

- Abart, R., Heuser, D. and Habler, G. (2014) 'Mechanisms of myrmekite formation: case study from the Weinsberg granite, Moldanubian zone, Upper Austria', *Contributions to Mineralogy and Petrology*, 168(5), pp. 1–15. doi: 10.1007/s00410-014-1074-7.
- Angombe, M. T. (2016) *The lithostratigraphy and structural components of the Eureka Shear Zone, Southern Namibia*. Stellenbosch University.
- Ashworth, J. R. (1972) 'Myrmekites of exsolution and replacement origins', *Geological Magazine*, 109(Plate 1), pp. 45–62.
- Ashworth, J. R. (1986) 'Myrmekite replacing albite in prograde metamorphism.', *American Mineralogist*, 71(7–8), pp. 895–899.
- Ashworth, J. R. and Chambers, A. D. (2000) 'Symplectic Reaction in Olivine and the Controls of Intergrowth Spacing in Symplectites', *Journal of Petrology*, 41(2), pp. 285–304. doi: 10.1093/petrology/41.2.285.
- Becke, F. (1908) 'Über Myrmekit.', *Schweizerische Mineralogische und Petrographische Mitteilungen*, 27, pp. 377–390.
- Berman, R. G. (1988) 'Internally-Consistent Thermodynamic Data for Minerals in the System Na₂O-K₂O-CaO-FeO-Fe₂O-Al₂O₃-SiO₂-H₂O-CO₂', *Journal of Petrology*, 29(Part 2), pp. 445–522.
- Bial, J., Büttner, S. H. and Frei, D. (2015) 'Formation and emplacement of two contrasting late-Mesoproterozoic magma types in the central Namaqua Metamorphic Complex (South Africa, Namibia): Evidence from geochemistry and geochronology', *Lithos*. Elsevier B.V., 224–225, pp. 272–294. doi: 10.1016/j.lithos.2015.02.021.

- Blignault, H. J. (1977) *Structural-metamorphic imprint on part of the Namaqua Mobile Belt in South West Africa*, *Bulletin of the Precambrian Research unit*. Dissertation, Univeristy of Cape Town.
- Blignault, H. J., Van Aswegen, G., Van der Merwe, S. W. and Colliston, W. P. (1983) *The Namaqualand Geotraverse and Environs: Part of the Proterozoic Namaqua Mobile Belt*.
- Bukovská, Z., Jeřábek, P. and Morales, L. F. G. (2015) 'Major softening at brittle-ductile transition due to interplay between chemical and deformation processes: An insight from evolution of shear bands in the South Armoricain Shear Zone', *Journal of Geophysical Research: Solid Earth*, 121, pp. 1158–1182. doi: 10.1002/ 2015JB012319.
- De Capitani, C. and Petrakakis, K. (2010) 'The computation of equilibrium assemblage diagrams with Theriak/Domino software', *American Mineralogist*, 95(7), pp. 1006–1016. doi: 10.2138/am.2010.3354.
- Carmichael, D. M. (1969) 'On the Mechanism of Prograde Metamorphic Reactions in Quartz-Bearing Pelitic Rocks', *Contributions to Mineralogy and Petrology*, 20, pp. 244–267.
- Ceccato, A., Menegon, L., Pennacchioni, G. and Morales, L. F. G. (2018) 'Myrmekite and strain weakening in granitoid mylonites', *Solid Earth Discussions*, in review, pp. 1–39. doi: 10.5194/se-2018-70.
- Cesare, B., Marchesi, C. and Connolly, J. A. D. (2002) 'Growth of myrmekite coronas by contact metamorphism of granitic mylonites in the aureole of Cima di Vila, Eastern Alps, Italy', *Journal of Metamorphic Geology*, 20(1), pp. 203–213. doi: 10.1046/j.0263-4929.2001.00351.x.
- Clifford, T. N. (2004) 'U-Pb Zircon Calendar for Namaquan (Grenville) Crustal Events in the Granulite-facies Terrane of the O'okiep Copper District of South Africa', *Journal of Petrology*, 45(4), pp. 669–691. doi: 10.1093/petrology/egg097.
- Cole, D. R., Larson, P. B., Riciputi, L. R. and Mora, C. I. (2004) 'Oxygen isotope zoning profiles in hydrothermally altered feldspars: Estimating the duration of water-rock interaction', *Geology*, 32(1), pp. 29–32. doi: 10.1130/G19881.1.
- Colliston, W. P. and Schoch, A. E. (2000) 'Mid-Proterozoic tectonic evolution along the Orange River on the border between South Africa and Namibia', *Communs geol. Surv. Namibia*, 12, pp. 57–66.
- Colliston, W. P. and Schoch, A. E. (2006) 'The distribution and diagnostic features of deformed plutonic rocks in two terranes of the Namaquamobile belt along the Orange (Gariiep) River, South Africa', *South African Journal of Geology*, 109, pp. 301–324.
- Colliston, W. P. and Schoch, A. E. (2013) 'Wrench-shearing during the namaqua orogenesis-mesoproterozoic late stage deformation effects during rodinia assembly', *Precambrian Research*. Elsevier B.V., 232, pp. 44–58. doi: 10.1016/j.precamres.2012.10.015.
- Cornell, D. H., Thomas, R. J., Moen, H. F. G., Reid, D. L., Moore, J. M. and Gibson, R. L. (2006) 'The Namaqua-Natal Province', in Johnson, C. R., Anhaeusser, C. R., and Thomas, R. J. (eds) *The Geology of South Africa*. Pretoria: Geological Society of South Africa, pp. 395–420.
- Dégi, J., Abart, R., Török, K., Bali, E., Wirth, R. and Rhede, D. (2010) 'Symplectite formation during decompression induced garnet breakdown in lower crustal mafic granulite xenoliths: Mechanisms and rates', *Contributions to Mineralogy and Petrology*, 159(3), pp. 293–314. doi: 10.1007/s00410-009-0428-z.
- Diener, J. F. A., Thomas, R. J. and Macey, P. H. (2017) 'Pan-African accretionary metamorphism in the Sperrgebiet Domain , Gariiep Belt, SW Namibia', *Precambrian Research*. Elsevier B.V., 292(February), pp. 152–162. doi: 10.1016/j.precamres.2017.02.006.

- Diener, J. F. A., White, R. W., Link, K., Dreyer, T. S. and Moodley, A. (2013) 'Clockwise, low-P metamorphism of the Aus granulite terrain, southern Namibia, during the Mesoproterozoic Namaqua Orogeny', *Precambrian Research*. Elsevier B.V., 224, pp. 629–652. doi: 10.1016/j.precamres.2012.11.009.
- Eglington, B. M. (2006) 'Evolution of the Namaqua-Natal Belt, southern Africa - A geochronological and isotope geochemical review', *Journal of African Earth Sciences*, 46(1–2), pp. 93–111. doi: 10.1016/j.jafrearsci.2006.01.014.
- Engvik, A. K., Putnis, A., Fitz Gerald, J. D. and Austrheim, H. (2008) 'Albitization of granitic rocks: The mechanism of replacement of oligoclase by albite', *Canadian Mineralogist*, 46(6), pp. 1401–1415. doi: 10.3749/canmin.46.6.1401.
- Fisher, G. W. (1973) 'Non-equilibrium thermodynamics as a model for diffusion-controlled metamorphic processes.', *American Journal of Science*, 273, pp. 897–924.
- Fitz-Gerald, J. D. and Stünitz, H. (1993) 'Deformation of granitoids at low metamorphic grade I: Reactions and grain size reduction', *Tectonophysics*, 221(3–4), pp. 269–297. doi: 10.1016/0040-1951(93)90164-F.
- Frisicale, M. C., Martinez, F. J., Dimieri, L. V. and Dristas, J. A. (2005) 'Microstructural analysis and P-T conditions of the Azul megashear zone, Tandilia, Buenos Aires province, Argentina', *Journal of South American Earth Sciences*, 19(4), pp. 433–444. doi: 10.1016/j.jsames.2005.06.006.
- Fukuda, J. I. and Okudaira, T. (2013) 'Grain-size-sensitive creep of plagioclase accompanied by solution-precipitation and mass transfer under mid-crustal conditions', *Journal of Structural Geology*. Elsevier Ltd, 51, pp. 61–73. doi: 10.1016/j.jsg.2013.03.006.
- Fukuda, J., Okudaira, T., Satsukawa, T. and Michibayashi, K. (2012) 'Solution-precipitation of K-feldspar in deformed granitoids and its relationship to the distribution of water', *Tectonophysics*. Elsevier B.V., 532–535, pp. 175–185. doi: 10.1016/j.tecto.2012.01.033.
- Gaidies, F., Milke, R., Heinrich, W. and Abart, R. (2017) 'Metamorphic mineral reactions: Porphyroblast, corona and symplectite growth', *Mineral reaction kinetics: Microstructures, textures, chemical and isotopic signatures*, 16, pp. 469–540. doi: 10.1180/EMU-notes.16.14.
- Gleeson, S. A., Dyardley, B. W., Munz, I. A. and Boyce, A. J. (2003) 'Infiltration of basinal fluids into high-grade basement, South Norway: Sources and behaviour of waters and brines', *Geofluids*, 3(1), pp. 33–48. doi: 10.1046/j.1468-8123.2003.00047.x.
- Gresens, R. L. (1967) 'Composition-volume relationships of metasomatism', *Chemical Geology*, 2, pp. 47–65. doi: 10.1016/0009-2541(67)90004-6.
- Haggart, A. M. J., Jamieson, R. A., Reynolds, P. H., Krogh, T. E. and Beaumont, C. (1993) 'Last Gasp of the Grenville Orogeny: Thermochronology of the Grenville Front Tectonic Zone near Killarney, Ontario', *The Journal of Geology*, 101(5), pp. 575–589.
- Han, L., Zhou, Y., He, C. and Li, H. (2016) 'Sublithostatic pore fluid pressure in the brittle-ductile transition zone of Mesozoic Yingxiu-Beichuan fault and its implication for the 2008 Mw7.9 Wenchuan earthquake', *Journal of Asian Earth Sciences*. Elsevier Ltd, 117, pp. 107–118. doi: 10.1016/j.jseaes.2015.12.009.
- Hanmer, S. K. (1982) 'Microstructure and geochemistry of plagioclase and microcline in naturally deformed granite.', *Journal of Structural Geology*, 4(1), pp. 197–213. Available at: <papers2://publication/uuid/54C1D1E6-7C70-4DFF-A98B-B7873D2B9520>.
- Harlov, D. E. and Wirth, R. (2000) 'K-feldspar-quartz and K-feldspar-plagioclase phase boundary

interaction in garnet-orthopyroxene gneiss's from the Val Strona di Omegna, Ivrea-Verbano Zone, northern Italy', *Contributions to Mineralogy and Petrology*, 140(2), pp. 148–162. doi: 10.1007/s004100000185.

Hartnady, C., Joubert, P. and Stowe, C. (1985) 'Proterozoic Crustal Evolution in Southwestern Africa', *Episodes*, 8(4), pp. 236–244.

Hippertt, J. and Tohver, E. (1999) 'On the development of zones of reverse shearing in mylonitic rocks', *Journal of Structural Geology*, 21(11), pp. 1603–1614. doi: 10.1016/S0191-8141(99)00107-8.

Hirth, G. and Tullis, J. (1992) 'Dislocation creep regimes in quartz aggregates', *Journal of Structural Geology*, 14(2), pp. 145–159.

Hoffman, P. F. (1991) 'Did the breakout of Laurentia turn Gondwanaland inside-out?', *Science*, 252(5011), pp. 1409–1412. doi: 10.1126/science.252.5011.1409.

Holland, T. J. . and Powell, R. (2000) *AX: a Program to Calculate Activities of Mineral Endmembers from Chemical Analyses (Usually Determined by Electron Microprobe)*. Available at: <https://www.esc.cam.ac.uk/research/research-groups/research-projects/tim-hollands-software-pages/ax>.

Imon, R., Okudaira, T. and Fujimoto, A. (2002) 'Dissolution and precipitation processes in deformed amphibolites : an example from the ductile shear zone of the Ryoke metamorphic belt , SW Japan', *Journal of Metamorphic Geology*, 20, pp. 297–308.

Indongo, J. (2017) *The Lithological and Structural Characterisation of the Sperlingputs Shear Zone in Southern Namibia*. Stellenbosch University.

Jacobs, J., Pisarevsky, S., Thomas, R. J. and Becker, T. (2008) 'The Kalahari Craton during the assembly and dispersal of Rodinia', *Precambrian Research*, 160(1–2), pp. 142–158. doi: 10.1016/j.precamres.2007.04.022.

Jacobs, J., Thomas, R. and Weber, K. (1993) 'Accretion and indentation tectonics at the southern margin of the Kaapvall craton during Kibaran (Greenville) orogeny', *Geological Society Of America*, 21(March), pp. 203–206. doi: 10.1130/0091-7613(1993)021<0203.

Joanny, V., van Roermund, H. and Lardeaux, J. M. (1991) 'The clinopyroxene/plagioclase symplectite in retrograde eclogites: A potential geothermobarometer', *Geologische Rundschau*, 80(2), pp. 303–320. doi: 10.1007/BF01829368.

Johnson, S. E., Marsh, J. H. and Vernon, R. H. (2008) 'From tonalite to mylonite: Coupled mechanical and chemical processes in foliation development and strain localization', *Journal of the Virtual Explorer*, 30(6). doi: 10.3809/jvirtex.2009.00208.

Joubert, P. (1986) 'Namaqualand-a model of proterozoic accretion?', *Transactions- Geological Society of South Africa*, 89(2), pp. 79–96.

Kendrick, M. A., Baker, T., Fu, B., Phillips, D. and Williams, P. J. (2008) 'Noble gas and halogen constraints on regionally extensive mid-crustal Na-Ca metasomatism, the Proterozoic Eastern Mount Isa Block, Australia', *Precambrian Research*, 163(1–2), pp. 131–150. doi: 10.1016/j.precamres.2007.08.015.

Kent, A. J. R., Ashley, P. M. and Fanning, C. M. (2000) 'Metasomatic alteration associated with regional metamorphism: An example from the Willyama Supergroup, South Australia', *Lithos*, 54(1–2), pp. 33–62. doi: 10.1016/S0024-4937(00)00021-9.

Knipe, R. J. (1989) 'Deformation mechanisms recognition from natural tectonites', *Journal of Structural Geology*, 11(1), pp. 127–147.

- Labotka, T. C., Cole, D. R., Fayek, M., Riciputi, L. R. and Stadermann, F. J. (2004) 'Coupled cation and oxygen-isotope exchange between alkali feldspar and aqueous chloride solution', *American Mineralogist*, 89(11–12), pp. 1822–1825. doi: 10.2138/am-2004-11-1229.
- Lambert, C. W. (2013) *Granitic melt transport and emplacement along transcurrent shear zones : Case study of the Pofadder Shear Zone in South Africa and Namibia*. Stellenbosch University.
- Lanari, P., Riel, N., Guillot, S., Vidal, O., Schwartz, S., Pêcher, A. and Hattori, K. H. (2013) 'Deciphering high-pressure metamorphism in collisional context using microprobe mapping methods: Application to the Stak eclogitic massif (northwest Himalaya)', *Geology*, 41(2), pp. 111–114. doi: 10.1130/G33523.1.
- Law, R. D. (2014) 'Deformation thermometry based on quartz c -axis fabrics and recrystallization microstructures : A review', *Journal of Structural Geology*. Elsevier Ltd, 66, pp. 129–161. doi: 10.1016/j.jsg.2014.05.023.
- Macey, P. et al. (2015) *The Precambrian Geology of the Region South of Warmbad from Haib to Velloorsdrif, Southern Namibia, An Explanation to 1:50 000 Geological Map Sheets 2818AC, 2818AD, 2818CA, 2818CB, 2818CC, 2818CD, 2818DA, 902819CA, 2819CB, 2819CC, 2819CD and 2819DA*.
- Macey, P. H. et al. (2017) 'Origin and evolution of the ~1.9 Ga Richtersveld Magmatic Arc, SW Africa', *Precambrian Research*. Elsevier B.V., 292, pp. 417–451. doi: 10.1016/j.precamres.2017.01.013.
- Macey, P. H., Bailie, R. H., Miller, J. A., Thomas, R. J., de Beer, C., Frei, D. and Le Roux, P. (2018) 'Implications of the distribution, age and origins of the granites of the Mesoproterozoic Spektakel Suite for the timing of the Namaqua Orogeny in the Bushmanland Subprovince of the Namaqua- Natal Metamorphic Province, South Africa', *Precambrian Research*, In print.
- MacLaren, A. (1984) *The geology of the area east of Pofadder with emphasis on shearing associated with the Pofadder Lineament, Northwest Cape*. University of Cape Town.
- Massonne, H.-J. and Szpurka, Z. (1997) 'Thermodynamic properties of white micas on the basis of high-pressure experiments in the systems K₂O-MgO-Al₂O₃-SiO₂-H₂O and K₂O-FeO-Al₂O₃-SiO₂-H₂O', *Lithos*, 41, pp. 229–250. doi: 10.1016/S0024-4937(97)82014-2.
- Melosh, B. L. (2015) *Earthquake cycling in the brittle-plastic transition of a transform boundary: The Pofadder Shear Zone, Namibia and South Africa*. Dissertation, University of McGill.
- Melosh, B. L., Rowe, C. D., Gerbi, C., Smit, L. and Macey, P. (2018) 'Seismic cycle feedbacks in a mid-crustal shear zone', *Journal of Structural Geology*. Elsevier Ltd, 112, pp. 95–111. doi: 10.1016/j.jsg.2018.04.004.
- Menegon, L., Pennacchioni, G. and Spiess, R. (2008) 'Dissolution-precipitation creep of K-feldspar in mid-crustal granite mylonites', *Journal of Structural Geology*, 30, pp. 565–579. doi: 10.1016/j.jsg.2008.02.001.
- Menegon, L., Pennacchioni, G. and Stünitz, H. (2006) 'Nucleation and growth of myrmekite during ductile shear deformation in metagranites', *Journal of Metamorphic Geology*, 24(7), pp. 553–568. doi: 10.1111/j.1525-1314.2006.00654.x.
- Milke, R., Neusser, G., Kolzer, K. and Wunder, B. (2013) 'Very little water is necessary to make a dry solid silicate system wet', *Geological Society Of America*, 41(2), pp. 247–250. doi: 10.1130/G33674.1.
- Miller, R. (2008) *The geology of Namibia, Geological Survey of Namibia*.
- Moen, H. F. G. and Toogood, D. J. (2007) *The Geology of the Onseepkans Area Explanation sheet 2818, Pretoria, South Africa: Council for Geoscience*.

- Mongkoltip, P. and Ashworth, J. R. (1983) 'Quantitative Estimation of an Open-system Symplectite-forming Reaction : Restricted Diffusion of Al and Si in Coronas around Olivine', *Journal of Microscopy*, 24(Part 4), pp. 635–661.
- Mukai, H., Austrheim, H., Putnis, C. V. and Putnis, A. (2014) 'Textural evolution of plagioclase feldspar across a shear zone: Implications for deformation mechanism and rock strength', *Journal of Petrology*, 55(8), pp. 1457–1477. doi: 10.1093/petrology/egu030.
- Munz, I. A., Yardley, B. W. D., Banks, D. A. and Wayne, D. (1995) 'Deep penetration of sedimentary fluids in basement rocks from southern Norway: Evidence from hydrocarbon and brine inclusions in quartz veins', *Geochimica et Cosmochimica Acta*, 59(2), pp. 239–254. doi: 10.1016/0016-7037(94)00322-D.
- Nold, J. L. (1984) 'Myrmekite in Belt supergroup metasedimentary rocks - northeast border zone of the Idaho batholith.', *American Mineralogist*, 69(11–12), pp. 1050–1052.
- Norberg, N., Neusser, G., Wirth, R. and Harlov, D. (2011) 'Microstructural evolution during experimental albitization of K-rich alkali feldspar', *Contributions to Mineralogy and Petrology*, 162(3), pp. 531–546. doi: 10.1007/s00410-011-0610-y.
- O'Hara, K. (1990) 'Brittle-plastic deformation in mylonites: an example from the Meadow Fork Thrust, western Blue Ridge province, southern Appalachians', *Geological Society of America Bulletin*, 102(12), pp. 1706–1713. doi: 10.1130/0016-7606(1990)102<1706:BPDIMA>2.3.CO;2.
- O'Neil, J. R. and Taylor, H. P. (1967) 'The oxygen isotope and cation exchange chemistry of feldspars', *The American Mineralogist*, 52(September-October).
- Obata, M., Ozawa, K., Naemura, K. and Miyake, A. (2013) 'Isochemical breakdown of garnet in orogenic garnet peridotite and its implication to reaction kinetics', *Mineralogy and Petrology*, 107(6), pp. 881–895. doi: 10.1007/s00710-012-0260-4.
- Ogilvie, P. and Gibson, R. L. (2017) 'Arrested development – a comparative analysis of multilayer corona textures in high-grade metamorphic rocks', *Solid Earth*, 8(1), pp. 93–135. doi: 10.5194/se-8-93-2017.
- Pak, T. (1998) *Solubility of simple pelite and granite mineral assemblages in supercritical aqueous chloride solutions*, Doctor of Philosophy. University of Wisconsin-Madison.
- Parsons, I., Thompson, P., Lee, M. R. and Cayzer, N. (2005) 'Alkali Feldspar Microtextures as Provenance Indicators in Siliciclastic Rocks and Their Role in Feldspar Dissolution During Transport and Diagenesis', *Journal of Sedimentary Research*, 75(5), pp. 921–942. doi: 10.2110/jsr.2005.071.
- Passchier, C. W. and Trouw, R. A. J. (2005) *Microtectonics*. 2nd edn.
- Pennacchioni, G. (2005) 'Control of the geometry of precursor brittle structures on the type of ductile shear zone in the Adamello tonalites, Southern Alps (Italy)', *Journal of Structural Geology*, 27(4), pp. 627–644. doi: 10.1016/j.jsg.2004.11.008.
- Phillips, E. R. (1974) 'Myrmekite- one hundred years later', *Lithos*, 7, pp. 181–194.
- Phillips, E. R. (1980) 'On polygenetic myrmekite', *Geological Magazine*, 117(1), pp. 29–36.
- Phillips, E. R. and Ransom, D. M. (1968) 'The proportionality of quartz in myrmekite', *Mineralogical Notes*, 53, pp. 1411–1413.
- Phillips, E. R., Ransom, D. M. and Vernon, R. H. (1972) 'Myrmekite and Muscovite Developed by Retrograde Metamorphism at Broken Hill, New South Wales', *Mineralogical Magazine*, 38, pp. 570–578. doi: 10.1180/minmag.1972.038.297.05.

- Platt, J. P. and Behr, W. M. (2011) 'Grainsize evolution in ductile shear zones: Implications for strain localization and the strength of the lithosphere', *Journal of Structural Geology*, 33(4), pp. 537–550. doi: 10.1016/j.jsg.2011.01.018.
- Pryer, L. L. (1993) 'Microstructures in feldspars from a major crustal thrust zone: the Grenville Front, Ontario, Canada', *Journal of Structural Geology*, 15(1), pp. 21–36.
- Pryer, L. L. and Robin, P. Y. F. (1995) 'Retrograde metamorphic reactions in deforming granites and the origin of flame perthite', *Journal of Metamorphic Geology*, 13(6), pp. 645–658. doi: 10.1111/j.1525-1314.1995.tb00249.x.
- Pryer, L. L. and Robin, P. Y. F. (1996) 'Differential stress control on the growth and orientation of flame perthite: A palaeostress-direction indicator', *Journal of Structural Geology*, 18(9), pp. 1151–1166. doi: 10.1016/0191-8141(96)00037-5.
- Pryer, L. L., Robin, P. Y. F. and Lloyd, G. E. (1995) 'An SEM electron-channeling study of flame perthite from the Killarney granite, southwestern Grenville Front, Ontario', *Canadian Mineralogist*, 33(2), pp. 333–347.
- Putnis, A. (2009) 'Mineral Replacement Reactions', *Reviews in Mineralogy and Geochemistry*, 70(1), pp. 87–124. doi: 10.2138/rmg.2009.70.3.
- Putnis, A. (2015) 'Transient Porosity Resulting from Fluid – Mineral Interaction and its Consequences', *Reviews in Mineralogy and Geochemistry*, 80, pp. 1–23.
- Putnis, A. and Putnis, C. V. (2007) 'The mechanism of reequilibration of solids in the presence of a fluid phase', *Journal of Solid State Chemistry*, 180(5), pp. 1783–1786. doi: 10.1016/j.jssc.2007.03.023.
- Ree, J. H., Kim, H. S., Han, R. and Jung, H. (2005) 'Grain-size reduction of feldspars by fracturing and neocrystallization in a low-grade granitic mylonite and its rheological effect', *Tectonophysics*, 407(3–4), pp. 227–237. doi: 10.1016/j.tecto.2005.07.010.
- Reid, D., Erlank, A. J. and Moyes, A. (1987) 'The Orange River Group: a major Proterozoic calcalkaline volcanic belt in the western Namaqua Province, southern Africa', *Geological Society Special Publication*, 33(33), pp. 327–346. doi: 10.1144/GSL.SP.1987.033.01.22.
- Reid, D. L. (1997) 'Sm-Nd age and REE geochemistry of Proterozoic arc-related igneous rocks in the Richtersveld Subprovince, Namaqua Mobile Belt, Southern Africa', *Journal of African Earth Sciences*, 24(4), pp. 621–633.
- Remmert, P., Heinrich, W., Wunder, B., Morales, L., Wirth, R., Rhede, D. and Abart, R. (2018) 'Synthesis of monticellite–forsterite and merwinite–forsterite symplectites in the CaO–MgO–SiO₂ model system: influence of temperature and water content on microstructure evolution', *Contributions to Mineralogy and Petrology*. Springer Berlin Heidelberg, 173(1), p. 5. doi: 10.1007/s00410-017-1429-y.
- Rennie, S. F., Fagereng, A. and Diener, J. F. A. (2013) 'Strain distribution within a km-scale, mid-crustal shear zone: The Kuckaus Mylonite Zone, Namibia', *Journal of Structural Geology*, 56(February 2016), pp. 57–69. doi: 10.1016/j.jsg.2013.09.001.
- Robb, L. J., Armstrong, R. A. and Waters, D. J. (1999) 'The History of Granulite-Facies Metamorphism and Crustal Growth from Single Zircon U – Pb Geochronology : Namaqualand , South Africa', *Journal of Petrology*, 40(12), pp. 1747–1770.
- Ruiz-Agudo, E., Putnis, C. V. and Putnis, A. (2014) 'Coupled dissolution and precipitation at mineral-fluid interfaces', *Chemical Geology*. Elsevier B.V., 383, pp. 132–146. doi: 10.1016/j.chemgeo.2014.06.007.
- Rybacki, E. and Dresen, G. (2000) 'Dislocation and diffusion creep of synthetic anorthite aggregates',

Journal of Geophysical Research: Solid Earth, 105(B11), pp. 26017–26036. doi: 10.1029/2000JB900223.

Schwantke, A. (1909) 'Die Beimischung von Ca im Kalifeldspat und die Myrmekitbildung', *Zentralblatt für Geologie und Palaontologie*, pp. 311–316.

Shigematsu, N., Fujimoto, K., Ohtani, T. and Goto, K. (2004) 'Ductile fracture of fine-grained plagioclase in the brittle-plastic transition regime: Implication for earthquake source nucleation', *Earth and Planetary Science Letters*, 222(3–4), pp. 1007–1022. doi: 10.1016/j.epsl.2004.04.001.

Simpson, C. (1985) 'Deformation of granitic rocks across the brittle--ductile transition', *Journal of Structural Geology*, 7(5), p. 503 to 511.

Simpson, C. and Wintsch, R. P. (1989) 'Evidence for deformation-induced K-feldspar replacement by myrmekite', *Journal of Metamorphic Geology*, 7(2), pp. 261–275. doi: 10.1111/j.1525-1314.1989.tb00588.x.

Spruzeniece, L., Piazzolo, S., Daczko, N. R., Kilburn, M. R. and Putnis, A. (2017) 'Symplectite formation in the presence of a reactive fluid: insights from hydrothermal experiments', *Journal of Metamorphic Geology*, 35(3), pp. 281–299. doi: 10.1111/jmg.12231.

Srivastava, P. and Mitra, G. (1996) 'Deformation mechanisms and inverted thermal profile in the North Almora Thrust mylonite zone, Kumaon Lesser Himalaya, India', *Journal of Structural Geology*, 18(1), pp. 27–39.

Stel, H. (1986) 'The effect of cyclic operation of brittle and ductile deformation on the metamorphic assemblage in cataclases and mylonites', *Pure and Applied Geophysics PAGEOPH*, 124(1–2), pp. 289–307. doi: 10.1007/BF00875729.

Stel, H. and Breedveld, M. (1990) 'Crystallographic orientation patterns of myrmekitic quartz: a fabric memory in quartz ribbon-bearing gneisses', *Journal of Structural Geology*, 12(1), pp. 19–28. doi: 10.1016/0191-8141(90)90045-Z.

Stipp, M. and Kunze, K. (2008) 'Dynamic recrystallization near the brittle-plastic transition in naturally and experimentally deformed quartz aggregates', *Tectonophysics*, 448(1–4), pp. 77–97. doi: 10.1016/j.tecto.2007.11.041.

Stipp, M., Stünitz, H., Heilbronner, R. and Schmid, S. M. (2002a) 'Dynamic recrystallization of quartz: correlation between natural and experimental conditions', *Geological Society, London, Special Publications*, 200(1), pp. 171–190. doi: 10.1144/GSL.SP.2001.200.01.11.

Stipp, M., Stünitz, H., Heilbronner, R. and Schmid, S. M. (2002b) 'The eastern Tonale fault zone: a "natural laboratory" for crystal plastic deformation of quartz over a temperature range from 250 to 700 °C', *Journal of Structural Geology*. Pergamon, 24(12), pp. 1861–1884. doi: 10.1016/S0191-8141(02)00035-4.

Stipp, M., Tullis, J. and Behrens, H. (2006) 'Effect of water on the dislocation creep microstructure and flow stress of quartz and implications for the recrystallized grain size piezometer', *Journal of Geophysical Research: Solid Earth*, 111(4), pp. 1–19. doi: 10.1029/2005JB003852.

Stünitz, H. and Fitz Gerald, J. D. (1993) 'Deformation of granitoids at low metamorphic grades: II. Granular flow in albite rich mylonites', *Tectonophysics*, 221, pp. 299–324.

Thomas, R. J., Agenbacht, A. L. D., Cornell, D. H. and Moore, J. M. (1994) 'The Kibaran of southern Africa: Tectonic evolution and metallogeny', *Ore Geology Reviews*, 9(2), pp. 131–160. doi: 10.1016/0169-1368(94)90025-6.

De Toni, G. B., Bitencourt, M. F. and Nardi, L. V. S. (2016) 'Strain partitioning into dry and wet zones

and the formation of Ca-rich myrmekite in syntectonic syenites: A case for melt-assisted dissolution-replacement creep under granulite facies conditions', *Journal of Structural Geology*. Elsevier Ltd, 91, pp. 88–101. doi: 10.1016/j.jsg.2016.08.002.

Toogood, D. J. (1976) 'Structural and Metamorphic Evolution of a Gneiss Terrain in the Namaqua Belt Near Onseepkans, South West Africa', *Bulletin of the Precambrian Research unit*, pp. 1–189.

Tsurumi, J., Hosonuma, H. and Kanagawa, K. (2002) 'Strain localization due to a positive feedback of deformation and myrmekite-forming reaction in granite and aplite mylonites along the Hatagawa Shear Zone of NE Japan', *Journal of Structural Geology*, 25(4), pp. 557–574. doi: 10.1016/S0191-8141(02)00048-2.

Vernon, R. H. (1999) 'Flame perthite in metapelitic gneisses at Cooma, SE Australia', *American Mineralogist*, 84(11–12), pp. 1760–1765.

Vernon, R. H. (2004) 'Microstructures of deformed rocks', in *A Practical Guide to Rock Microstructure*, pp. 295–474. doi: 10.1017/CBO9780511807206.006.

Whitney, J. A. and Stormer, J. C. (1977) 'The distribution of NaAlSi₃O₈ between coexisting microcline and plagioclase and its effect on geothermometric calculations', *American Mineralogist*, 62(1974), pp. 687–691.

Wintsch, R. P. and Yi, K. (2002) 'Dissolution and replacement creep: a significant deformation mechanism in mid-crustal rocks', *Journal of Structural Geology*, 24, pp. 1179–1193.

Wirth, R. and Voll, G. (1987) 'Cellular intergrowth between quartz and analogue of discontinuous precipitation in metal alloys', *Journal of Material Science*, 22, pp. 1913–1918.

Wu, W., Liu, J., Zhang, L., Qi, Y. and Ling, C. (2017) 'Characterizing a middle to upper crustal shear zone: Microstructures, quartz c-axis fabrics, deformation temperatures and flow vorticity analysis of the northern Ailao Shan-Red River shear zone, China', *Journal of Asian Earth Sciences*. Elsevier Ltd, 139, pp. 95–114. doi: 10.1016/j.jseaes.2016.12.026.

Yardley, B. (2013) 'The Chemical Composition of Metasomatic Fluids in the Crust', in Harlov, D. E. and Austrheim, H. (eds) *Metasomatism and the Chemical Transformation of Rock- The Role of Fluids in Terrestrial and Extraterrestrial Processes*. doi: 10.4108/eai.3-12-2015.2262440.

Yardley, B., Bennett, A. and Banks, D. (2003) 'Controls on the chemical composition of crustal brines', *Journal of Geochemical Exploration*, 79, pp. 133–135. doi: 10.1016/S0375.

Yin, C., Zhang, B., Han, B. F., Zhang, J., Wang, Y. and Ai, S. (2017) 'Structural analysis and deformation characteristics of the Yingba metamorphic core complex, northwestern margin of the North China craton, NE Asia', *Journal of Structural Geology*. Elsevier Ltd, 94, pp. 195–212. doi: 10.1016/j.jsg.2016.11.011.

5 APPENDIXES

5.1 MUSCOVITE DATA

Type	Fish	Fish	Fish	Fish	Fish	Fish	Fish	Fish	Fish	Fish	Fish	Fish
SiO ₂	46.050	46.700	45.850	46.210	46.480	45.570	46.030	46.130	46.520	46.960	45.770	46.750
Al ₂ O ₃	32.590	32.700	32.470	32.680	32.990	32.900	32.890	32.250	31.880	31.790	32.530	32.040
MgO	0.725	0.817	0.737	0.746	0.733	0.647	0.713	0.938	1.041	1.080	0.780	1.012
K ₂ O	11.170	11.200	11.490	11.310	11.310	11.460	11.320	11.520	11.500	11.440	11.550	11.350
MnO	0.005	0.010	0.000	0.026	0.020	0.021	0.007	0.012	0.020	0.040	0.027	0.010
FeO	3.190	3.420	3.320	3.420	3.410	3.530	3.350	3.560	3.500	3.830	3.260	3.540
Na ₂ O	0.299	0.242	0.258	0.270	0.242	0.251	0.243	0.236	0.215	0.202	0.273	0.205
F	0.075	0.090	0.058	0.106	0.086	0.091	0.097	0.149	0.099	0.121	0.110	0.148
TiO ₂	1.643	1.080	1.602	1.395	0.881	1.351	1.542	0.871	1.195	0.893	1.424	0.992
Cl	0.000	0.000	0.003	0.001	0.000	0.000	0.000	0.000	0.002	0.007	0.001	0.000
CaO	0.003	0.003	0.000	0.003	0.003	0.005	0.006	0.010	0.003	0.003	0.003	0.002
Total	95.750	96.262	95.786	96.166	96.154	95.826	96.198	95.676	95.975	96.366	95.727	96.048
Cations pfu												
Si	3.10	3.13	3.09	3.10	3.12	3.08	3.09	3.12	3.13	3.15	3.09	3.14
Ti	0.08	0.05	0.08	0.07	0.04	0.07	0.08	0.04	0.06	0.05	0.07	0.05
Al	2.59	2.58	2.58	2.59	2.61	2.62	2.60	2.57	2.53	2.52	2.59	2.54
Fe	0.18	0.19	0.19	0.19	0.19	0.20	0.19	0.20	0.20	0.22	0.18	0.20
Mg	0.07	0.08	0.07	0.07	0.07	0.07	0.07	0.09	0.10	0.11	0.08	0.10
Mn	0.00	0.00	0.00	0.00	0.00	0.00	0.00	0.00	0.00	0.00	0.00	0.00
Ca	0.00	0.00	0.00	0.00	0.00	0.00	0.00	0.00	0.00	0.00	0.00	0.00
Na	0.04	0.03	0.03	0.04	0.03	0.03	0.03	0.03	0.03	0.03	0.04	0.03
K	0.96	0.96	0.99	0.97	0.97	0.99	0.97	0.99	0.99	0.98	1.00	0.97
F	0.02	0.02	0.01	0.02	0.02	0.02	0.02	0.03	0.02	0.03	0.02	0.03
Cl	0.00	0.00	0.00	0.00	0.00	0.00	0.00	0.00	0.00	0.00	0.00	0.00
Total positive cations	7.02	7.02	7.04	7.03	7.03	7.05	7.03	7.06	7.05	7.05	7.05	7.04

Type	Fish	Fish	Fish	Fish	Fish	Fish	Fish	Fish	Fish	Fish	Fish	Fish
SiO ₂	46.510	45.970	45.920	46.440	46.310	45.640	46.380	46.860	46.380	46.440	45.890	47.070
Al ₂ O ₃	31.920	32.910	33.460	32.000	33.060	33.260	32.190	31.800	32.720	32.530	32.510	31.830
MgO	0.909	0.725	0.655	0.962	0.706	0.611	0.856	1.055	0.754	0.770	0.693	1.165
K ₂ O	11.410	11.300	11.220	11.370	11.280	11.380	11.340	11.360	11.420	11.280	11.120	11.350
MnO	0.039	0.025	0.021	0.015	0.000	0.011	0.008	0.010	0.030	0.025	0.000	0.041
FeO	3.320	3.080	3.080	3.330	3.140	2.900	3.510	3.440	3.300	3.380	3.100	3.680
Na ₂ O	0.228	0.334	0.409	0.200	0.299	0.360	0.232	0.235	0.251	0.252	0.278	0.198
F	0.054	0.096	0.087	0.113	0.081	0.071	0.090	0.102	0.043	0.087	0.133	0.138
TiO ₂	1.405	1.560	1.209	0.833	1.073	1.342	1.587	0.966	1.142	1.639	1.236	0.859
Cl	0.000	0.001	0.000	0.001	0.003	0.011	0.000	0.000	0.008	0.003	0.002	0.000
CaO	0.006	0.000	0.003	0.036	0.000	0.006	0.006	0.006	0.004	0.015	0.002	0.000
Total	95.800	96.001	96.064	95.299	95.952	95.592	96.200	95.835	96.053	96.419	94.964	96.331
Cations pfu												
Si	3.13	3.09	3.08	3.15	3.11	3.08	3.12	3.16	3.12	3.11	3.11	3.16
Ti	0.07	0.08	0.06	0.04	0.05	0.07	0.08	0.05	0.06	0.08	0.06	0.04
Al	2.54	2.61	2.65	2.55	2.62	2.64	2.55	2.52	2.59	2.57	2.60	2.52
Fe	0.19	0.17	0.17	0.19	0.18	0.16	0.20	0.19	0.19	0.19	0.18	0.21
Mg	0.09	0.07	0.07	0.10	0.07	0.06	0.09	0.11	0.08	0.08	0.07	0.12
Mn	0.00	0.00	0.00	0.00	0.00	0.00	0.00	0.00	0.00	0.00	0.00	0.00
Ca	0.00	0.00	0.00	0.00	0.00	0.00	0.00	0.00	0.00	0.00	0.00	0.00
Na	0.03	0.04	0.05	0.03	0.04	0.05	0.03	0.03	0.03	0.03	0.04	0.03
K	0.98	0.97	0.96	0.98	0.97	0.98	0.97	0.98	0.98	0.96	0.96	0.97
F	0.01	0.02	0.02	0.02	0.02	0.02	0.02	0.02	0.01	0.02	0.03	0.03
Cl	0.00	0.00	0.00	0.00	0.00	0.00	0.00	0.00	0.00	0.00	0.00	0.00
Total positive cations	7.03	7.03	7.04	7.04	7.03	7.04	7.03	7.04	7.04	7.02	7.02	7.04

Type	Fish	Fish	Fish	Fish	Fish	Fish	Fish	Fish	Fish	Fish	Fish	Fish
SiO ₂	46.150	46.380	45.720	45.880	45.760	45.510	46.080	46.340	46.450	45.860	46.590	46.130
Al ₂ O ₃	31.750	32.740	32.800	32.850	32.970	32.960	32.350	32.990	33.190	32.680	31.650	32.710
MgO	0.840	0.705	0.721	0.721	0.656	0.675	0.796	0.688	0.667	0.685	1.024	0.697
K ₂ O	11.150	11.310	11.530	11.590	11.320	11.430	11.470	11.330	11.360	11.370	11.360	11.150
MnO	0.027	0.016	0.007	0.000	0.007	0.021	0.013	0.012	0.000	0.024	0.000	0.000
FeO	3.470	3.340	3.270	3.240	3.040	3.130	3.150	3.310	3.050	3.010	3.130	3.270
Na ₂ O	0.265	0.232	0.221	0.219	0.306	0.334	0.269	0.266	0.304	0.264	0.213	0.279
F	0.090	0.066	0.086	0.051	0.130	0.089	0.125	0.074	0.097	0.074	0.122	0.082
TiO ₂	1.700	1.384	1.165	1.142	1.544	1.637	1.545	0.985	1.181	1.830	1.474	1.566
Cl	0.004	0.007	0.005	0.001	0.000	0.001	0.001	0.000	0.000	0.001	0.000	0.007
CaO	0.000	0.004	0.006	0.003	0.024	0.000	0.005	0.000	0.000	0.008	0.008	0.000
Total	95.447	96.184	95.531	95.697	95.756	95.787	95.803	95.995	96.300	95.804	95.571	95.891
Cations pfu												
Si	3.12	3.11	3.09	3.10	3.08	3.07	3.11	3.11	3.11	3.09	3.14	3.10
Ti	0.09	0.07	0.06	0.06	0.08	0.08	0.08	0.05	0.06	0.09	0.07	0.08
Al	2.53	2.59	2.62	2.61	2.62	2.62	2.57	2.61	2.62	2.59	2.52	2.59
Fe	0.20	0.19	0.19	0.18	0.17	0.18	0.18	0.19	0.17	0.17	0.18	0.18
Mg	0.08	0.07	0.07	0.07	0.07	0.07	0.08	0.07	0.07	0.07	0.10	0.07
Mn	0.00	0.00	0.00	0.00	0.00	0.00	0.00	0.00	0.00	0.00	0.00	0.00
Ca	0.00	0.00	0.00	0.00	0.00	0.00	0.00	0.00	0.00	0.00	0.00	0.00
Na	0.03	0.03	0.03	0.03	0.04	0.04	0.04	0.03	0.04	0.03	0.03	0.04
K	0.96	0.97	1.00	1.00	0.97	0.98	0.99	0.97	0.97	0.98	0.98	0.96
F	0.02	0.01	0.02	0.01	0.03	0.02	0.03	0.02	0.02	0.02	0.03	0.02
Cl	0.00	0.00	0.00	0.00	0.00	0.00	0.00	0.00	0.00	0.00	0.00	0.00
Total positive cations	7.02	7.02	7.05	7.05	7.03	7.05	7.04	7.03	7.03	7.03	7.02	7.02

Type	Fish	Fish	Fish	Fish	Fish	Fish	Fish	Fish	Fish	Fish	Fish	Fish
SiO ₂	45.920	45.880	46.640	45.940	46.490	47.130	45.940	46.290	46.910	46.260	46.420	46.810
Al ₂ O ₃	33.020	32.870	31.660	32.760	32.760	32.420	32.740	32.520	33.130	33.060	32.550	32.290
MgO	0.645	0.727	1.035	0.707	0.713	0.980	0.691	0.756	0.723	0.669	0.729	0.939
K ₂ O	11.160	11.410	11.040	11.300	11.300	10.890	11.300	11.290	11.260	11.360	11.110	11.220
MnO	0.000	0.027	0.012	0.029	0.022	0.010	0.007	0.021	0.007	0.013	0.006	0.042
FeO	3.110	3.220	3.640	3.250	3.270	3.080	3.130	2.970	2.620	3.240	3.100	3.400
Na ₂ O	0.401	0.222	0.204	0.267	0.246	0.219	0.263	0.282	0.248	0.240	0.327	0.214
F	0.042	0.124	0.093	0.086	0.064	0.090	0.087	0.085	0.081	0.045	0.067	0.072
TiO ₂	1.664	1.236	0.861	1.489	1.226	0.975	1.240	1.577	1.425	1.062	1.623	1.146
Cl	0.003	0.000	0.001	0.007	0.000	0.002	0.007	0.000	0.000	0.003	0.000	0.000
CaO	0.000	0.003	0.033	0.005	0.008	0.009	0.002	0.003	0.000	0.013	0.000	0.012
Total	95.965	95.718	95.219	95.839	96.099	95.804	95.406	95.794	96.403	95.965	95.932	96.145
Cations pfu												
Si	3.08	3.10	3.16	3.09	3.12	3.16	3.11	3.11	3.12	3.11	3.12	3.14
Ti	0.08	0.06	0.04	0.08	0.06	0.05	0.06	0.08	0.07	0.05	0.08	0.06
Al	2.61	2.61	2.53	2.60	2.59	2.56	2.61	2.58	2.60	2.62	2.57	2.55
Fe	0.17	0.18	0.21	0.18	0.18	0.17	0.18	0.17	0.15	0.18	0.17	0.19
Mg	0.06	0.07	0.10	0.07	0.07	0.10	0.07	0.08	0.07	0.07	0.07	0.09
Mn	0.00	0.00	0.00	0.00	0.00	0.00	0.00	0.00	0.00	0.00	0.00	0.00
Ca	0.00	0.00	0.00	0.00	0.00	0.00	0.00	0.00	0.00	0.00	0.00	0.00
Na	0.05	0.03	0.03	0.03	0.03	0.03	0.03	0.04	0.03	0.03	0.04	0.03
K	0.96	0.98	0.95	0.97	0.97	0.93	0.97	0.97	0.96	0.97	0.95	0.96
F	0.01	0.03	0.02	0.02	0.01	0.02	0.02	0.02	0.02	0.01	0.01	0.02
Cl	0.00	0.00	0.00	0.00	0.00	0.00	0.00	0.00	0.00	0.00	0.00	0.00
Total positive cations	7.03	7.04	7.02	7.03	7.02	6.99	7.03	7.02	7.00	7.03	7.01	7.02

Type	Fish	Fish	Fish	Fish	Fish	Fish	Fish	Fish	Fol	Fol	Fol	Fol
SiO ₂	46.860	46.330	46.030	46.010	46.410	46.370	46.080	45.980	46.280	46.510	46.550	46.820
Al ₂ O ₃	31.780	32.840	32.480	32.190	33.360	32.910	32.440	33.200	32.370	32.100	32.130	31.070
MgO	1.018	0.699	0.753	1.038	0.664	0.700	0.801	0.625	0.808	0.836	0.994	1.334
K ₂ O	11.130	11.320	11.560	11.470	11.120	11.340	11.510	11.360	11.420	11.350	11.320	11.030
MnO	0.020	0.026	0.001	0.040	0.014	0.019	0.002	0.011	0.021	0.031	0.029	0.022
FeO	3.680	3.250	3.440	3.580	3.060	3.300	3.110	3.300	3.520	3.320	3.700	3.980
Na ₂ O	0.198	0.267	0.227	0.228	0.331	0.306	0.244	0.252	0.213	0.212	0.190	0.211
F	0.087	0.049	0.064	0.104	0.066	0.045	0.043	0.032	0.090	0.081	0.106	0.098
TiO ₂	1.271	1.384	1.340	0.853	1.301	1.267	1.540	1.338	1.267	1.422	0.874	0.768
Cl	0.003	0.000	0.000	0.000	0.000	0.000	0.000	0.003	0.000	0.003	0.005	0.012
CaO	0.012	0.006	0.001	0.000	0.012	0.009	0.003	0.007	0.006	0.005	0.023	0.035
Total	96.059	96.170	95.895	95.513	96.338	96.266	95.774	96.107	95.995	95.869	95.920	95.380
Cations pfu												
Si	3.15	3.11	3.10	3.12	3.10	3.11	3.11	3.09	3.12	3.13	3.14	3.17
Ti	0.06	0.07	0.07	0.04	0.07	0.06	0.08	0.07	0.06	0.07	0.04	0.04
Al	2.52	2.60	2.58	2.57	2.63	2.60	2.58	2.63	2.57	2.55	2.55	2.48
Fe	0.21	0.18	0.19	0.20	0.17	0.18	0.18	0.19	0.20	0.19	0.21	0.23
Mg	0.10	0.07	0.08	0.10	0.07	0.07	0.08	0.06	0.08	0.08	0.10	0.13
Mn	0.00	0.00	0.00	0.00	0.00	0.00	0.00	0.00	0.00	0.00	0.00	0.00
Ca	0.00	0.00	0.00	0.00	0.00	0.00	0.00	0.00	0.00	0.00	0.00	0.00
Na	0.03	0.03	0.03	0.03	0.04	0.04	0.03	0.03	0.03	0.03	0.02	0.03
K	0.95	0.97	0.99	0.99	0.95	0.97	0.99	0.97	0.98	0.97	0.97	0.95
F	0.02	0.01	0.01	0.02	0.01	0.01	0.01	0.01	0.02	0.02	0.02	0.02
Cl	0.00	0.00	0.00	0.00	0.00	0.00	0.00	0.00	0.00	0.00	0.00	0.00
Total positive cations	7.02	7.03	7.05	7.06	7.02	7.03	7.04	7.04	7.04	7.02	7.04	7.04

Type	Fol	Fol	Fol	Fol	Fol	Fol	Fol	Fol	Fol	Fol	Fol	Fol
SiO ₂	46.920	46.120	46.510	46.050	45.550	46.120	46.470	47.800	46.400	46.750	46.410	46.450
Al ₂ O ₃	31.450	32.270	31.740	32.530	31.260	32.760	33.440	30.930	31.850	31.000	32.080	32.720
MgO	1.162	0.814	1.020	0.785	0.954	0.674	0.787	1.124	1.045	1.127	0.974	0.744
K ₂ O	11.530	11.550	11.530	11.400	11.180	11.270	11.650	11.300	11.380	11.430	11.470	11.340
MnO	0.039	0.013	0.033	0.011	0.016	0.002	0.027	0.026	0.009	0.026	0.003	0.009
FeO	3.940	3.780	3.620	3.100	4.340	3.200	2.970	3.680	3.540	3.760	3.490	3.470
Na ₂ O	0.206	0.235	0.213	0.305	0.224	0.254	0.243	0.187	0.255	0.195	0.212	0.234
F	0.076	0.108	0.111	0.087	0.101	0.014	0.095	0.078	0.080	0.087	0.119	0.089
TiO ₂	0.915	1.557	1.136	1.175	0.795	1.194	0.540	0.784	1.223	0.788	0.938	1.071
Cl	0.000	0.000	0.010	0.001	0.007	0.002	0.001	0.001	0.009	0.002	0.001	0.000
CaO	0.001	0.010	0.022	0.010	0.036	0.019	0.016	0.031	0.009	0.020	0.021	0.012
Total	96.240	96.458	95.944	95.454	94.463	95.508	96.239	95.940	95.798	95.185	95.719	96.139
Cations pfu												
Si	3.16	3.10	3.14	3.11	3.13	3.11	3.11	3.21	3.13	3.18	3.13	3.12
Ti	0.05	0.08	0.06	0.06	0.04	0.06	0.03	0.04	0.06	0.04	0.05	0.05
Al	2.50	2.56	2.52	2.59	2.53	2.60	2.64	2.45	2.53	2.48	2.55	2.59
Fe	0.22	0.21	0.20	0.18	0.25	0.18	0.17	0.21	0.20	0.21	0.20	0.19
Mg	0.12	0.08	0.10	0.08	0.10	0.07	0.08	0.11	0.11	0.11	0.10	0.07
Mn	0.00	0.00	0.00	0.00	0.00	0.00	0.00	0.00	0.00	0.00	0.00	0.00
Ca	0.00	0.00	0.00	0.00	0.00	0.00	0.00	0.00	0.00	0.00	0.00	0.00
Na	0.03	0.03	0.03	0.04	0.03	0.03	0.03	0.02	0.03	0.03	0.03	0.03
K	0.99	0.99	0.99	0.98	0.98	0.97	1.00	0.97	0.98	0.99	0.99	0.97
F	0.02	0.02	0.02	0.02	0.02	0.00	0.02	0.02	0.02	0.02	0.03	0.02
Cl	0.00	0.00	0.00	0.00	0.00	0.00	0.00	0.00	0.00	0.00	0.00	0.00
Total positive cations	7.06	7.05	7.05	7.04	7.07	7.03	7.05	7.02	7.05	7.05	7.05	7.03

Type	Fol	Fol	Fol	Near myr	Near myr	Near myr	Near myr	Near myr	Near myr	Near myr	Near myr	Near myr
SiO ₂	46.660	49.560	47.110	46.310	46.170	46.610	46.330	46.270	46.810	46.360	46.530	45.770
Al ₂ O ₃	31.520	30.690	31.490	31.780	32.440	32.050	31.940	32.150	31.990	32.460	31.880	32.920
MgO	0.998	1.113	1.065	1.026	0.907	1.004	1.012	0.978	1.084	0.913	1.048	0.694
K ₂ O	11.360	10.910	11.320	11.550	11.490	11.560	11.250	11.470	11.530	11.540	11.450	11.570
MnO	0.014	0.008	0.019	0.023	0.016	0.023	0.000	0.012	0.041	0.016	0.022	0.025
FeO	3.420	3.560	3.590	3.600	3.460	3.450	3.410	3.370	3.300	3.210	3.670	3.400
Na ₂ O	0.191	0.186	0.396	0.209	0.221	0.212	0.187	0.219	0.227	0.198	0.187	0.243
F	0.054	0.100	0.125	0.085	0.084	0.108	0.076	0.111	0.075	0.075	0.069	0.051
TiO ₂	1.225	0.617	0.919	0.989	0.758	0.769	0.719	0.883	0.796	0.879	0.758	1.514
Cl	0.001	0.000	0.005	0.004	0.004	0.002	0.006	0.001	0.001	0.003	0.010	0.000
CaO	0.012	0.025	0.014	0.016	0.007	0.017	0.030	0.002	0.000	0.013	0.034	0.017
Total	95.454	96.769	96.054	95.592	95.556	95.806	94.960	95.465	95.853	95.668	95.658	96.205
Cations pfu												
Si	3.15	3.28	3.17	3.14	3.12	3.14	3.15	3.13	3.15	3.13	3.15	3.08
Ti	0.06	0.03	0.05	0.05	0.04	0.04	0.04	0.04	0.04	0.04	0.04	0.08
Al	2.51	2.40	2.50	2.54	2.59	2.55	2.56	2.56	2.54	2.58	2.54	2.61
Fe	0.19	0.20	0.20	0.20	0.20	0.19	0.19	0.19	0.19	0.18	0.21	0.19
Mg	0.10	0.11	0.11	0.10	0.09	0.10	0.10	0.10	0.11	0.09	0.11	0.07
Mn	0.00	0.00	0.00	0.00	0.00	0.00	0.00	0.00	0.00	0.00	0.00	0.00
Ca	0.00	0.00	0.00	0.00	0.00	0.00	0.00	0.00	0.00	0.00	0.00	0.00
Na	0.02	0.02	0.05	0.03	0.03	0.03	0.02	0.03	0.03	0.03	0.02	0.03
K	0.98	0.92	0.97	1.00	0.99	0.99	0.97	0.99	0.99	0.99	0.99	0.99
F	0.01	0.02	0.03	0.02	0.02	0.02	0.02	0.02	0.02	0.02	0.01	0.01
Cl	0.00	0.00	0.00	0.00	0.00	0.00	0.00	0.00	0.00	0.00	0.00	0.00
Total positive cations	7.03	6.96	7.05	7.06	7.06	7.05	7.04	7.05	7.05	7.05	7.05	7.05

Type	Near myr	Near myr	Near myr	Near Myr	Near myr	Near myr	Near myr	Near myr	Near myr	Near myr	Near myr	Near myr
SiO ₂	47.090	46.730	46.610	46.280	46.840	45.970	46.310	46.500	46.610	45.850	46.260	47.170
Al ₂ O ₃	31.820	31.840	32.170	32.030	31.650	33.010	31.840	32.640	32.130	33.140	33.030	31.000
MgO	1.035	1.108	0.927	0.968	1.113	0.724	1.108	0.825	1.004	0.636	0.724	1.071
K ₂ O	11.470	11.340	11.430	11.400	11.320	11.340	11.050	11.270	11.410	11.550	11.520	11.720
MnO	0.024	0.041	0.013	0.039	0.026	0.011	0.028	0.005	0.011	0.000	0.023	0.018
FeO	3.900	3.430	3.350	3.520	3.580	3.140	3.680	3.160	3.250	3.350	3.310	3.520
Na ₂ O	0.170	0.188	0.225	0.212	0.218	0.211	0.201	0.278	0.230	0.243	0.227	0.252
F	0.071	0.093	0.115	0.095	0.097	0.033	0.071	0.091	0.089	0.075	0.036	0.104
TiO ₂	1.397	0.883	1.388	0.869	0.764	1.010	0.725	1.123	0.815	1.012	0.782	0.712
Cl	0.000	0.000	0.001	0.005	0.002	0.003	0.009	0.008	0.003	0.003	0.000	0.021
CaO	0.041	0.022	0.016	0.014	0.027	0.018	0.035	0.000	0.000	0.013	0.021	0.045
Total	97.016	95.675	96.245	95.431	95.637	95.469	95.055	95.899	95.553	95.871	95.933	95.632
Cations pfu												
Si	3.14	3.15	3.13	3.13	3.16	3.10	3.14	3.12	3.15	3.09	3.11	3.19
Ti	0.07	0.04	0.07	0.04	0.04	0.05	0.04	0.06	0.04	0.05	0.04	0.04
Al	2.50	2.53	2.54	2.56	2.52	2.63	2.55	2.58	2.56	2.63	2.62	2.47
Fe	0.22	0.19	0.19	0.20	0.20	0.18	0.21	0.18	0.18	0.19	0.19	0.20
Mg	0.10	0.11	0.09	0.10	0.11	0.07	0.11	0.08	0.10	0.06	0.07	0.11
Mn	0.00	0.00	0.00	0.00	0.00	0.00	0.00	0.00	0.00	0.00	0.00	0.00
Ca	0.00	0.00	0.00	0.00	0.00	0.00	0.00	0.00	0.00	0.00	0.00	0.00
Na	0.02	0.02	0.03	0.03	0.03	0.03	0.03	0.04	0.03	0.03	0.03	0.03
K	0.98	0.98	0.98	0.98	0.97	0.98	0.96	0.97	0.98	0.99	0.99	1.01
F	0.01	0.02	0.02	0.02	0.02	0.01	0.02	0.02	0.02	0.02	0.01	0.02
Cl	0.00	0.00	0.00	0.00	0.00	0.00	0.00	0.00	0.00	0.00	0.00	0.00
Total positive cations	7.04	7.04	7.03	7.05	7.04	7.04	7.04	7.03	7.04	7.05	7.05	7.06

Type	Near myr	Near myr	Near myr	Near myr	Near myr	Near myr	Near myr	Near myr	Near myr	Near myr	Near myr	Near myr
SiO ₂	46.510	46.080	46.670	46.390	46.630	45.940	47.010	46.580	47.070	47.080	46.840	47.210
Al ₂ O ₃	31.990	32.230	32.180	32.670	31.870	30.870	30.970	32.940	31.480	31.900	31.610	31.970
MgO	1.025	0.966	1.046	0.960	1.089	1.351	1.325	0.755	1.083	1.060	1.058	0.912
K ₂ O	11.270	11.470	11.400	11.430	11.370	10.990	11.240	11.530	11.350	11.360	11.240	11.030
MnO	0.009	0.032	0.001	0.019	0.010	0.042	0.025	0.020	0.022	0.016	0.004	0.012
FeO	3.440	3.450	3.510	2.920	3.260	4.780	3.910	3.290	3.740	3.430	3.590	3.120
Na ₂ O	0.181	0.210	0.188	0.213	0.193	0.203	0.192	0.212	0.207	0.189	0.223	0.210
F	0.052	0.104	0.056	0.057	0.064	0.072	0.135	0.087	0.053	0.112	0.096	0.057
TiO ₂	0.756	0.597	0.556	0.861	0.740	1.051	0.756	0.646	0.662	0.694	0.888	0.689
Cl	0.000	0.019	0.006	0.000	0.009	0.003	0.004	0.000	0.002	0.005	0.004	0.007
CaO	0.030	0.033	0.022	0.001	0.015	0.016	0.030	0.021	0.031	0.022	0.038	0.028
Total	95.263	95.191	95.634	95.521	95.250	95.319	95.598	96.081	95.700	95.867	95.591	95.244
Cations pfu												
Si	3.15	3.13	3.15	3.13	3.16	3.13	3.18	3.13	3.18	3.17	3.16	3.18
Ti	0.04	0.03	0.03	0.04	0.04	0.05	0.04	0.03	0.03	0.04	0.05	0.03
Al	2.55	2.58	2.56	2.60	2.54	2.48	2.47	2.61	2.50	2.53	2.52	2.54
Fe	0.19	0.20	0.20	0.16	0.18	0.27	0.22	0.18	0.21	0.19	0.20	0.18
Mg	0.10	0.10	0.11	0.10	0.11	0.14	0.13	0.08	0.11	0.11	0.11	0.09
Mn	0.00	0.00	0.00	0.00	0.00	0.00	0.00	0.00	0.00	0.00	0.00	0.00
Ca	0.00	0.00	0.00	0.00	0.00	0.00	0.00	0.00	0.00	0.00	0.00	0.00
Na	0.02	0.03	0.02	0.03	0.03	0.03	0.03	0.03	0.03	0.02	0.03	0.03
K	0.97	0.99	0.98	0.98	0.98	0.96	0.97	0.99	0.98	0.97	0.97	0.95
F	0.01	0.02	0.01	0.01	0.01	0.02	0.03	0.02	0.01	0.02	0.02	0.01
Cl	0.00	0.00	0.00	0.00	0.00	0.00	0.00	0.00	0.00	0.00	0.00	0.00
Total positive cations	7.04	7.06	7.05	7.04	7.04	7.06	7.04	7.04	7.04	7.03	7.03	7.00

Type	Near myr	Near myr	Near myr	Near myr	Near myr	Near myr	Near myr	Near myr	Near myr	Near myr	Near myr	Near myr
SiO ₂	46.360	47.950	47.190	48.440	48.000	46.870	46.340	46.220	47.010	47.140	46.090	47.210
Al ₂ O ₃	31.620	31.830	32.060	31.160	31.470	31.970	32.550	32.380	31.960	31.650	32.210	31.470
MgO	1.055	1.047	1.054	1.041	1.001	1.006	0.739	0.753	1.065	1.047	0.893	1.151
K ₂ O	11.330	11.330	11.400	10.960	10.880	11.370	11.280	11.160	11.280	11.120	10.980	11.240
MnO	0.002	0.002	0.017	0.001	0.004	0.017	0.018	0.000	0.023	0.022	0.019	0.010
FeO	3.460	3.210	3.160	3.290	3.070	3.660	2.990	3.230	3.430	3.480	3.470	3.640
Na ₂ O	0.212	0.220	0.203	0.205	0.212	0.200	0.241	0.239	0.200	0.203	0.236	0.231
F	0.123	0.105	0.102	0.055	0.082	0.108	0.043	0.067	0.092	0.106	0.094	0.115
TiO ₂	0.303	0.372	0.771	0.889	0.710	0.511	1.642	1.518	0.782	0.723	1.185	0.816
Cl	0.004	0.000	0.004	0.000	0.000	0.000	0.000	0.000	0.000	0.001	0.003	0.000
CaO	0.262	0.012	0.026	0.023	0.029	0.011	0.000	0.006	0.009	0.012	0.038	0.019
Total	94.732	96.078	95.988	96.064	95.458	95.723	95.843	95.573	95.851	95.504	95.218	95.901
Cations pfu												
Si	3.16	3.21	3.17	3.23	3.22	3.16	3.11	3.12	3.16	3.18	3.12	3.18
Ti	0.02	0.02	0.04	0.04	0.04	0.03	0.08	0.08	0.04	0.04	0.06	0.04
Al	2.54	2.51	2.54	2.45	2.49	2.54	2.58	2.57	2.53	2.52	2.57	2.50
Fe	0.20	0.18	0.18	0.18	0.17	0.21	0.17	0.18	0.19	0.20	0.20	0.20
Mg	0.11	0.10	0.11	0.10	0.10	0.10	0.07	0.08	0.11	0.11	0.09	0.12
Mn	0.00	0.00	0.00	0.00	0.00	0.00	0.00	0.00	0.00	0.00	0.00	0.00
Ca	0.02	0.00	0.00	0.00	0.00	0.00	0.00	0.00	0.00	0.00	0.00	0.00
Na	0.03	0.03	0.03	0.03	0.03	0.03	0.03	0.03	0.03	0.03	0.03	0.03
K	0.99	0.97	0.98	0.93	0.93	0.98	0.97	0.96	0.97	0.96	0.95	0.96
F	0.03	0.02	0.02	0.01	0.02	0.02	0.01	0.01	0.02	0.02	0.02	0.02
Cl	0.00	0.00	0.00	0.00	0.00	0.00	0.00	0.00	0.00	0.00	0.00	0.00
Total positive cations	7.06	7.02	7.03	6.98	6.98	7.04	7.01	7.02	7.03	7.02	7.02	7.03

Type	Near myr	Near myr	Near myr	Near myr	Near myr	Near myr	Near myr	Near myr
SiO ₂	46.670	46.960	46.990	47.470	47.260	47.210	47.520	48.130
Al ₂ O ₃	31.640	31.780	31.200	31.130	31.880	31.360	32.380	31.800
MgO	1.149	0.998	1.236	1.376	1.082	1.131	0.999	0.988
K ₂ O	10.980	11.310	11.050	11.240	11.380	11.270	11.300	11.410
MnO	0.004	0.017	0.000	0.011	0.033	0.011	0.002	0.020
FeO	4.120	3.450	3.990	4.200	3.630	3.680	3.180	3.380
Na ₂ O	0.223	0.205	0.198	0.253	0.217	0.189	0.201	0.212
F	0.118	0.065	0.090	0.118	0.076	0.109	0.073	0.082
TiO ₂	0.792	0.910	0.643	0.708	0.657	0.809	0.449	0.732
Cl	0.004	0.002	0.008	0.006	0.000	0.006	0.007	0.003
CaO	0.024	0.032	0.017	0.044	0.038	0.028	0.031	0.009
Total	95.724	95.729	95.420	96.555	96.252	95.802	96.142	96.765
Cations pfu								
Si	3.15	3.16	3.18	3.18	3.17	3.18	3.18	3.20
Ti	0.04	0.05	0.03	0.04	0.03	0.04	0.02	0.04
Al	2.52	2.52	2.49	2.46	2.52	2.49	2.55	2.49
Fe	0.23	0.19	0.23	0.24	0.20	0.21	0.18	0.19
Mg	0.12	0.10	0.12	0.14	0.11	0.11	0.10	0.10
Mn	0.00	0.00	0.00	0.00	0.00	0.00	0.00	0.00
Ca	0.00	0.00	0.00	0.00	0.00	0.00	0.00	0.00
Na	0.03	0.03	0.03	0.03	0.03	0.02	0.03	0.03
K	0.95	0.97	0.95	0.96	0.97	0.97	0.96	0.97
F	0.03	0.01	0.02	0.02	0.02	0.02	0.02	0.02
Cl	0.00	0.00	0.00	0.00	0.00	0.00	0.00	0.00
Total positive cations	7.04	7.03	7.03	7.05	7.04	7.03	7.02	7.01

5.2 BIOTITE DATA

Type	As Musc	As Musc	As Musc	As Musc	As Musc	As Musc	As Musc	As Musc	As Musc	As Musc	As Musc	As Musc
SiO ₂	34.610	35.140	35.000	34.400	35.340	34.800	35.150	35.150	35.680	34.430	35.030	35.010
Al ₂ O ₃	16.340	16.350	16.730	16.880	17.050	16.600	17.050	16.510	16.730	16.960	16.690	16.220
MgO	7.540	7.390	7.290	7.660	7.150	7.270	7.090	7.420	6.810	7.120	7.030	7.390
K ₂ O	9.020	9.770	9.770	8.810	10.070	9.510	10.060	9.800	10.260	9.120	9.770	9.570
MnO	0.263	0.283	0.295	0.264	0.281	0.249	0.255	0.243	0.267	0.308	0.242	0.281
FeO	24.060	23.780	23.460	23.730	22.660	23.400	23.230	23.520	23.450	24.260	24.170	23.990
Na ₂ O	0.017	0.054	0.053	0.036	0.059	0.035	0.082	0.042	0.055	0.032	0.046	0.052
F	0.172	0.208	0.221	0.143	0.168	0.143	0.194	0.218	0.240	0.097	0.179	0.281
TiO ₂	2.450	2.160	2.320	2.160	2.430	2.490	2.500	2.390	2.880	1.375	2.570	2.320
Cl	0.023	0.035	0.040	0.030	0.041	0.037	0.037	0.033	0.035	0.043	0.036	0.035
CaO	0.017	0.026	0.000	0.034	0.012	0.013	0.006	0.010	0.001	0.065	0.008	0.071
Total	94.513	95.196	95.178	94.146	95.262	94.547	95.654	95.337	96.408	93.810	95.771	95.220
Cations pfu												
Si	2.74	2.76	2.75	2.72	2.76	2.75	2.74	2.76	2.77	2.74	2.74	2.76
Ti	0.15	0.13	0.14	0.13	0.14	0.15	0.15	0.14	0.17	0.08	0.15	0.14
Al	1.52	1.52	1.55	1.57	1.57	1.54	1.57	1.53	1.53	1.59	1.54	1.51
Fe	1.59	1.56	1.54	1.57	1.48	1.54	1.52	1.54	1.52	1.62	1.58	1.58
Mg	0.89	0.87	0.85	0.90	0.83	0.85	0.82	0.87	0.79	0.85	0.82	0.87
Mn	0.02	0.02	0.02	0.02	0.02	0.02	0.02	0.02	0.02	0.02	0.02	0.02
Ca	0.00	0.00	0.00	0.00	0.00	0.00	0.00	0.00	0.00	0.01	0.00	0.01
Na	0.00	0.01	0.01	0.01	0.01	0.01	0.01	0.01	0.01	0.00	0.01	0.01
K	0.91	0.98	0.98	0.89	1.00	0.96	1.00	0.98	1.01	0.93	0.97	0.96
F	0.04	0.05	0.05	0.04	0.04	0.04	0.05	0.05	0.06	0.02	0.04	0.07
Cl	0.00	0.00	0.01	0.00	0.01	0.00	0.00	0.00	0.00	0.01	0.00	0.00
Total positive cations	7.81	7.85	7.83	7.81	7.82	7.82	7.83	7.83	7.81	7.84	7.83	7.84

Type	As Musc	As Musc	As Musc	As Musc	As Musc	As Musc	As Musc	As Musc	As Musc	As Musc	As Musc	As Musc
SiO ₂	35.560	35.160	35.300	34.660	35.350	35.280	35.070	35.450	34.840	34.520	34.870	35.790
Al ₂ O ₃	16.320	16.680	16.300	15.960	16.550	16.550	16.480	16.630	16.240	16.780	16.670	16.700
MgO	7.170	6.660	7.140	7.260	7.150	7.380	7.480	7.340	7.740	7.660	6.900	8.050
K ₂ O	10.000	9.680	9.900	9.080	10.110	9.500	9.460	9.560	9.560	9.500	9.720	9.190
MnO	0.248	0.220	0.246	0.220	0.283	0.256	0.284	0.253	0.237	0.253	0.309	0.265
FeO	23.190	23.760	23.210	24.400	24.080	23.800	24.390	23.650	23.460	23.720	23.670	23.710
Na ₂ O	0.081	0.032	0.077	0.065	0.048	0.038	0.039	0.059	0.056	0.046	0.044	0.039
F	0.294	0.164	0.216	0.082	0.233	0.150	0.223	0.237	0.227	0.209	0.225	0.188
TiO ₂	2.700	2.930	2.590	2.290	2.350	2.570	2.190	2.500	2.310	1.880	2.880	1.650
Cl	0.041	0.031	0.032	0.039	0.040	0.037	0.041	0.038	0.045	0.034	0.042	0.046
CaO	0.015	0.001	0.069	0.058	0.013	0.011	0.015	0.018	0.016	0.052	0.000	0.012
Total	95.618	95.319	95.080	94.113	96.208	95.571	95.672	95.735	94.732	94.655	95.330	95.640
Cations pfu												
Si	2.78	2.75	2.77	2.76	2.76	2.75	2.75	2.76	2.75	2.73	2.74	2.78
Ti	0.16	0.17	0.15	0.14	0.14	0.15	0.13	0.15	0.14	0.11	0.17	0.10
Al	1.50	1.54	1.51	1.50	1.52	1.52	1.52	1.53	1.51	1.56	1.54	1.53
Fe	1.51	1.56	1.52	1.62	1.57	1.55	1.60	1.54	1.55	1.57	1.55	1.54
Mg	0.83	0.78	0.84	0.86	0.83	0.86	0.87	0.85	0.91	0.90	0.81	0.93
Mn	0.02	0.01	0.02	0.01	0.02	0.02	0.02	0.02	0.02	0.02	0.02	0.02
Ca	0.00	0.00	0.01	0.00	0.00	0.00	0.00	0.00	0.00	0.00	0.00	0.00
Na	0.01	0.00	0.01	0.01	0.01	0.01	0.01	0.01	0.01	0.01	0.01	0.01
K	1.00	0.97	0.99	0.92	1.01	0.95	0.95	0.95	0.96	0.96	0.97	0.91
F	0.07	0.04	0.05	0.02	0.06	0.04	0.06	0.06	0.06	0.05	0.06	0.05
Cl	0.01	0.00	0.00	0.01	0.01	0.00	0.01	0.01	0.01	0.00	0.01	0.01
Total positive cations	7.82	7.79	7.82	7.82	7.85	7.81	7.84	7.81	7.84	7.86	7.81	7.82

Type	As Musc	As Musc	As Musc	As Musc	As Musc	As Musc	As Musc	As Musc	As Musc	As Musc	As Musc	As Musc
SiO ₂	35.120	35.400	35.550	35.730	35.660	35.230	35.370	35.670	35.570	35.630	35.680	36.000
Al ₂ O ₃	16.670	16.810	16.660	16.740	16.710	16.170	16.800	16.270	16.770	16.770	16.870	16.720
MgO	7.060	7.050	7.200	7.020	7.170	7.430	6.920	6.850	7.080	6.960	6.950	7.460
K ₂ O	9.890	10.080	9.780	9.980	9.840	9.510	10.060	9.760	9.670	10.040	9.950	10.240
MnO	0.248	0.227	0.265	0.262	0.241	0.243	0.235	0.269	0.241	0.315	0.262	0.261
FeO	24.800	23.820	24.140	24.110	23.860	24.520	24.550	24.560	23.590	24.400	24.320	23.690
Na ₂ O	0.092	0.047	0.072	0.050	0.036	0.032	0.051	0.043	0.051	0.081	0.075	0.052
F	0.255	0.258	0.352	0.283	0.169	0.120	0.226	0.112	0.167	0.201	0.235	0.295
TiO ₂	2.600	2.620	2.510	2.820	2.670	2.440	2.640	3.000	2.630	2.860	3.040	2.180
Cl	0.052	0.041	0.038	0.038	0.036	0.039	0.033	0.038	0.040	0.030	0.035	0.036
CaO	0.025	0.004	0.028	0.007	0.014	0.020	0.009	0.004	0.012	0.000	0.008	0.001
Total	96.813	96.357	96.594	97.039	96.405	95.754	96.894	96.575	95.821	97.287	97.425	96.936
Cations pfu												
Si	2.73	2.75	2.76	2.76	2.76	2.76	2.74	2.77	2.77	2.75	2.74	2.78
Ti	0.15	0.15	0.15	0.16	0.16	0.14	0.15	0.17	0.15	0.17	0.18	0.13
Al	1.53	1.54	1.52	1.52	1.53	1.49	1.53	1.49	1.54	1.52	1.53	1.52
Fe	1.61	1.55	1.57	1.56	1.55	1.60	1.59	1.59	1.53	1.57	1.56	1.53
Mg	0.82	0.82	0.83	0.81	0.83	0.87	0.80	0.79	0.82	0.80	0.80	0.86
Mn	0.02	0.01	0.02	0.02	0.02	0.02	0.02	0.02	0.02	0.02	0.02	0.02
Ca	0.00	0.00	0.00	0.00	0.00	0.00	0.00	0.00	0.00	0.00	0.00	0.00
Na	0.01	0.01	0.01	0.01	0.01	0.00	0.01	0.01	0.01	0.01	0.01	0.01
K	0.98	1.00	0.97	0.98	0.97	0.95	0.99	0.97	0.96	0.99	0.98	1.01
F	0.06	0.06	0.09	0.07	0.04	0.03	0.06	0.03	0.04	0.05	0.06	0.07
Cl	0.01	0.01	0.00	0.00	0.00	0.01	0.00	0.00	0.01	0.00	0.00	0.00
Total positive cations	7.85	7.83	7.82	7.81	7.81	7.83	7.84	7.80	7.80	7.83	7.81	7.84

Type	Inside	Inside	Inside	Inside	Inside	Inside	Inside	Inside	Inside	Inside	Inside	Inside
SiO ₂	35.870	35.340	35.270	35.660	35.210	35.370	34.930	35.610	35.080	35.180	35.420	35.620
Al ₂ O ₃	16.990	16.340	16.570	17.400	17.070	16.350	17.130	16.910	17.180	17.250	16.980	16.640
MgO	6.770	7.230	6.520	7.410	6.590	6.290	7.170	7.480	7.080	7.100	7.170	7.080
K ₂ O	9.880	9.620	10.050	9.850	9.870	9.950	9.930	9.830	10.150	9.930	9.930	10.000
MnO	0.231	0.204	0.306	0.280	0.315	0.295	0.314	0.280	0.324	0.284	0.279	0.295
FeO	23.280	23.290	24.810	22.420	24.170	24.770	23.420	24.210	23.350	23.870	24.200	23.780
Na ₂ O	0.095	0.074	0.047	0.097	0.085	0.039	0.067	0.040	0.083	0.079	0.091	0.098
F	0.207	0.171	0.297	0.264	0.219	0.277	0.248	0.265	0.251	0.312	0.284	0.225
TiO ₂	3.390	2.770	3.060	2.370	2.900	4.080	2.170	1.920	2.230	2.570	2.250	2.490
Cl	0.036	0.045	0.037	0.047	0.034	0.029	0.048	0.044	0.037	0.035	0.046	0.033
CaO	0.061	0.052	0.025	0.034	0.040	0.023	0.036	0.036	0.013	0.016	0.007	0.040
Total	96.430	95.135	96.992	95.832	96.503	97.473	95.463	96.626	95.778	96.626	96.656	96.301
Cations pfu												
Si	2.76	2.77	2.74	2.76	2.73	2.73	2.74	2.76	2.74	2.73	2.75	2.77
Ti	0.20	0.16	0.18	0.14	0.17	0.24	0.13	0.11	0.13	0.15	0.13	0.15
Al	1.54	1.51	1.52	1.59	1.56	1.49	1.58	1.54	1.58	1.58	1.55	1.52
Fe	1.50	1.53	1.61	1.45	1.57	1.60	1.53	1.57	1.53	1.55	1.57	1.54
Mg	0.78	0.84	0.75	0.85	0.76	0.72	0.84	0.86	0.82	0.82	0.83	0.82
Mn	0.02	0.01	0.02	0.02	0.02	0.02	0.02	0.02	0.02	0.02	0.02	0.02
Ca	0.01	0.00	0.00	0.00	0.00	0.00	0.00	0.00	0.00	0.00	0.00	0.00
Na	0.01	0.01	0.01	0.01	0.01	0.01	0.01	0.01	0.01	0.01	0.01	0.01
K	0.97	0.96	1.00	0.97	0.98	0.98	0.99	0.97	1.01	0.98	0.98	0.99
F	0.05	0.04	0.07	0.06	0.05	0.07	0.06	0.06	0.06	0.08	0.07	0.06
Cl	0.00	0.01	0.00	0.01	0.00	0.00	0.01	0.01	0.00	0.00	0.01	0.00
Total positive cations	7.77	7.80	7.83	7.80	7.81	7.78	7.85	7.85	7.85	7.83	7.84	7.83

Type	Inside	Inside	Inside	Inside	Inside	Inside	Inside	Inside	Inside	Inside	Inside	Inside
SiO ₂	35.570	35.160	35.410	35.430	35.350	35.480	35.200	35.620	35.820	35.320	35.710	35.770
Al ₂ O ₃	17.250	17.060	17.650	16.730	16.780	16.500	16.800	16.620	16.910	17.050	17.000	17.190
MgO	6.720	7.060	6.370	6.820	6.870	6.620	7.030	6.830	7.270	7.210	7.350	7.330
K ₂ O	10.250	10.040	9.900	9.800	10.210	10.190	10.080	9.970	9.980	9.860	10.140	10.260
MnO	0.275	0.327	0.290	0.290	0.277	0.327	0.299	0.278	0.290	0.323	0.298	0.297
FeO	23.130	23.770	24.000	24.630	23.700	23.530	22.970	23.790	23.690	23.240	23.120	21.970
Na ₂ O	0.058	0.071	0.067	0.071	0.062	0.049	0.065	0.053	0.044	0.049	0.066	0.090
F	0.190	0.230	0.193	0.234	0.223	0.202	0.247	0.290	0.251	0.290	0.321	0.269
TiO ₂	2.710	2.370	2.720	2.080	2.750	3.340	2.450	3.010	2.470	2.460	2.410	2.430
Cl	0.035	0.041	0.041	0.043	0.036	0.039	0.035	0.037	0.040	0.033	0.035	0.039
CaO	0.029	0.010	0.014	0.013	0.006	0.045	0.055	0.024	0.000	0.699	0.000	0.007
Total	96.216	96.139	96.655	96.141	96.264	96.322	95.232	96.520	96.765	96.533	96.450	95.651
Cations pfu												
Si	2.76	2.74	2.74	2.77	2.75	2.76	2.76	2.76	2.76	2.74	2.76	2.78
Ti	0.16	0.14	0.16	0.12	0.16	0.20	0.14	0.18	0.14	0.14	0.14	0.14
Al	1.58	1.57	1.61	1.54	1.54	1.51	1.55	1.52	1.54	1.56	1.55	1.57
Fe	1.50	1.55	1.55	1.61	1.54	1.53	1.51	1.54	1.53	1.51	1.50	1.43
Mg	0.78	0.82	0.73	0.79	0.80	0.77	0.82	0.79	0.84	0.83	0.85	0.85
Mn	0.02	0.02	0.02	0.02	0.02	0.02	0.02	0.02	0.02	0.02	0.02	0.02
Ca	0.00	0.00	0.00	0.00	0.00	0.00	0.00	0.00	0.00	0.06	0.00	0.00
Na	0.01	0.01	0.01	0.01	0.01	0.01	0.01	0.01	0.01	0.01	0.01	0.01
K	1.01	1.00	0.98	0.98	1.01	1.01	1.01	0.99	0.98	0.97	1.00	1.02
F	0.05	0.06	0.05	0.06	0.05	0.05	0.06	0.07	0.06	0.07	0.08	0.07
Cl	0.00	0.01	0.01	0.01	0.00	0.01	0.00	0.00	0.01	0.00	0.00	0.01
Total positive cations	7.81	7.84	7.79	7.84	7.83	7.80	7.83	7.80	7.82	7.83	7.83	7.81

Type	Inside	Inside	Inside	Inside	Inside	Inside	Inside	Inside	Inside	Inside	Inside	Inside
SiO ₂	35.340	35.130	35.770	35.450	35.550	35.430	35.450	35.380	35.620	35.070	35.620	35.380
Al ₂ O ₃	16.990	16.920	16.750	16.800	17.360	16.100	17.200	17.080	16.950	16.780	16.930	16.480
MgO	6.850	6.990	6.780	6.770	7.880	6.100	6.970	6.830	6.920	6.820	6.600	6.740
K ₂ O	10.010	9.520	9.960	10.000	9.690	9.960	10.060	10.140	9.810	10.080	10.030	10.020
MnO	0.268	0.292	0.291	0.304	0.268	0.277	0.280	0.327	0.292	0.297	0.298	0.307
FeO	23.900	23.850	23.350	23.960	23.030	23.940	22.760	23.590	24.250	23.940	24.170	23.260
Na ₂ O	0.071	0.076	0.063	0.060	0.052	0.078	0.060	0.088	0.073	0.064	0.062	0.073
F	0.241	0.166	0.219	0.263	0.254	0.102	0.260	0.273	0.214	0.243	0.150	0.223
TiO ₂	2.770	2.850	3.220	2.970	1.452	4.580	2.970	2.690	2.800	2.600	3.350	3.060
Cl	0.036	0.031	0.039	0.035	0.038	0.038	0.027	0.036	0.043	0.039	0.033	0.035
CaO	0.041	0.192	0.031	0.022	0.043	0.037	0.021	0.009	0.043	0.006	0.037	0.074
Total	96.518	96.016	96.472	96.633	95.618	96.641	96.059	96.442	97.014	95.939	97.280	95.653
Cations pfu												
Si	2.74	2.73	2.76	2.75	2.76	2.74	2.75	2.75	2.75	2.74	2.74	2.76
Ti	0.16	0.17	0.19	0.17	0.08	0.27	0.17	0.16	0.16	0.15	0.19	0.18
Al	1.55	1.55	1.53	1.53	1.59	1.47	1.57	1.56	1.54	1.55	1.53	1.52
Fe	1.55	1.55	1.51	1.55	1.50	1.55	1.47	1.53	1.56	1.57	1.55	1.52
Mg	0.79	0.81	0.78	0.78	0.91	0.70	0.81	0.79	0.80	0.79	0.76	0.78
Mn	0.02	0.02	0.02	0.02	0.02	0.02	0.02	0.02	0.02	0.02	0.02	0.02
Ca	0.00	0.02	0.00	0.00	0.00	0.00	0.00	0.00	0.00	0.00	0.00	0.01
Na	0.01	0.01	0.01	0.01	0.01	0.01	0.01	0.01	0.01	0.01	0.01	0.01
K	0.99	0.94	0.98	0.99	0.96	0.98	0.99	1.00	0.97	1.01	0.98	1.00
F	0.06	0.04	0.05	0.06	0.06	0.02	0.06	0.07	0.05	0.06	0.04	0.06
Cl	0.00	0.00	0.01	0.00	0.00	0.00	0.00	0.00	0.01	0.01	0.00	0.00
Total positive cations	7.82	7.80	7.78	7.81	7.84	7.75	7.80	7.82	7.81	7.84	7.80	7.80

Type	Inside	Inside	Str Shad	Str Shad	Str Shad	Str Shad	Str Shad	Str Shad	Str Shad	Str Shad	Str Shad	Str Shad
SiO ₂	35.430	35.490	34.770	35.680	35.220	35.550	34.860	35.610	35.210	35.080	35.240	35.740
Al ₂ O ₃	17.270	17.060	16.750	17.110	16.420	16.810	16.610	16.880	16.680	16.600	16.600	16.440
MgO	7.030	7.010	7.650	7.200	6.680	7.260	6.980	7.220	6.990	7.120	6.680	7.400
K ₂ O	10.060	10.050	9.060	10.140	9.770	9.890	9.360	9.770	9.940	9.630	10.070	9.670
MnO	0.303	0.275	0.231	0.308	0.296	0.228	0.223	0.249	0.278	0.268	0.333	0.208
FeO	24.690	24.470	24.370	23.150	24.210	23.630	23.550	23.560	23.120	23.860	23.700	23.900
Na ₂ O	0.064	0.085	0.036	0.040	0.050	0.046	0.052	0.043	0.053	0.038	0.060	0.035
F	0.214	0.235	0.155	0.250	0.229	0.246	0.106	0.217	0.208	0.168	0.163	0.205
TiO ₂	2.560	2.420	2.230	2.260	3.170	2.390	2.700	2.490	2.590	2.730	2.920	2.480
Cl	0.040	0.043	0.037	0.034	0.033	0.043	0.035	0.030	0.036	0.029	0.030	0.030
CaO	0.014	0.031	0.008	0.020	0.010	0.039	0.036	0.008	0.024	0.036	0.014	0.041
Total	97.674	97.168	95.296	96.191	96.087	96.133	94.512	96.076	95.130	95.560	95.811	96.148
Cations pfu												
Si	2.72	2.74	2.73	2.77	2.75	2.76	2.75	2.76	2.76	2.74	2.75	2.77
Ti	0.15	0.14	0.13	0.13	0.19	0.14	0.16	0.15	0.15	0.16	0.17	0.14
Al	1.56	1.55	1.55	1.56	1.51	1.54	1.54	1.54	1.54	1.53	1.53	1.50
Fe	1.59	1.58	1.60	1.50	1.58	1.54	1.55	1.53	1.52	1.56	1.55	1.55
Mg	0.81	0.81	0.89	0.83	0.78	0.84	0.82	0.83	0.82	0.83	0.78	0.86
Mn	0.02	0.02	0.02	0.02	0.02	0.01	0.01	0.02	0.02	0.02	0.02	0.01
Ca	0.00	0.00	0.00	0.00	0.00	0.00	0.00	0.00	0.00	0.00	0.00	0.00
Na	0.01	0.01	0.01	0.01	0.01	0.01	0.01	0.01	0.01	0.01	0.01	0.01
K	0.99	0.99	0.91	1.00	0.97	0.98	0.94	0.97	0.99	0.96	1.00	0.96
F	0.05	0.06	0.04	0.06	0.06	0.06	0.03	0.05	0.05	0.04	0.04	0.05
Cl	0.01	0.01	0.00	0.00	0.00	0.01	0.00	0.00	0.00	0.00	0.00	0.00
Total positive cations	7.84	7.84	7.82	7.82	7.80	7.82	7.79	7.81	7.82	7.81	7.82	7.81

Type	Str Shad	Str Shad	Str Shad	Str Shad	Str Shad	Str Shad	Str Shad	Str Shad	Str Shad	Str Shad	Str Shad	Str Shad
SiO ₂	35.350	36.040	35.690	35.570	35.380	35.500	35.590	35.870	35.670	35.620	35.460	35.380
Al ₂ O ₃	16.750	17.330	16.610	16.760	16.830	16.440	16.840	16.850	16.860	16.780	16.820	16.670
MgO	6.700	7.740	7.210	7.280	7.000	7.190	7.310	7.310	7.280	6.870	7.100	7.440
K ₂ O	10.130	10.010	10.120	9.780	10.150	9.770	9.800	9.960	9.890	10.130	10.050	9.990
MnO	0.328	0.252	0.255	0.239	0.265	0.255	0.233	0.259	0.285	0.273	0.343	0.312
FeO	23.500	23.100	23.700	23.650	23.150	24.010	23.490	23.860	23.410	23.060	23.430	22.980
Na ₂ O	0.046	0.070	0.060	0.051	0.045	0.091	0.036	0.074	0.063	0.046	0.044	0.032
F	0.181	0.240	0.269	0.261	0.270	0.286	0.185	0.250	0.558	0.266	0.217	0.171
TiO ₂	2.800	1.561	2.590	2.430	2.600	2.430	2.530	2.600	1.820	2.840	2.550	2.080
Cl	0.033	0.043	0.038	0.037	0.039	0.055	0.034	0.038	0.046	0.043	0.034	0.040
CaO	0.011	0.027	0.017	0.016	0.020	0.042	0.015	0.005	0.577	0.000	0.003	0.000
Total	95.828	96.413	96.559	96.074	95.749	96.067	96.063	97.075	96.459	95.929	96.051	95.095
Cations pfu												
Si	2.76	2.78	2.77	2.76	2.76	2.77	2.76	2.76	2.77	2.77	2.76	2.77
Ti	0.16	0.09	0.15	0.14	0.15	0.14	0.15	0.15	0.11	0.17	0.15	0.12
Al	1.54	1.58	1.52	1.54	1.55	1.51	1.54	1.53	1.54	1.54	1.54	1.54
Fe	1.53	1.49	1.54	1.54	1.51	1.57	1.52	1.54	1.52	1.50	1.52	1.51
Mg	0.78	0.89	0.83	0.84	0.81	0.84	0.85	0.84	0.84	0.80	0.82	0.87
Mn	0.02	0.02	0.02	0.02	0.02	0.02	0.02	0.02	0.02	0.02	0.02	0.02
Ca	0.00	0.00	0.00	0.00	0.00	0.00	0.00	0.00	0.05	0.00	0.00	0.00
Na	0.01	0.01	0.01	0.01	0.01	0.01	0.01	0.01	0.01	0.01	0.01	0.00
K	1.01	0.98	1.00	0.97	1.01	0.97	0.97	0.98	0.98	1.00	1.00	1.00
F	0.04	0.06	0.07	0.06	0.07	0.07	0.05	0.06	0.14	0.07	0.05	0.04
Cl	0.00	0.01	0.01	0.00	0.01	0.01	0.00	0.00	0.01	0.01	0.00	0.01
Total positive cations	7.81	7.84	7.83	7.82	7.82	7.83	7.81	7.82	7.84	7.80	7.82	7.84

Type	Str Shad	Str Shad	Str Shad	Str Shad	Str Shad	Str Shad	Str Shad	Str Shad	Str Shad
SiO ₂	35.740	35.400	35.520	35.160	35.100	35.370	35.070	34.990	35.600
Al ₂ O ₃	16.810	16.820	16.530	17.090	16.720	17.180	17.140	16.570	16.880
MgO	7.650	7.030	7.240	7.580	6.870	7.380	7.030	7.510	6.930
K ₂ O	10.180	10.260	10.010	9.520	9.890	10.120	10.180	9.050	10.150
MnO	0.266	0.248	0.255	0.332	0.298	0.250	0.303	0.241	0.302
FeO	22.970	23.240	23.090	23.330	23.500	22.910	22.780	24.290	22.660
Na ₂ O	0.046	0.065	0.030	0.047	0.063	0.068	0.083	0.061	0.053
F	0.251	0.230	0.241	0.243	0.173	0.259	0.258	0.179	0.244
TiO ₂	2.140	2.440	2.730	2.010	3.050	1.720	2.370	2.630	2.640
Cl	0.032	0.040	0.032	0.041	0.040	0.053	0.034	0.026	0.036
CaO	0.000	0.023	0.000	0.017	0.019	0.005	0.022	0.045	0.019
Total	96.085	95.796	95.677	95.369	95.723	95.314	95.269	95.593	95.514
Cations pfu									
Si	2.77	2.76	2.77	2.75	2.74	2.77	2.75	2.73	2.78
Ti	0.12	0.14	0.16	0.12	0.18	0.10	0.14	0.15	0.15
Al	1.54	1.55	1.52	1.57	1.54	1.58	1.58	1.53	1.55
Fe	1.49	1.52	1.51	1.52	1.53	1.50	1.49	1.59	1.48
Mg	0.88	0.82	0.84	0.88	0.80	0.86	0.82	0.87	0.81
Mn	0.02	0.02	0.02	0.02	0.02	0.02	0.02	0.02	0.02
Ca	0.00	0.00	0.00	0.00	0.00	0.00	0.00	0.00	0.00
Na	0.01	0.01	0.00	0.01	0.01	0.01	0.01	0.01	0.01
K	1.01	1.02	1.00	0.95	0.99	1.01	1.02	0.90	1.01
F	0.06	0.06	0.06	0.06	0.04	0.06	0.06	0.04	0.06
Cl	0.00	0.01	0.00	0.01	0.01	0.01	0.00	0.00	0.00
Total positive cations	7.84	7.84	7.81	7.83	7.81	7.85	7.84	7.81	7.80

5.3 FELDSPAR DATA

Type	ksp core	ksp nm	recrys myr	recrys myr	ksp nm	ksp core	ksp core	ksp nm	str myr	str myr	str myr	str myr	ksp nm	ksp nm
SiO ₂	64.560	64.420	61.690	62.050	64.420	64.380	64.170	64.440	62.250	64.490	61.990	71.710	63.930	63.790
Al ₂ O ₃	18.780	18.750	23.960	23.760	18.730	18.800	18.710	18.730	23.670	22.560	23.740	17.350	18.750	18.750
MgO	0.000	0.000	0.001	0.000	0.000	0.000	0.002	0.000	0.000	0.000	0.000	0.001	0.000	0.000
CaO	0.025	0.012	5.340	5.110	0.017	0.037	0.033	0.042	4.970	4.820	5.170	3.710	0.011	0.011
FeO	0.021	0.029	0.028	0.014	0.003	0.004	0.010	0.028	0.033	0.007	0.028	0.036	0.007	0.009
Na ₂ O	0.748	0.699	8.360	8.400	0.702	0.783	0.776	0.746	8.500	8.060	8.370	6.200	0.709	0.672
SrO	0.145	0.097	0.096	0.118	0.145	0.118	0.123	0.122	0.120	0.123	0.091	0.095	0.099	0.131
K ₂ O	15.790	15.830	0.131	0.080	16.000	15.870	15.820	15.910	0.136	0.146	0.107	0.292	15.840	15.880
BaO	0.371	0.484	0.045	0.000	0.416	0.297	0.411	0.338	0.031	0.021	0.002	0.000	0.476	0.599
Total	100.439	100.321	99.650	99.532	100.432	100.288	100.056	100.357	99.709	100.227	99.497	99.393	99.821	99.843
Cations pfu														
Si	2.98	2.98	2.75	2.76	2.98	2.98	2.98	2.98	2.77	2.83	2.76	3.11	2.97	2.97
Al	1.02	1.02	1.26	1.25	1.02	1.02	1.02	1.02	1.24	1.17	1.25	0.89	1.03	1.03
Mg	0.00	0.00	0.00	0.00	0.00	0.00	0.00	0.00	0.00	0.00	0.00	0.00	0.00	0.00
Ca	0.00	0.00	0.25	0.24	0.00	0.00	0.00	0.00	0.24	0.23	0.25	0.17	0.00	0.00
Fe	0.00	0.00	0.00	0.00	0.00	0.00	0.00	0.00	0.00	0.00	0.00	0.00	0.00	0.00
Na	0.07	0.06	0.72	0.72	0.06	0.07	0.07	0.07	0.73	0.69	0.72	0.52	0.06	0.06
Sr	0.00	0.00	0.00	0.00	0.00	0.00	0.00	0.00	0.00	0.00	0.00	0.00	0.00	0.00
K	0.93	0.93	0.01	0.00	0.94	0.94	0.94	0.94	0.01	0.01	0.01	0.02	0.94	0.94
Ba	0.01	0.01	0.00	0.00	0.01	0.01	0.01	0.01	0.00	0.00	0.00	0.00	0.01	0.01
Total	5.01	5.01	4.99	4.98	5.02	5.02	5.02	5.01	4.99	4.93	4.98	4.71	5.02	5.02
End member composition														
An	0.1	0.1	25.9	25.0	0.1	0.2	0.2	0.2	24.2	24.6	25.3	24.3	0.1	0.1
Ab	6.7	6.3	73.4	74.5	6.2	7.0	6.9	6.6	75.0	74.5	74.1	73.4	6.4	6.0
Or	93.2	93.7	0.8	0.5	93.7	92.9	92.9	93.2	0.8	0.9	0.6	2.3	93.6	93.9

Type	ksp recrys	plag matrix	plag matrix	plag matrix	ksp recrys	plag matrix	plag core	plag core	plag core	plag core	plag core	plag core	plag core	plag core
SiO ₂	63.880	62.410	61.760	62.190	64.080	61.580	60.570	60.630	60.630	60.400	60.810	60.530	60.580	60.720
Al ₂ O ₃	18.640	23.480	23.630	23.420	18.660	23.770	24.700	24.630	24.620	24.720	24.510	24.550	24.520	24.550
MgO	0.003	0.000	0.002	0.001	0.000	0.000	0.000	0.000	0.003	0.000	0.000	0.004	0.003	0.007
CaO	0.024	4.960	5.040	4.970	0.015	5.420	6.220	6.220	6.170	6.230	6.080	6.100	6.150	6.080
FeO	0.061	0.059	0.062	0.075	0.051	0.072	0.033	0.028	0.042	0.095	0.031	0.010	0.000	0.031
Na ₂ O	0.446	8.500	8.440	8.490	0.446	8.320	7.980	7.970	7.970	8.030	7.990	7.990	8.060	8.030
SrO	0.094	0.101	0.117	0.103	0.080	0.074	0.082	0.108	0.109	0.095	0.100	0.096	0.097	0.103
K ₂ O	16.190	0.123	0.185	0.111	16.330	0.163	0.212	0.180	0.185	0.155	0.201	0.217	0.186	0.169
BaO	0.470	0.002	0.015	0.000	0.458	0.000	0.017	0.026	0.035	0.000	0.026	0.078	0.028	0.022
Total	99.808	99.634	99.251	99.361	100.120	99.399	99.815	99.792	99.764	99.724	99.749	99.574	99.625	99.712
Cations pfu														
Si	2.97	2.77	2.76	2.77	2.98	2.75	2.70	2.70	2.70	2.70	2.71	2.71	2.71	2.71
Al	1.02	1.23	1.24	1.23	1.02	1.25	1.30	1.29	1.29	1.30	1.29	1.29	1.29	1.29
Mg	0.00	0.00	0.00	0.00	0.00	0.00	0.00	0.00	0.00	0.00	0.00	0.00	0.00	0.00
Ca	0.00	0.24	0.24	0.24	0.00	0.26	0.30	0.30	0.29	0.30	0.29	0.29	0.29	0.29
Fe	0.00	0.00	0.00	0.00	0.00	0.00	0.00	0.00	0.00	0.00	0.00	0.00	0.00	0.00
Na	0.04	0.73	0.73	0.73	0.04	0.72	0.69	0.69	0.69	0.70	0.69	0.69	0.70	0.69
Sr	0.00	0.00	0.00	0.00	0.00	0.00	0.00	0.00	0.00	0.00	0.00	0.00	0.00	0.00
K	0.96	0.01	0.01	0.01	0.97	0.01	0.01	0.01	0.01	0.01	0.01	0.01	0.01	0.01
Ba	0.01	0.00	0.00	0.00	0.01	0.00	0.00	0.00	0.00	0.00	0.00	0.00	0.00	0.00
Total	5.01	4.98	4.99	4.98	5.02	4.99	5.00	5.00	5.00	5.01	5.00	5.00	5.00	5.00
End member composition														
An	0.1	24.2	24.5	24.3	0.1	26.2	29.7	29.8	29.6	29.7	29.3	29.3	29.3	29.2
Ab	4.0	75.1	74.4	75.1	4.0	72.8	69.0	69.1	69.3	69.4	69.6	69.5	69.6	69.8
Or	95.9	0.7	1.1	0.6	95.9	0.9	1.2	1.0	1.1	0.9	1.2	1.2	1.1	1.0

Type	ksp recrys	ksp recrys	ksp recrys	ksp core	ksp core	ksp core	ksp core	ksp core	plag core	plag core	plag core	plag core	ksp inside	ksp recrys
SiO ₂	64.280	63.870	64.010	64.470	64.360	64.310	64.330	64.300	62.260	60.570	60.600	60.470	64.610	64.230
Al ₂ O ₃	18.570	18.560	18.620	18.660	18.720	18.720	18.730	18.720	23.500	24.630	24.680	24.600	18.650	18.630
MgO	0.000	0.000	0.000	0.000	0.000	0.000	0.004	0.004	0.000	0.000	0.005	0.000	0.002	0.003
CaO	0.006	0.013	0.076	0.050	0.049	0.055	0.057	0.048	4.910	6.220	6.250	6.220	0.033	0.014
FeO	0.024	0.159	0.023	0.006	0.000	0.004	0.000	0.044	0.032	0.030	0.015	0.045	0.000	0.027
Na ₂ O	0.635	0.670	0.684	0.864	0.881	0.870	0.822	0.779	8.730	7.960	7.980	8.020	0.471	0.628
SrO	0.079	0.089	0.104	0.104	0.129	0.106	0.100	0.127	0.142	0.110	0.104	0.102	0.085	0.123
K ₂ O	15.440	15.260	15.320	15.120	15.080	15.070	15.140	15.220	0.142	0.166	0.198	0.194	16.470	16.050
BaO	0.273	0.411	0.634	0.372	0.387	0.269	0.367	0.297	0.000	0.000	0.030	0.007	0.269	0.415
Total	99.306	99.031	99.471	99.646	99.606	99.404	99.550	99.539	99.716	99.686	99.861	99.658	100.590	100.120
Cations pfu														
Si	2.99	2.98	2.98	2.99	2.98	2.98	2.98	2.98	2.77	2.70	2.70	2.70	2.98	2.98
Al	1.02	1.02	1.02	1.02	1.02	1.02	1.02	1.02	1.23	1.30	1.30	1.30	1.01	1.02
Mg	0.00	0.00	0.00	0.00	0.00	0.00	0.00	0.00	0.00	0.00	0.00	0.00	0.00	0.00
Ca	0.00	0.00	0.00	0.00	0.00	0.00	0.00	0.00	0.23	0.30	0.30	0.30	0.00	0.00
Fe	0.00	0.01	0.00	0.00	0.00	0.00	0.00	0.00	0.00	0.00	0.00	0.00	0.00	0.00
Na	0.06	0.06	0.06	0.08	0.08	0.08	0.07	0.07	0.75	0.69	0.69	0.69	0.04	0.06
Sr	0.00	0.00	0.00	0.00	0.00	0.00	0.00	0.00	0.00	0.00	0.00	0.00	0.00	0.00
K	0.92	0.91	0.91	0.89	0.89	0.89	0.90	0.90	0.01	0.01	0.01	0.01	0.97	0.95
Ba	0.00	0.01	0.01	0.01	0.01	0.00	0.01	0.01	0.00	0.00	0.00	0.00	0.00	0.01
Total	4.99	4.99	4.99	4.99	4.99	4.99	4.99	4.99	5.00	5.00	5.00	5.00	5.02	5.02
End member composition														
An	0.0	0.1	0.4	0.3	0.3	0.3	0.3	0.2	23.5	29.9	29.9	29.7	0.2	0.1
Ab	5.9	6.2	6.3	8.0	8.1	8.0	7.6	7.2	75.7	69.2	69.0	69.2	4.2	5.6
Or	94.1	93.7	93.3	91.8	91.6	91.7	92.1	92.6	0.8	1.0	1.1	1.1	95.7	94.3

Type	ksp recrys	ksp recrys	ksp recrys	plag core	plag core	str myr	ksp nm	str myr	str myr	str myr	str myr	str myr	ksp nm	ksp nm
SiO ₂	64.300	64.110	64.310	60.640	60.660	62.020	64.250	61.310	61.680	62.060	61.550	71.160	63.990	64.240
Al ₂ O ₃	18.590	18.700	18.600	24.490	24.480	23.790	18.670	24.110	23.830	23.600	23.920	18.810	18.630	18.580
MgO	0.000	0.000	0.002	0.000	0.000	0.000	0.000	0.003	0.008	0.000	0.002	0.000	0.002	0.001
CaO	0.013	0.000	0.003	5.950	5.980	4.960	0.050	5.410	5.290	4.790	5.250	3.660	0.028	0.065
FeO	0.030	0.246	0.189	0.040	0.043	0.029	0.025	0.020	0.014	0.000	0.011	0.011	0.003	0.000
Na ₂ O	0.671	0.445	0.675	7.830	7.800	8.430	0.674	8.200	8.210	8.620	8.320	6.900	0.678	0.688
SrO	0.085	0.108	0.109	0.099	0.114	0.091	0.156	0.088	0.103	0.110	0.102	0.086	0.086	0.125
K ₂ O	15.970	16.350	16.120	0.210	0.230	0.131	15.910	0.108	0.141	0.131	0.106	0.130	15.910	15.940
BaO	0.409	0.385	0.291	0.018	0.022	0.000	0.395	0.025	0.000	0.014	0.000	0.033	0.439	0.412
Total	100.069	100.345	100.298	99.278	99.329	99.450	100.129	99.274	99.276	99.325	99.262	100.791	99.766	100.051
Cations pfu														
Si	2.98	2.97	2.98	2.71	2.71	2.76	2.98	2.74	2.75	2.77	2.75	3.06	2.98	2.98
Al	1.02	1.02	1.01	1.29	1.29	1.25	1.02	1.27	1.25	1.24	1.26	0.95	1.02	1.02
Mg	0.00	0.00	0.00	0.00	0.00	0.00	0.00	0.00	0.00	0.00	0.00	0.00	0.00	0.00
Ca	0.00	0.00	0.00	0.29	0.29	0.24	0.00	0.26	0.25	0.23	0.25	0.17	0.00	0.00
Fe	0.00	0.01	0.01	0.00	0.00	0.00	0.00	0.00	0.00	0.00	0.00	0.00	0.00	0.00
Na	0.06	0.04	0.06	0.68	0.68	0.73	0.06	0.71	0.71	0.74	0.72	0.57	0.06	0.06
Sr	0.00	0.00	0.00	0.00	0.00	0.00	0.00	0.00	0.00	0.00	0.00	0.00	0.00	0.00
K	0.94	0.97	0.95	0.01	0.01	0.01	0.94	0.01	0.01	0.01	0.01	0.01	0.94	0.94
Ba	0.01	0.01	0.01	0.00	0.00	0.00	0.01	0.00	0.00	0.00	0.00	0.00	0.01	0.01
Total	5.01	5.02	5.02	4.99	4.99	4.98	5.01	4.99	4.98	4.99	4.99	4.76	5.02	5.01
End member composition														
An	0.1	0.0	0.0	29.2	29.4	24.3	0.2	26.5	26.0	23.3	25.7	22.5	0.1	0.3
Ab	6.0	4.0	6.0	69.6	69.3	74.9	6.0	72.8	73.1	75.9	73.7	76.6	6.1	6.1
Or	93.9	96.0	94.0	1.2	1.3	0.8	93.7	0.6	0.8	0.8	0.6	1.0	93.8	93.5

Type			plag											
	ksp nm	str myr	core	str myr	str myr	ksp nm	ksp core	ksp core	ksp core	str myr	ksp nm	str myr	str myr	ksp nm
SiO ₂	63.910	62.010	60.260	62.280	68.760	64.010	64.180	64.260	64.210	64.820	64.240	65.860	62.210	64.640
Al ₂ O ₃	18.600	23.480	24.610	23.450	20.040	18.630	18.670	18.680	18.830	22.510	18.730	22.240	23.630	18.720
MgO	0.000	0.002	0.000	0.000	0.000	0.001	0.000	0.000	0.000	0.000	0.000	0.000	0.000	0.001
CaO	0.052	4.840	6.130	4.650	4.190	0.080	0.069	0.067	0.056	4.590	0.012	4.990	5.070	0.064
FeO	0.032	0.015	0.010	0.006	0.000	0.024	0.012	0.000	0.010	0.019	0.000	0.022	0.026	0.014
Na ₂ O	0.733	8.430	7.600	8.520	7.630	0.599	0.685	0.689	0.786	8.160	0.725	7.870	8.740	0.716
SrO	0.137	0.098	0.097	0.089	0.096	0.113	0.122	0.104	0.133	0.117	0.111	0.123	0.116	0.133
K ₂ O	15.810	0.122	0.193	0.106	0.080	15.510	15.220	15.280	15.210	0.769	15.330	0.106	0.090	15.210
BaO	0.309	0.043	0.000	0.000	0.026	0.428	0.298	0.419	0.259	0.034	0.524	0.000	0.012	0.377
Total	99.582	99.039	98.899	99.101	100.822	99.394	99.256	99.499	99.495	101.019	99.671	101.211	99.893	99.875
Cations pfu														
Si	2.98	2.77	2.71	2.78	2.97	2.98	2.99	2.98	2.98	2.84	2.98	2.86	2.76	2.99
Al	1.02	1.24	1.30	1.23	1.02	1.02	1.02	1.02	1.03	1.16	1.02	1.14	1.24	1.02
Mg	0.00	0.00	0.00	0.00	0.00	0.00	0.00	0.00	0.00	0.00	0.00	0.00	0.00	0.00
Ca	0.00	0.23	0.29	0.22	0.19	0.00	0.00	0.00	0.00	0.22	0.00	0.23	0.24	0.00
Fe	0.00	0.00	0.00	0.00	0.00	0.00	0.00	0.00	0.00	0.00	0.00	0.00	0.00	0.00
Na	0.07	0.73	0.66	0.74	0.64	0.05	0.06	0.06	0.07	0.69	0.07	0.66	0.75	0.06
Sr	0.00	0.00	0.00	0.00	0.00	0.00	0.00	0.00	0.00	0.00	0.00	0.00	0.00	0.00
K	0.94	0.01	0.01	0.01	0.00	0.92	0.90	0.91	0.90	0.04	0.91	0.01	0.01	0.90
Ba	0.01	0.00	0.00	0.00	0.00	0.01	0.01	0.01	0.00	0.00	0.01	0.00	0.00	0.01
Total	5.02	4.98	4.98	4.98	4.84	5.00	4.99	4.99	4.99	4.95	4.99	4.90	5.00	4.98
End member composition														
An	0.3	23.9	30.5	23.0	23.2	0.4	0.4	0.3	0.3	22.6	0.1	25.8	24.2	0.3
Ab	6.6	75.4	68.4	76.3	76.3	5.5	6.4	6.4	7.3	72.8	6.7	73.6	75.3	6.7
Or	93.2	0.7	1.1	0.6	0.5	94.1	93.3	93.3	92.5	4.5	93.2	0.7	0.5	93.0

Type	str myr	ksp nm	ksp core	plag core	ksp recryst	ksp recryst	ksp recryst	plag matrix	plag core	plag matrix	plag core	plag matrix	plag matrix	plag core
SiO ₂	61.620	64.350	64.390	60.660	64.290	64.420	64.420	61.890	60.790	62.020	60.630	61.930	61.580	60.960
Al ₂ O ₃	24.150	18.760	18.790	24.620	18.650	18.550	18.650	23.920	24.620	23.950	24.870	24.050	23.990	24.470
MgO	0.000	0.000	0.000	0.000	0.000	0.000	0.000	0.000	0.000	0.000	0.000	0.000	0.005	0.000
CaO	5.650	0.050	0.046	6.210	0.007	0.000	0.007	5.440	6.150	5.280	6.260	5.340	5.490	6.030
FeO	0.004	0.016	0.000	0.020	0.034	0.000	0.004	0.029	0.045	0.059	0.011	0.068	0.061	0.011
Na ₂ O	8.430	0.707	0.765	8.130	0.597	0.431	0.624	8.470	8.130	8.650	8.170	8.560	8.470	8.120
SrO	0.086	0.127	0.113	0.111	0.117	0.089	0.082	0.102	0.106	0.120	0.102	0.099	0.101	0.101
K ₂ O	0.111	15.220	15.310	0.209	15.470	15.840	15.490	0.105	0.138	0.088	0.135	0.122	0.158	0.182
BaO	0.036	0.371	0.375	0.000	0.569	0.388	0.424	0.035	0.000	0.000	0.039	0.068	0.000	0.000
Total	100.086	99.601	99.789	99.960	99.733	99.719	99.700	99.990	99.979	100.167	100.218	100.237	99.855	99.875
Cations pfu														
Si	2.73	2.98	2.98	2.70	2.98	2.99	2.99	2.75	2.71	2.75	2.69	2.74	2.74	2.71
Al	1.26	1.03	1.03	1.29	1.02	1.01	1.02	1.25	1.29	1.25	1.30	1.26	1.26	1.28
Mg	0.00	0.00	0.00	0.00	0.00	0.00	0.00	0.00	0.00	0.00	0.00	0.00	0.00	0.00
Ca	0.27	0.00	0.00	0.30	0.00	0.00	0.00	0.26	0.29	0.25	0.30	0.25	0.26	0.29
Fe	0.00	0.00	0.00	0.00	0.00	0.00	0.00	0.00	0.00	0.00	0.00	0.00	0.00	0.00
Na	0.73	0.06	0.07	0.70	0.05	0.04	0.06	0.73	0.70	0.74	0.70	0.74	0.73	0.70
Sr	0.00	0.00	0.00	0.00	0.00	0.00	0.00	0.00	0.00	0.00	0.00	0.00	0.00	0.00
K	0.01	0.90	0.90	0.01	0.92	0.94	0.92	0.01	0.01	0.00	0.01	0.01	0.01	0.01
Ba	0.00	0.01	0.01	0.00	0.01	0.01	0.01	0.00	0.00	0.00	0.00	0.00	0.00	0.00
Total	5.00	4.99	4.99	5.01	4.99	4.99	4.99	5.00	5.00	5.00	5.01	5.00	5.00	5.00
End member composition														
An	26.9	0.3	0.2	29.3	0.0	0.0	0.0	26.0	29.2	25.1	29.5	25.5	26.1	28.8
Ab	72.5	6.6	7.0	69.5	5.5	4.0	5.8	73.4	70.0	74.4	69.7	73.9	73.0	70.2
Or	0.6	93.2	92.7	1.2	94.4	96.0	94.2	0.6	0.8	0.5	0.8	0.7	0.9	1.0

Type	plag core	plag core	plag core	plag core	ksp core	ksp core	ksp core	ksp core	ksp nm	myr	myr	ksp recrys	recrys myr	ksp nm
SiO ₂	60.700	60.800	60.520	60.820	64.310	64.370	64.390	64.560	64.050	75.590	62.430	64.470	62.710	64.450
Al ₂ O ₃	24.400	24.580	24.630	24.480	18.710	18.690	18.720	18.750	19.030	15.970	23.270	18.600	23.440	18.640
MgO	0.000	0.000	0.000	0.000	0.000	0.000	0.000	0.000	0.003	0.000	0.000	0.004	0.000	0.003
CaO	5.970	6.130	6.150	6.030	0.021	0.066	0.020	0.041	0.423	3.460	4.740	0.028	5.040	0.006
FeO	0.026	0.047	0.032	0.027	0.008	0.001	0.004	0.019	0.014	0.032	0.029	0.027	0.049	0.016
Na ₂ O	8.130	8.070	8.110	8.070	0.881	0.819	0.869	0.857	1.299	5.570	8.700	0.457	8.680	0.596
SrO	0.112	0.093	0.109	0.112	0.099	0.095	0.110	0.118	0.107	0.104	0.096	0.096	0.132	0.092
K ₂ O	0.187	0.194	0.179	0.146	15.160	15.170	15.290	15.060	14.390	0.079	0.105	15.610	0.084	15.570
BaO	0.000	0.033	0.000	0.013	0.494	0.282	0.374	0.265	0.534	0.003	0.040	0.517	0.000	0.258
Total	99.524	99.947	99.731	99.698	99.683	99.493	99.777	99.670	99.851	100.807	99.410	99.809	100.134	99.631
Cations pfu														
Si	2.71	2.71	2.70	2.71	2.98	2.99	2.98	2.99	2.96	3.21	2.78	2.99	2.77	2.99
Al	1.29	1.29	1.30	1.29	1.02	1.02	1.02	1.02	1.04	0.80	1.22	1.02	1.22	1.02
Mg	0.00	0.00	0.00	0.00	0.00	0.00	0.00	0.00	0.00	0.00	0.00	0.00	0.00	0.00
Ca	0.29	0.29	0.29	0.29	0.00	0.00	0.00	0.00	0.02	0.16	0.23	0.00	0.24	0.00
Fe	0.00	0.00	0.00	0.00	0.00	0.00	0.00	0.00	0.00	0.00	0.00	0.00	0.00	0.00
Na	0.70	0.70	0.70	0.70	0.08	0.07	0.08	0.08	0.12	0.46	0.75	0.04	0.74	0.05
Sr	0.00	0.00	0.00	0.00	0.00	0.00	0.00	0.00	0.00	0.00	0.00	0.00	0.00	0.00
K	0.01	0.01	0.01	0.01	0.90	0.90	0.90	0.89	0.85	0.00	0.01	0.92	0.00	0.92
Ba	0.00	0.00	0.00	0.00	0.01	0.01	0.01	0.00	0.01	0.00	0.00	0.01	0.00	0.00
Total	5.00	5.00	5.01	5.00	4.99	4.99	5.00	4.99	5.00	4.63	4.99	4.98	4.99	4.99
End member composition														
An	28.6	29.2	29.2	29.0	0.1	0.3	0.1	0.2	2.1	25.4	23.0	0.1	24.2	0.0
Ab	70.4	69.7	69.8	70.2	8.1	7.6	7.9	7.9	11.8	73.9	76.4	4.3	75.3	5.5
Or	1.1	1.1	1.0	0.8	91.8	92.1	92.0	91.8	86.1	0.7	0.6	95.6	0.5	94.5

Type	ksp nm	recrys myr	plag matrix	ksp core	ksp core	plag core	plag core	ksp inside	ksp inside	ksp recrys	ksp core	str myr	ksp nm	str myr
SiO ₂	64.400	62.130	62.100	64.410	64.310	60.650	60.780	64.650	64.400	64.320	64.340	63.920	64.380	64.620
Al ₂ O ₃	18.760	23.780	23.560	18.660	18.710	24.440	24.620	18.500	18.530	18.550	18.780	22.650	18.760	22.380
MgO	0.006	0.000	0.000	0.000	0.000	0.000	0.000	0.000	0.000	0.000	0.000	0.004	0.000	0.000
CaO	0.034	5.170	5.050	0.040	0.041	6.060	6.120	0.021	0.016	0.066	0.031	4.790	0.019	4.740
FeO	0.047	0.054	0.153	0.021	0.011	0.013	0.013	0.033	0.017	0.101	0.000	0.038	0.020	0.025
Na ₂ O	0.705	8.530	8.710	0.798	0.685	8.120	8.120	0.462	0.516	0.530	0.738	8.480	0.575	8.230
SrO	0.093	0.094	0.092	0.107	0.130	0.094	0.110	0.058	0.074	0.102	0.119	0.133	0.122	0.118
K ₂ O	15.360	0.123	0.136	15.400	15.440	0.159	0.150	15.730	15.800	15.580	15.290	0.070	15.440	0.121
BaO	0.383	0.000	0.003	0.348	0.382	0.000	0.016	0.206	0.116	0.385	0.367	0.023	0.511	0.000
Total	99.787	99.881	99.804	99.784	99.709	99.536	99.929	99.659	99.469	99.634	99.665	100.107	99.827	100.234
Cations pfu														
Si	2.98	2.76	2.76	2.98	2.98	2.71	2.71	3.00	2.99	2.99	2.98	2.82	2.98	2.84
Al	1.02	1.24	1.23	1.02	1.02	1.29	1.29	1.01	1.01	1.02	1.03	1.18	1.02	1.16
Mg	0.00	0.00	0.00	0.00	0.00	0.00	0.00	0.00	0.00	0.00	0.00	0.00	0.00	0.00
Ca	0.00	0.25	0.24	0.00	0.00	0.29	0.29	0.00	0.00	0.00	0.00	0.23	0.00	0.22
Fe	0.00	0.00	0.01	0.00	0.00	0.00	0.00	0.00	0.00	0.00	0.00	0.00	0.00	0.00
Na	0.06	0.73	0.75	0.07	0.06	0.70	0.70	0.04	0.05	0.05	0.07	0.73	0.05	0.70
Sr	0.00	0.00	0.00	0.00	0.00	0.00	0.00	0.00	0.00	0.00	0.00	0.00	0.00	0.00
K	0.91	0.01	0.01	0.91	0.91	0.01	0.01	0.93	0.94	0.92	0.90	0.00	0.91	0.01
Ba	0.01	0.00	0.00	0.01	0.01	0.00	0.00	0.00	0.00	0.01	0.01	0.00	0.01	0.00
Total	4.99	4.99	5.00	5.00	4.99	5.00	5.00	4.98	4.99	4.99	4.99	4.96	4.99	4.93
End member composition														
An	0.2	24.9	24.1	0.2	0.2	28.9	29.2	0.1	0.1	0.3	0.2	23.7	0.1	24.0
Ab	6.5	74.4	75.2	7.3	6.3	70.2	70.0	4.3	4.7	4.9	6.8	75.9	5.4	75.3
Or	93.3	0.7	0.8	92.5	93.5	0.9	0.8	95.6	95.2	94.8	93.0	0.4	94.6	0.7

Type	plag core	plag core	str myr	ksp nm	str myr	recrys myr	plag core	recrys myr	recrys myr	ksp nm	ksp core	recrys myr	recrys myr	recrys myr
SiO ₂	60.480	60.710	62.150	64.970	64.110	61.540	60.590	62.180	70.950	64.340	64.670	61.830	61.840	61.640
Al ₂ O ₃	24.610	24.530	23.660	18.830	23.090	24.010	24.460	23.830	19.110	18.650	18.670	23.720	23.970	24.060
MgO	0.000	0.000	0.000	0.002	0.000	0.002	0.007	0.000	0.001	0.000	0.000	0.005	0.002	0.000
CaO	6.210	6.070	5.080	0.772	5.050	5.390	6.040	5.280	3.500	0.037	0.033	5.370	5.320	5.490
FeO	0.039	0.023	0.008	0.013	0.000	0.016	0.000	0.030	0.036	0.008	0.000	0.032	0.021	0.041
Na ₂ O	7.990	8.000	8.680	1.670	8.400	8.480	8.080	8.590	7.670	0.779	0.754	8.420	8.490	8.430
SrO	0.113	0.101	0.118	0.085	0.106	0.105	0.100	0.101	0.141	0.142	0.133	0.097	0.103	0.099
K ₂ O	0.155	0.222	0.086	13.000	0.082	0.095	0.111	0.112	0.205	15.240	15.250	0.100	0.134	0.145
BaO	0.078	0.019	0.000	0.416	0.025	0.000	0.025	0.006	0.010	0.444	0.395	0.000	0.000	0.000
Total	99.675	99.675	99.782	99.757	100.862	99.638	99.413	100.129	101.623	99.639	99.904	99.574	99.881	99.905
Cations pfu														
Si	2.70	2.71	2.76	2.98	2.81	2.74	2.71	2.75	3.03	2.99	2.99	2.75	2.75	2.74
Al	1.30	1.29	1.24	1.02	1.19	1.26	1.29	1.24	0.96	1.02	1.02	1.24	1.25	1.26
Mg	0.00	0.00	0.00	0.00	0.00	0.00	0.00	0.00	0.00	0.00	0.00	0.00	0.00	0.00
Ca	0.30	0.29	0.24	0.04	0.24	0.26	0.29	0.25	0.16	0.00	0.00	0.26	0.25	0.26
Fe	0.00	0.00	0.00	0.00	0.00	0.00	0.00	0.00	0.00	0.00	0.00	0.00	0.00	0.00
Na	0.69	0.69	0.75	0.15	0.71	0.73	0.70	0.74	0.64	0.07	0.07	0.73	0.73	0.73
Sr	0.00	0.00	0.00	0.00	0.00	0.00	0.00	0.00	0.00	0.00	0.00	0.00	0.00	0.00
K	0.01	0.01	0.00	0.76	0.00	0.01	0.01	0.01	0.01	0.90	0.90	0.01	0.01	0.01
Ba	0.00	0.00	0.00	0.01	0.00	0.00	0.00	0.00	0.00	0.01	0.01	0.00	0.00	0.00
Total	5.00	5.00	5.00	4.96	4.96	5.00	5.00	5.00	4.81	4.99	4.99	4.99	5.00	5.00
End member composition														
An	29.8	29.2	24.3	4.0	24.8	25.9	29.0	25.2	19.9	0.2	0.2	25.9	25.5	26.2
Ab	69.3	69.6	75.2	15.7	74.7	73.6	70.3	74.2	78.8	7.2	7.0	73.5	73.7	72.9
Or	0.9	1.3	0.5	80.3	0.5	0.5	0.6	0.6	1.4	92.6	92.9	0.6	0.8	0.8

Type	ksp recrys	plag matrix	plag core	ksp core	str myr	ksp nm	str myr	ksp nm	str myr	ksp nm	str myr	ksp nm	ksp core	ksp core
SiO ₂	64.500	61.680	60.940	64.440	62.160	64.600	61.790	64.320	61.990	64.510	62.430	64.560	64.630	64.600
Al ₂ O ₃	18.670	23.970	24.470	18.790	23.760	18.710	23.910	18.740	23.800	18.670	23.560	18.760	18.740	18.700
MgO	0.000	0.000	0.000	0.000	0.000	0.003	0.000	0.000	0.000	0.000	0.000	0.003	0.001	0.000
CaO	0.019	5.400	6.050	0.052	5.220	0.029	5.270	0.046	5.290	0.045	5.130	0.036	0.041	0.045
FeO	0.022	0.029	0.046	0.010	0.026	0.020	0.008	0.021	0.027	0.014	0.006	0.039	0.000	0.036
Na ₂ O	0.352	8.460	8.100	0.790	8.570	0.735	8.660	0.738	8.530	0.737	8.630	0.757	0.763	0.806
SrO	0.095	0.105	0.105	0.104	0.121	0.140	0.109	0.138	0.108	0.126	0.101	0.131	0.130	0.108
K ₂ O	15.810	0.097	0.164	15.300	0.125	15.380	0.105	15.340	0.127	15.280	0.128	15.280	15.270	15.220
BaO	0.434	0.072	0.021	0.406	0.005	0.424	0.000	0.367	0.023	0.298	0.000	0.391	0.349	0.381
Total	99.901	99.813	99.897	99.891	99.987	100.041	99.852	99.710	99.895	99.679	99.985	99.956	99.924	99.897
Cations pfu														
Si	2.99	2.74	2.71	2.98	2.76	2.99	2.75	2.98	2.75	2.99	2.77	2.98	2.99	2.99
Al	1.02	1.26	1.28	1.02	1.24	1.02	1.25	1.02	1.25	1.02	1.23	1.02	1.02	1.02
Mg	0.00	0.00	0.00	0.00	0.00	0.00	0.00	0.00	0.00	0.00	0.00	0.00	0.00	0.00
Ca	0.00	0.26	0.29	0.00	0.25	0.00	0.25	0.00	0.25	0.00	0.24	0.00	0.00	0.00
Fe	0.00	0.00	0.00	0.00	0.00	0.00	0.00	0.00	0.00	0.00	0.00	0.00	0.00	0.00
Na	0.03	0.73	0.70	0.07	0.74	0.07	0.75	0.07	0.73	0.07	0.74	0.07	0.07	0.07
Sr	0.00	0.00	0.00	0.00	0.00	0.00	0.00	0.00	0.00	0.00	0.00	0.00	0.00	0.00
K	0.93	0.01	0.01	0.90	0.01	0.91	0.01	0.91	0.01	0.90	0.01	0.90	0.90	0.90
Ba	0.01	0.00	0.00	0.01	0.00	0.01	0.00	0.01	0.00	0.01	0.00	0.01	0.01	0.01
Total	4.99	5.00	5.00	4.99	4.99	4.99	5.00	4.99	5.00	4.99	4.99	4.99	4.99	4.99
End member composition														
An	0.1	25.9	28.9	0.3	25.0	0.1	25.0	0.2	25.3	0.2	24.5	0.2	0.2	0.2
Ab	3.3	73.5	70.1	7.3	74.3	6.8	74.4	6.8	73.9	6.8	74.7	7.0	7.0	7.4
Or	96.6	0.6	0.9	92.5	0.7	93.1	0.6	93.0	0.7	93.0	0.7	92.8	92.7	92.3

Type	ksp core	ksp core	ksp recrys	ksp recrys	str myr	recrys myr	ksp nm	recrys myr	recrys myr	ksp nm	ksp nm	plag matrix	plag matrix	plag matrix
SiO ₂	64.420	64.560	64.390	64.510	61.840	61.580	64.360	62.180	62.100	64.270	64.260	61.800	62.120	61.840
Al ₂ O ₃	18.710	18.630	18.590	18.560	23.860	24.200	18.720	23.650	23.770	18.730	18.690	23.860	23.760	23.780
MgO	0.000	0.003	0.000	0.000	0.000	0.000	0.005	0.000	0.000	0.000	0.004	0.004	0.000	0.002
CaO	0.040	0.020	0.009	0.018	5.030	5.470	0.060	4.980	5.080	0.034	0.033	5.250	5.080	5.100
FeO	0.005	0.033	0.009	0.026	0.036	0.000	0.011	0.014	0.005	0.018	0.047	0.108	0.039	0.055
Na ₂ O	0.799	0.764	0.370	0.472	8.660	8.310	0.681	8.570	8.490	0.652	0.706	8.390	8.590	8.580
SrO	0.108	0.126	0.084	0.083	0.095	0.087	0.115	0.104	0.112	0.107	0.129	0.099	0.117	0.089
K ₂ O	15.960	15.880	16.530	16.330	0.135	0.104	15.990	0.139	0.139	15.960	15.930	0.081	0.144	0.141
BaO	0.316	0.407	0.471	0.461	0.014	0.000	0.449	0.019	0.004	0.461	0.371	0.028	0.033	0.000
Total	100.358	100.422	100.452	100.460	99.670	99.751	100.392	99.656	99.699	100.232	100.171	99.621	99.883	99.586
Cations pfu														
Si	2.98	2.98	2.98	2.98	2.75	2.74	2.98	2.76	2.76	2.98	2.98	2.75	2.76	2.75
Al	1.02	1.01	1.01	1.01	1.25	1.27	1.02	1.24	1.24	1.02	1.02	1.25	1.24	1.25
Mg	0.00	0.00	0.00	0.00	0.00	0.00	0.00	0.00	0.00	0.00	0.00	0.00	0.00	0.00
Ca	0.00	0.00	0.00	0.00	0.24	0.26	0.00	0.24	0.24	0.00	0.00	0.25	0.24	0.24
Fe	0.00	0.00	0.00	0.00	0.00	0.00	0.00	0.00	0.00	0.00	0.00	0.00	0.00	0.00
Na	0.07	0.07	0.03	0.04	0.75	0.72	0.06	0.74	0.73	0.06	0.06	0.72	0.74	0.74
Sr	0.00	0.00	0.00	0.00	0.00	0.00	0.00	0.00	0.00	0.00	0.00	0.00	0.00	0.00
K	0.94	0.94	0.98	0.96	0.01	0.01	0.94	0.01	0.01	0.94	0.94	0.00	0.01	0.01
Ba	0.01	0.01	0.01	0.01	0.00	0.00	0.01	0.00	0.00	0.01	0.01	0.00	0.00	0.00
Total	5.02	5.01	5.02	5.01	5.00	4.99	5.02	4.99	4.99	5.01	5.02	4.99	4.99	5.00
End member composition														
An	0.2	0.1	0.0	0.1	24.1	26.5	0.3	24.1	24.6	0.2	0.2	25.6	24.4	24.5
Ab	7.1	6.8	3.3	4.2	75.1	72.9	6.1	75.1	74.5	5.8	6.3	74.0	74.7	74.7
Or	92.8	93.1	96.7	95.7	0.8	0.6	93.6	0.8	0.8	94.0	93.5	0.5	0.8	0.8

Type	plag matrix	plag matrix	ksp recrys	plag core	plag matrix	plag matrix	plag matrix	plag matrix	recrys myr	ksp nm	recrys myr	ksp nm	plag matrix	plag matrix
SiO ₂	61.890	60.920	64.360	60.610	61.620	61.660	62.020	61.780	62.160	64.330	62.090	64.290	61.540	61.620
Al ₂ O ₃	23.940	24.390	18.630	24.690	24.070	23.940	23.800	23.990	23.650	18.700	23.350	18.620	23.990	23.910
MgO	0.000	0.004	0.003	0.002	0.000	0.002	0.000	0.030	0.003	0.000	0.000	0.000	0.000	0.000
CaO	5.160	5.710	0.005	6.080	5.420	5.310	5.260	5.060	5.080	0.017	5.020	0.017	5.510	5.350
FeO	0.088	0.131	0.123	0.032	0.152	0.176	0.140	0.112	0.047	0.000	0.031	0.004	0.183	0.175
Na ₂ O	8.540	8.160	0.394	7.960	8.330	8.410	8.680	8.460	8.680	0.723	8.770	0.674	8.420	8.480
SrO	0.093	0.116	0.074	0.094	0.102	0.084	0.100	0.112	0.125	0.132	0.121	0.112	0.112	0.109
K ₂ O	0.093	0.090	16.570	0.128	0.147	0.106	0.126	0.346	0.086	15.190	0.091	15.200	0.139	0.114
BaO	0.028	0.030	0.444	0.011	0.000	0.029	0.000	0.037	0.024	0.431	0.000	0.349	0.002	0.000
Total	99.832	99.551	100.604	99.607	99.841	99.718	100.126	99.927	99.856	99.522	99.473	99.266	99.895	99.758
Cations pfu														
Si	2.75	2.72	2.98	2.70	2.74	2.74	2.75	2.75	2.76	2.99	2.77	2.99	2.74	2.74
Al	1.25	1.28	1.02	1.30	1.26	1.26	1.24	1.26	1.24	1.02	1.23	1.02	1.26	1.25
Mg	0.00	0.00	0.00	0.00	0.00	0.00	0.00	0.00	0.00	0.00	0.00	0.00	0.00	0.00
Ca	0.25	0.27	0.00	0.29	0.26	0.25	0.25	0.24	0.24	0.00	0.24	0.00	0.26	0.26
Fe	0.00	0.00	0.00	0.00	0.01	0.01	0.01	0.00	0.00	0.00	0.00	0.00	0.01	0.01
Na	0.74	0.71	0.04	0.69	0.72	0.73	0.75	0.73	0.75	0.07	0.76	0.06	0.73	0.73
Sr	0.00	0.00	0.00	0.00	0.00	0.00	0.00	0.00	0.00	0.00	0.00	0.00	0.00	0.00
K	0.01	0.01	0.98	0.01	0.01	0.01	0.01	0.02	0.00	0.90	0.01	0.90	0.01	0.01
Ba	0.00	0.00	0.01	0.00	0.00	0.00	0.00	0.00	0.00	0.01	0.00	0.01	0.00	0.00
Total	4.99	5.00	5.02	4.99	4.99	4.99	5.00	5.00	5.00	4.99	5.00	4.98	5.00	5.00
End member composition														
An	24.9	27.7	0.0	29.5	26.2	25.7	24.9	24.3	24.3	0.1	23.9	0.1	26.3	25.7
Ab	74.6	71.7	3.5	69.8	72.9	73.7	74.4	73.7	75.2	6.7	75.6	6.3	72.9	73.7
Or	0.5	0.5	96.5	0.7	0.8	0.6	0.7	2.0	0.5	93.2	0.5	93.6	0.8	0.7

Type	plag matrix	plag matrix	plag matrix	plag core	plag matrix	ksp inside	plag core	plag core	plag core	plag core	plag matrix	ksp core	ksp inside	ksp recryst
SiO ₂	61.760	62.110	61.540	60.990	61.640	64.260	60.440	60.500	60.800	61.030	61.930	64.610	64.640	64.350
Al ₂ O ₃	23.790	23.790	24.010	24.390	23.890	18.700	24.500	24.690	24.500	24.310	23.850	18.760	18.590	18.520
MgO	0.000	0.000	0.001	0.000	0.003	0.000	0.000	0.008	0.000	0.000	0.008	0.000	0.000	0.000
CaO	5.250	5.190	5.540	6.050	5.400	0.030	6.180	6.330	5.970	5.850	5.240	0.045	0.021	0.000
FeO	0.077	0.096	0.101	0.063	0.202	0.057	0.026	0.045	0.028	0.058	0.055	0.027	0.016	0.004
Na ₂ O	8.550	8.570	8.390	8.020	8.560	0.519	7.960	7.830	7.990	8.120	8.660	0.687	0.504	0.375
SrO	0.110	0.099	0.100	0.099	0.104	0.100	0.103	0.119	0.117	0.097	0.106	0.117	0.105	0.097
K ₂ O	0.164	0.143	0.137	0.155	0.161	15.530	0.219	0.235	0.218	0.188	0.148	15.350	16.090	16.320
BaO	0.014	0.022	0.000	0.000	0.000	0.545	0.004	0.047	0.011	0.007	0.052	0.355	0.370	0.257
Total	99.714	100.019	99.819	99.767	99.960	99.741	99.432	99.804	99.634	99.661	100.048	99.951	100.335	99.923
Cations pfu														
Si	2.75	2.75	2.74	2.72	2.74	2.98	2.71	2.70	2.71	2.72	2.75	2.99	2.99	2.99
Al	1.25	1.24	1.26	1.28	1.25	1.02	1.29	1.30	1.29	1.28	1.25	1.02	1.01	1.01
Mg	0.00	0.00	0.00	0.00	0.00	0.00	0.00	0.00	0.00	0.00	0.00	0.00	0.00	0.00
Ca	0.25	0.25	0.26	0.29	0.26	0.00	0.30	0.30	0.29	0.28	0.25	0.00	0.00	0.00
Fe	0.00	0.00	0.00	0.00	0.01	0.00	0.00	0.00	0.00	0.00	0.00	0.00	0.00	0.00
Na	0.74	0.74	0.72	0.69	0.74	0.05	0.69	0.68	0.69	0.70	0.75	0.06	0.05	0.03
Sr	0.00	0.00	0.00	0.00	0.00	0.00	0.00	0.00	0.00	0.00	0.00	0.00	0.00	0.00
K	0.01	0.01	0.01	0.01	0.01	0.92	0.01	0.01	0.01	0.01	0.01	0.90	0.95	0.97
Ba	0.00	0.00	0.00	0.00	0.00	0.01	0.00	0.00	0.00	0.00	0.00	0.01	0.01	0.00
Total	5.00	5.00	5.00	4.99	5.01	4.99	5.00	5.00	4.99	5.00	5.00	4.99	5.00	5.01
End member composition														
An	25.1	24.9	26.5	29.2	25.6	0.2	29.6	30.5	28.9	28.2	24.8	0.2	0.1	0.0
Ab	74.0	74.3	72.7	70.0	73.5	4.8	69.1	68.2	69.9	70.8	74.3	6.4	4.5	3.4
Or	0.9	0.8	0.8	0.9	0.9	95.0	1.3	1.3	1.3	1.1	0.8	93.4	95.4	96.6

Type	ksp recrys	plag matrix	plag matrix	plag matrix	plag matrix	ksp recrys	ksp core	str myr	ksp nm	str myr	ksp nm	str myr	ksp nm	ksp recrys
SiO ₂	64.480	62.180	61.870	62.220	62.000	64.360	63.740	62.230	64.130	62.110	64.180	61.910	64.550	64.320
Al ₂ O ₃	18.580	23.800	24.000	23.720	23.880	18.730	18.670	23.980	18.690	23.940	18.730	23.910	18.790	18.520
MgO	0.000	0.003	0.000	0.000	0.000	0.000	0.000	0.000	0.001	0.000	0.000	0.000	0.000	0.000
CaO	0.010	4.990	5.190	4.950	5.160	0.014	0.027	5.260	0.019	5.110	0.039	5.210	0.024	0.073
FeO	0.000	0.267	0.082	0.045	0.044	0.040	0.004	0.005	0.011	0.029	0.010	0.034	0.033	0.037
Na ₂ O	0.349	8.360	8.150	8.250	8.260	0.654	0.696	8.200	0.629	8.250	0.644	8.270	0.640	0.346
SrO	0.094	0.128	0.098	0.099	0.102	0.095	0.123	0.134	0.127	0.081	0.158	0.086	0.138	0.107
K ₂ O	16.360	0.141	0.150	0.156	0.188	15.890	15.650	0.131	15.930	0.122	15.910	0.184	15.980	16.420
BaO	0.319	0.000	0.000	0.003	0.029	0.501	0.467	0.012	0.532	0.000	0.337	0.033	0.441	0.387
Total	100.192	99.868	99.539	99.444	99.663	100.284	99.377	99.952	100.070	99.641	100.008	99.637	100.596	100.209
Cations pfu														
Si	2.99	2.76	2.75	2.77	2.76	2.98	2.97	2.76	2.98	2.76	2.98	2.75	2.98	2.98
Al	1.01	1.24	1.26	1.24	1.25	1.02	1.03	1.25	1.02	1.25	1.02	1.25	1.02	1.01
Mg	0.00	0.00	0.00	0.00	0.00	0.00	0.00	0.00	0.00	0.00	0.00	0.00	0.00	0.00
Ca	0.00	0.24	0.25	0.24	0.25	0.00	0.00	0.25	0.00	0.24	0.00	0.25	0.00	0.00
Fe	0.00	0.01	0.00	0.00	0.00	0.00	0.00	0.00	0.00	0.00	0.00	0.00	0.00	0.00
Na	0.03	0.72	0.70	0.71	0.71	0.06	0.06	0.70	0.06	0.71	0.06	0.71	0.06	0.03
Sr	0.00	0.00	0.00	0.00	0.00	0.00	0.00	0.00	0.00	0.00	0.00	0.00	0.00	0.00
K	0.97	0.01	0.01	0.01	0.01	0.94	0.93	0.01	0.94	0.01	0.94	0.01	0.94	0.97
Ba	0.01	0.00	0.00	0.00	0.00	0.01	0.01	0.00	0.01	0.00	0.01	0.00	0.01	0.01
Total	5.01	4.98	4.97	4.97	4.98	5.01	5.01	4.97	5.01	4.97	5.01	4.98	5.01	5.01
End member composition														
An	0.0	24.6	25.8	24.7	25.4	0.1	0.1	26.0	0.1	25.3	0.2	25.5	0.1	0.4
Ab	3.1	74.6	73.3	74.4	73.5	5.9	6.3	73.3	5.7	74.0	5.8	73.4	5.7	3.1
Or	96.8	0.8	0.9	0.9	1.1	94.0	93.5	0.8	94.2	0.7	94.0	1.1	94.1	96.6

Type		plag matrix	plag matrix	plag matrix	plag matrix	plag matrix	plag matrix	plag core	plag matrix	plag matrix	ksp inside	ksp inside	ksp recrys	ksp recrys
SiO ₂	64.070	61.760	61.680	61.800	61.690	61.660	62.090	60.580	61.360	61.620	64.810	64.630	64.680	64.670
Al ₂ O ₃	18.560	23.920	23.990	23.840	23.910	24.050	23.750	24.800	24.220	24.080	18.540	18.500	18.670	18.630
MgO	0.000	0.007	0.004	0.000	0.000	0.000	0.000	0.003	0.000	0.006	0.007	0.004	0.000	0.001
CaO	0.012	5.300	5.290	5.300	5.280	5.450	5.130	6.320	5.620	5.460	0.036	0.035	0.003	0.011
FeO	0.019	0.232	0.206	0.112	0.135	0.172	0.298	0.029	0.187	0.201	0.034	0.000	0.198	0.067
Na ₂ O	0.363	8.200	8.070	8.320	8.480	8.390	8.630	7.790	8.370	8.550	0.450	0.400	0.632	0.600
SrO	0.072	0.093	0.135	0.127	0.092	0.101	0.094	0.129	0.102	0.116	0.113	0.075	0.075	0.078
K ₂ O	16.440	0.144	0.119	0.103	0.164	0.143	0.145	0.214	0.128	0.140	15.680	15.790	15.460	15.540
BaO	0.367	0.042	0.000	0.049	0.000	0.000	0.000	0.041	0.059	0.011	0.253	0.273	0.435	0.346
Total	99.903	99.698	99.494	99.651	99.750	99.965	100.136	99.905	100.047	100.184	99.922	99.707	100.153	99.943
Cations pfu														
Si	2.98	2.75	2.75	2.75	2.74	2.74	2.75	2.70	2.73	2.73	3.00	3.00	2.99	2.99
Al	1.02	1.25	1.26	1.25	1.25	1.26	1.24	1.30	1.27	1.26	1.01	1.01	1.02	1.02
Mg	0.00	0.00	0.00	0.00	0.00	0.00	0.00	0.00	0.00	0.00	0.00	0.00	0.00	0.00
Ca	0.00	0.25	0.25	0.25	0.25	0.26	0.24	0.30	0.27	0.26	0.00	0.00	0.00	0.00
Fe	0.00	0.01	0.01	0.00	0.01	0.01	0.01	0.00	0.01	0.01	0.00	0.00	0.01	0.00
Na	0.03	0.71	0.70	0.72	0.73	0.72	0.74	0.67	0.72	0.74	0.04	0.04	0.06	0.05
Sr	0.00	0.00	0.00	0.00	0.00	0.00	0.00	0.00	0.00	0.00	0.00	0.00	0.00	0.00
K	0.98	0.01	0.01	0.01	0.01	0.01	0.01	0.01	0.01	0.01	0.92	0.93	0.91	0.92
Ba	0.01	0.00	0.00	0.00	0.00	0.00	0.00	0.00	0.00	0.00	0.00	0.00	0.01	0.01
Total	5.02	4.98	4.97	4.99	5.00	5.00	5.00	4.99	5.00	5.01	4.98	4.98	4.99	4.99
End member composition														
An	0.1	26.1	26.4	25.9	25.4	26.2	24.5	30.6	26.9	25.9	0.2	0.2	0.0	0.1
Ab	3.2	73.1	72.9	73.5	73.7	73.0	74.7	68.2	72.4	73.3	4.2	3.7	5.8	5.5
Or	96.7	0.8	0.7	0.6	0.9	0.8	0.8	1.2	0.7	0.8	95.6	96.1	94.1	94.4

Type	str myr	ksp nm	str myr	ksp nm	str myr	ksp nm	str myr	ksp nm	ksp core	ksp core		plag matrix	ksp recryst	plag core
SiO ₂	62.030	64.200	62.890	64.500	62.190	64.320	62.340	64.280	64.490	64.500	64.560	61.910	64.340	60.980
Al ₂ O ₃	23.670	18.750	23.240	18.750	23.520	18.640	23.810	18.750	18.710	18.600	18.700	23.880	18.670	24.570
MgO	0.000	0.000	0.000	0.000	0.000	0.000	0.000	0.002	0.000	0.000	0.000	0.004	0.004	0.000
CaO	5.020	0.022	4.540	0.017	4.880	0.038	5.060	0.016	0.033	0.043	0.038	5.000	0.007	5.950
FeO	0.017	0.000	0.006	0.013	0.005	0.001	0.002	0.000	0.012	0.015	0.008	0.043	0.066	0.022
Na ₂ O	8.710	0.656	9.090	0.683	8.830	0.757	8.660	0.674	0.803	0.802	0.881	8.440	0.551	7.970
SrO	0.117	0.139	0.115	0.143	0.119	0.120	0.130	0.122	0.144	0.091	0.107	0.103	0.099	0.108
K ₂ O	0.121	15.400	0.093	15.300	0.150	15.250	0.101	15.300	15.300	15.250	15.740	0.131	16.080	0.123
BaO	0.040	0.454	0.080	0.422	0.000	0.375	0.000	0.437	0.378	0.257	0.322	0.011	0.475	0.000
Total	99.725	99.622	100.055	99.828	99.694	99.501	100.103	99.580	99.871	99.557	100.356	99.522	100.292	99.723
Cations pfu														
Si	2.76	2.98	2.78	2.99	2.77	2.99	2.76	2.98	2.98	2.99	2.98	2.76	2.98	2.72
Al	1.24	1.03	1.21	1.02	1.23	1.02	1.24	1.03	1.02	1.02	1.02	1.25	1.02	1.29
Mg	0.00	0.00	0.00	0.00	0.00	0.00	0.00	0.00	0.00	0.00	0.00	0.00	0.00	0.00
Ca	0.24	0.00	0.22	0.00	0.23	0.00	0.24	0.00	0.00	0.00	0.00	0.24	0.00	0.28
Fe	0.00	0.00	0.00	0.00	0.00	0.00	0.00	0.00	0.00	0.00	0.00	0.00	0.00	0.00
Na	0.75	0.06	0.78	0.06	0.76	0.07	0.74	0.06	0.07	0.07	0.08	0.73	0.05	0.69
Sr	0.00	0.00	0.00	0.00	0.00	0.00	0.00	0.00	0.00	0.00	0.00	0.00	0.00	0.00
K	0.01	0.91	0.01	0.90	0.01	0.90	0.01	0.91	0.90	0.90	0.93	0.01	0.95	0.01
Ba	0.00	0.01	0.00	0.01	0.00	0.01	0.00	0.01	0.01	0.00	0.01	0.00	0.01	0.00
Total	5.00	4.99	5.00	4.99	5.00	4.99	4.99	4.99	4.99	4.99	5.01	4.99	5.01	4.99
End member composition														
An	24.0	0.1	21.5	0.1	23.2	0.2	24.3	0.1	0.2	0.2	0.2	24.5	0.0	29.0
Ab	75.3	6.1	78.0	6.4	76.0	7.0	75.2	6.3	7.4	7.4	7.8	74.8	5.0	70.3
Or	0.7	93.8	0.5	93.6	0.8	92.8	0.6	93.6	92.5	92.4	92.0	0.8	95.0	0.7

Type	str myr	str myr	ksp nm	ksp core	ksp recryst	str myr	plag matrix	plag matrix	ksp inside	plag matrix	plag matrix	plag matrix	plag matrix	plag matrix
SiO ₂	63.120	62.550	64.610	64.470	64.530	62.240	61.690	61.790	64.860	62.300	61.820	62.030	61.870	61.930
Al ₂ O ₃	23.140	23.550	18.780	18.740	18.650	23.880	23.990	23.980	18.560	23.810	23.950	23.820	23.930	24.030
MgO	0.000	0.000	0.000	0.000	0.000	0.003	0.003	0.000	0.006	0.005	0.001	0.000	0.000	0.000
CaO	4.190	4.730	0.047	0.054	0.003	5.040	5.280	5.220	0.032	5.050	5.220	4.920	5.180	5.290
FeO	0.013	0.014	0.028	0.026	0.000	0.055	0.084	0.072	0.012	0.275	0.295	0.167	0.115	0.092
Na ₂ O	8.910	8.640	0.806	0.937	0.628	8.060	8.180	8.270	0.508	8.390	8.390	8.470	8.440	8.320
SrO	0.099	0.109	0.123	0.114	0.096	0.108	0.118	0.121	0.083	0.120	0.105	0.095	0.130	0.112
K ₂ O	0.155	0.118	15.770	15.680	16.110	0.130	0.130	0.142	16.350	0.140	0.162	0.077	0.131	0.119
BaO	0.023	0.056	0.343	0.305	0.290	0.078	0.022	0.047	0.196	0.027	0.023	0.000	0.033	0.000
Total	99.650	99.766	100.506	100.325	100.306	99.594	99.497	99.642	100.607	100.117	99.967	99.579	99.829	99.893
Cations pfu														
Si	2.80	2.77	2.98	2.98	2.98	2.76	2.75	2.75	2.99	2.76	2.75	2.76	2.75	2.75
Al	1.21	1.23	1.02	1.02	1.02	1.25	1.26	1.26	1.01	1.24	1.25	1.25	1.25	1.26
Mg	0.00	0.00	0.00	0.00	0.00	0.00	0.00	0.00	0.00	0.00	0.00	0.00	0.00	0.00
Ca	0.20	0.22	0.00	0.00	0.00	0.24	0.25	0.25	0.00	0.24	0.25	0.23	0.25	0.25
Fe	0.00	0.00	0.00	0.00	0.00	0.00	0.00	0.00	0.00	0.01	0.01	0.01	0.00	0.00
Na	0.77	0.74	0.07	0.08	0.06	0.69	0.71	0.71	0.05	0.72	0.72	0.73	0.73	0.72
Sr	0.00	0.00	0.00	0.00	0.00	0.00	0.00	0.00	0.00	0.00	0.00	0.00	0.00	0.00
K	0.01	0.01	0.93	0.92	0.95	0.01	0.01	0.01	0.96	0.01	0.01	0.00	0.01	0.01
Ba	0.00	0.00	0.01	0.01	0.01	0.00	0.00	0.00	0.00	0.00	0.00	0.00	0.00	0.00
Total	4.98	4.98	5.01	5.02	5.01	4.96	4.98	4.98	5.01	4.98	4.99	4.98	4.99	4.98
End member composition														
An	20.4	23.1	0.2	0.3	0.0	25.5	26.1	25.6	0.2	24.8	25.3	24.2	25.1	25.8
Ab	78.7	76.2	7.2	8.3	5.6	73.7	73.1	73.5	4.5	74.4	73.7	75.4	74.1	73.5
Or	0.9	0.7	92.6	91.4	94.4	0.8	0.8	0.8	95.3	0.8	0.9	0.5	0.8	0.7

Type	ksp inside	ksp inside	recrys myr	recrys myr	ksp recrys	recrys myr	plag core	ksp core	ksp core	ksp core	ksp core	ksp nm	ksp core	plag matrix	plag matrix
SiO ₂	64.840	64.660	62.490	62.090	64.610	62.420	61.020	64.600	64.490	64.680	64.500	64.420	61.820	62.180	
Al ₂ O ₃	18.590	18.610	23.800	23.940	18.650	23.760	24.500	18.710	18.730	18.740	18.710	18.740	24.080	23.830	
MgO	0.005	0.003	0.000	0.000	0.000	0.000	0.000	0.002	0.003	0.003	0.003	0.003	0.000	0.001	
CaO	0.022	0.017	5.110	5.220	0.022	5.290	6.060	0.024	0.050	0.046	0.011	0.007	5.500	5.120	
FeO	0.022	0.018	0.034	0.004	0.001	0.033	0.015	0.022	0.023	0.003	0.016	0.001	0.038	0.031	
Na ₂ O	0.432	0.494	8.680	8.580	0.517	8.440	8.140	0.809	0.799	0.778	0.729	0.725	8.490	8.700	
SrO	0.080	0.081	0.101	0.121	0.085	0.091	0.128	0.132	0.115	0.103	0.092	0.119	0.123	0.101	
K ₂ O	16.540	16.370	0.165	0.100	15.610	0.117	0.210	15.160	15.230	15.120	15.260	15.250	0.157	0.138	
BaO	0.137	0.280	0.000	0.053	0.500	0.051	0.017	0.304	0.317	0.292	0.544	0.450	0.042	0.017	
Total	100.668	100.533	100.380	100.108	99.994	100.202	100.090	99.763	99.757	99.765	99.865	99.716	100.250	100.118	
Cations pfu															
Si	2.99	2.98	2.76	2.75	2.99	2.76	2.71	2.99	2.98	2.99	2.99	2.98	2.74	2.75	
Al	1.01	1.01	1.24	1.25	1.02	1.24	1.28	1.02	1.02	1.02	1.02	1.02	1.26	1.24	
Mg	0.00	0.00	0.00	0.00	0.00	0.00	0.00	0.00	0.00	0.00	0.00	0.00	0.00	0.00	
Ca	0.00	0.00	0.24	0.25	0.00	0.25	0.29	0.00	0.00	0.00	0.00	0.00	0.26	0.24	
Fe	0.00	0.00	0.00	0.00	0.00	0.00	0.00	0.00	0.00	0.00	0.00	0.00	0.00	0.00	
Na	0.04	0.04	0.74	0.74	0.05	0.72	0.70	0.07	0.07	0.07	0.07	0.07	0.73	0.75	
Sr	0.00	0.00	0.00	0.00	0.00	0.00	0.00	0.00	0.00	0.00	0.00	0.00	0.00	0.00	
K	0.97	0.96	0.01	0.01	0.92	0.01	0.01	0.89	0.90	0.89	0.90	0.90	0.01	0.01	
Ba	0.00	0.01	0.00	0.00	0.01	0.00	0.00	0.01	0.01	0.01	0.01	0.01	0.00	0.00	
Total	5.01	5.01	5.00	5.00	4.99	4.98	5.00	4.99	4.99	4.98	4.99	4.99	5.00	5.00	
End member composition															
An	0.1	0.1	24.3	25.0	0.1	25.6	28.8	0.1	0.3	0.2	0.1	0.0	26.1	24.3	
Ab	3.8	4.4	74.7	74.4	4.8	73.8	70.0	7.5	7.4	7.2	6.8	6.7	73.0	74.9	
Or	96.1	95.5	0.9	0.6	95.1	0.7	1.2	92.4	92.4	92.5	93.2	93.2	0.9	0.8	

Type	plag matrix	ksp recrys	ksp recrys	plag matrix	plag core	recrys myr	recrys myr	recrys myr	ksp nm	str myr	ksp nm	plag matrix	plag matrix	plag core
SiO ₂	61.920	64.550	64.620	61.940	60.600	61.710	62.340	61.870	64.730	61.780	64.440	61.830	61.400	60.780
Al ₂ O ₃	24.050	18.550	18.690	23.750	24.880	24.110	23.700	23.940	18.650	24.010	18.740	23.920	24.050	24.590
MgO	0.001	0.000	0.000	0.002	0.000	0.001	0.000	0.000	0.000	0.000	0.000	0.000	0.007	0.000
CaO	5.380	0.010	0.005	5.270	6.400	5.500	5.040	5.350	0.010	5.280	0.036	5.270	5.350	5.930
FeO	0.036	0.028	0.043	0.044	0.084	0.086	0.033	0.021	0.003	0.054	0.028	0.058	0.234	0.025
Na ₂ O	8.550	0.594	0.392	8.710	8.000	8.560	8.690	8.450	0.755	8.360	0.656	8.410	8.350	7.930
SrO	0.138	0.098	0.068	0.095	0.116	0.126	0.104	0.089	0.118	0.113	0.134	0.114	0.114	0.089
K ₂ O	0.174	15.510	15.760	0.185	0.130	0.133	0.137	0.155	15.930	0.128	16.100	0.102	0.133	0.229
BaO	0.029	0.289	0.340	0.001	0.022	0.011	0.000	0.000	0.382	0.014	0.314	0.000	0.018	0.000
Total	100.278	99.628	99.919	99.997	100.232	100.237	100.045	99.875	100.578	99.738	100.448	99.704	99.656	99.573
Cations pfu														
Si	2.74	2.99	2.99	2.75	2.69	2.74	2.76	2.75	2.98	2.75	2.98	2.75	2.74	2.71
Al	1.26	1.01	1.02	1.24	1.30	1.26	1.24	1.25	1.01	1.26	1.02	1.25	1.26	1.29
Mg	0.00	0.00	0.00	0.00	0.00	0.00	0.00	0.00	0.00	0.00	0.00	0.00	0.00	0.00
Ca	0.26	0.00	0.00	0.25	0.30	0.26	0.24	0.25	0.00	0.25	0.00	0.25	0.26	0.28
Fe	0.00	0.00	0.00	0.00	0.00	0.00	0.00	0.00	0.00	0.00	0.00	0.00	0.01	0.00
Na	0.73	0.05	0.04	0.75	0.69	0.74	0.75	0.73	0.07	0.72	0.06	0.72	0.72	0.69
Sr	0.00	0.00	0.00	0.00	0.00	0.00	0.00	0.00	0.00	0.00	0.00	0.00	0.00	0.00
K	0.01	0.92	0.93	0.01	0.01	0.01	0.01	0.01	0.94	0.01	0.95	0.01	0.01	0.01
Ba	0.00	0.01	0.01	0.00	0.00	0.00	0.00	0.00	0.01	0.00	0.01	0.00	0.00	0.00
Total	5.00	4.99	4.98	5.01	5.00	5.01	5.00	4.99	5.01	4.99	5.02	4.99	5.00	4.99
End member composition														
An	25.5	0.1	0.0	24.8	30.4	26.0	24.1	25.7	0.1	25.7	0.2	25.6	25.9	28.9
Ab	73.5	5.5	3.6	74.2	68.8	73.2	75.1	73.4	6.7	73.6	5.8	73.8	73.3	69.8
Or	1.0	94.5	96.3	1.0	0.7	0.7	0.8	0.9	93.2	0.7	94.0	0.6	0.8	1.3

Type	plag core	plag core	plag core	ksp core	ksp core	ksp core	recrys myr	ksp nm	recrys myr	ksp nm	recrys myr	ksp nm	ksp nm	recrys myr
SiO ₂	60.580	60.410	60.930	64.480	64.290	64.310	62.370	64.230	61.840	64.290	62.090	64.350	64.190	62.260
Al ₂ O ₃	24.660	24.760	24.600	18.740	18.660	18.720	23.590	18.700	23.800	18.590	23.670	18.720	18.630	23.680
MgO	0.004	0.000	0.004	0.000	0.010	0.006	0.000	0.000	0.000	0.000	0.000	0.000	0.003	0.000
CaO	6.170	6.130	6.020	0.026	0.003	0.035	4.760	0.037	5.070	0.011	4.940	0.022	0.011	4.970
FeO	0.048	0.067	0.033	0.026	0.031	0.029	0.019	0.018	0.024	0.001	0.000	0.032	0.034	0.087
Na ₂ O	7.910	7.810	7.860	0.787	0.708	0.790	8.580	0.781	8.420	0.763	8.550	0.778	0.797	8.490
SrO	0.090	0.090	0.113	0.134	0.137	0.124	0.123	0.111	0.100	0.096	0.116	0.112	0.111	0.104
K ₂ O	0.216	0.182	0.208	15.850	15.820	15.920	0.245	15.720	0.140	15.840	0.118	15.770	15.790	0.116
BaO	0.000	0.043	0.028	0.426	0.385	0.405	0.012	0.406	0.013	0.455	0.012	0.397	0.542	0.015
Total	99.677	99.491	99.795	100.469	100.043	100.339	99.699	100.003	99.406	100.045	99.495	100.181	100.107	99.723
Cations pfu														
Si	2.70	2.70	2.71	2.98	2.98	2.98	2.77	2.98	2.76	2.98	2.76	2.98	2.98	2.76
Al	1.30	1.30	1.29	1.02	1.02	1.02	1.23	1.02	1.25	1.02	1.24	1.02	1.02	1.24
Mg	0.00	0.00	0.00	0.00	0.00	0.00	0.00	0.00	0.00	0.00	0.00	0.00	0.00	0.00
Ca	0.29	0.29	0.29	0.00	0.00	0.00	0.23	0.00	0.24	0.00	0.24	0.00	0.00	0.24
Fe	0.00	0.00	0.00	0.00	0.00	0.00	0.00	0.00	0.00	0.00	0.00	0.00	0.00	0.00
Na	0.68	0.68	0.68	0.07	0.06	0.07	0.74	0.07	0.73	0.07	0.74	0.07	0.07	0.73
Sr	0.00	0.00	0.00	0.00	0.00	0.00	0.00	0.00	0.00	0.00	0.00	0.00	0.00	0.00
K	0.01	0.01	0.01	0.93	0.94	0.94	0.01	0.93	0.01	0.94	0.01	0.93	0.93	0.01
Ba	0.00	0.00	0.00	0.01	0.01	0.01	0.00	0.01	0.00	0.01	0.00	0.01	0.01	0.00
Total	5.00	4.99	4.99	5.01	5.01	5.02	4.99	5.01	4.99	5.01	4.99	5.01	5.02	4.98
End member composition														
An	29.7	29.9	29.4	0.1	0.0	0.2	23.1	0.2	24.8	0.1	24.0	0.1	0.1	24.3
Ab	69.0	69.0	69.4	7.0	6.4	7.0	75.5	7.0	74.4	6.8	75.3	7.0	7.1	75.0
Or	1.2	1.1	1.2	92.9	93.6	92.8	1.4	92.8	0.8	93.1	0.7	92.9	92.8	0.7

Type	ksp nm	plag matrix	plag matrix	error	error	plag core	ksp core	ksp recryst	ksp core	str myr	str myr	plag core	ksp nm	str myr
SiO ₂	64.190	62.030	61.750	61.690	60.600	60.860	64.120	64.230	64.380	61.850	61.700	60.430	64.170	63.380
Al ₂ O ₃	18.710	24.070	24.080	23.880	24.770	24.510	18.730	18.510	18.690	23.720	23.870	24.800	18.730	22.700
MgO	0.005	0.000	0.000	0.000	0.000	0.001	0.000	0.006	0.003	0.000	0.003	0.000	0.000	0.001
CaO	0.013	5.280	5.290	5.160	6.150	5.910	0.022	0.000	0.036	5.120	5.140	6.190	0.020	3.750
FeO	0.057	0.334	0.125	0.128	0.142	0.050	0.022	0.035	0.033	0.040	0.018	0.046	0.013	0.014
Na ₂ O	0.750	8.430	8.470	8.510	8.020	8.120	0.794	0.342	0.798	8.600	8.600	8.020	0.813	9.400
SrO	0.149	0.114	0.116	0.102	0.103	0.115	0.109	0.106	0.155	0.091	0.110	0.105	0.124	0.125
K ₂ O	15.820	0.127	0.140	0.139	0.107	0.193	15.860	16.480	15.770	0.119	0.114	0.120	15.680	0.078
BaO	0.447	0.000	0.000	0.000	0.000	0.002	0.381	0.301	0.276	0.000	0.000	0.059	0.462	0.000
Total	100.143	100.385	99.970	99.610	99.892	99.761	100.038	100.010	100.140	99.541	99.554	99.770	100.012	99.449
Cations pfu														
Si	2.98	2.74	2.74	2.75	2.70	2.71	2.97	2.98	2.98	2.75	2.75	2.70	2.98	2.81
Al	1.02	1.25	1.26	1.25	1.30	1.29	1.02	1.01	1.02	1.25	1.25	1.30	1.02	1.19
Mg	0.00	0.00	0.00	0.00	0.00	0.00	0.00	0.00	0.00	0.00	0.00	0.00	0.00	0.00
Ca	0.00	0.25	0.25	0.25	0.29	0.28	0.00	0.00	0.00	0.24	0.25	0.30	0.00	0.18
Fe	0.00	0.01	0.00	0.00	0.01	0.00	0.00	0.00	0.00	0.00	0.00	0.00	0.00	0.00
Na	0.07	0.72	0.73	0.73	0.69	0.70	0.07	0.03	0.07	0.74	0.74	0.69	0.07	0.81
Sr	0.00	0.00	0.00	0.00	0.00	0.00	0.00	0.00	0.00	0.00	0.00	0.00	0.00	0.00
K	0.94	0.01	0.01	0.01	0.01	0.01	0.94	0.98	0.93	0.01	0.01	0.01	0.93	0.00
Ba	0.01	0.00	0.00	0.00	0.00	0.00	0.01	0.01	0.01	0.00	0.00	0.00	0.01	0.00
Total	5.02	4.99	5.00	5.00	5.00	5.00	5.02	5.01	5.01	5.00	5.00	5.00	5.01	5.00
End member composition														
An	0.1	25.5	25.5	24.9	29.6	28.4	0.1	0.0	0.2	24.6	24.7	29.7	0.1	18.0
Ab	6.7	73.7	73.7	74.3	69.8	70.5	7.1	3.1	7.1	74.7	74.7	69.6	7.3	81.6
Or	93.2	0.7	0.8	0.8	0.6	1.1	92.8	96.9	92.7	0.7	0.6	0.7	92.6	0.4

Type	ksp nm	str myr	error	plag core	plag core	ksp inside	ksp inside	ksp recryst	ksp recryst	ksp core	ksp core	ksp core	ksp core	plag core
SiO ₂	63.990	61.920	61.260	60.130	60.730	64.040	64.160	64.240	64.420	64.360	64.460	64.030	64.210	60.560
Al ₂ O ₃	18.590	23.770	24.150	24.790	24.490	18.610	18.600	18.590	18.610	18.680	18.730	18.550	18.670	24.530
MgO	0.000	0.000	0.000	0.000	0.001	0.003	0.010	0.003	0.000	0.002	0.000	0.000	0.000	0.000
CaO	0.019	4.940	5.340	6.150	5.860	0.010	0.015	0.014	0.011	0.022	0.033	0.037	0.026	5.880
FeO	0.073	0.027	0.020	0.039	0.035	0.012	0.042	0.315	0.008	0.016	0.000	0.000	0.041	0.029
Na ₂ O	0.364	8.610	8.420	7.910	8.050	0.516	0.495	0.591	0.631	0.765	0.762	0.751	0.705	8.000
SrO	0.097	0.116	0.125	0.087	0.116	0.084	0.083	0.074	0.115	0.130	0.128	0.150	0.138	0.078
K ₂ O	16.420	0.109	0.139	0.119	0.184	16.150	16.270	16.160	16.110	15.930	15.780	15.860	15.980	0.222
BaO	0.310	0.011	0.011	0.000	0.000	0.442	0.329	0.322	0.403	0.432	0.396	0.316	0.382	0.059
Total	99.863	99.503	99.464	99.224	99.466	99.867	100.004	100.309	100.308	100.336	100.289	99.694	100.151	99.358
Cations pfu														
Si	2.98	2.76	2.73	2.69	2.71	2.98	2.98	2.98	2.98	2.98	2.98	2.98	2.98	2.71
Al	1.02	1.25	1.27	1.31	1.29	1.02	1.02	1.02	1.01	1.02	1.02	1.02	1.02	1.29
Mg	0.00	0.00	0.00	0.00	0.00	0.00	0.00	0.00	0.00	0.00	0.00	0.00	0.00	0.00
Ca	0.00	0.24	0.26	0.30	0.28	0.00	0.00	0.00	0.00	0.00	0.00	0.00	0.00	0.28
Fe	0.00	0.00	0.00	0.00	0.00	0.00	0.00	0.01	0.00	0.00	0.00	0.00	0.00	0.00
Na	0.03	0.74	0.73	0.69	0.70	0.05	0.04	0.05	0.06	0.07	0.07	0.07	0.06	0.69
Sr	0.00	0.00	0.00	0.00	0.00	0.00	0.00	0.00	0.00	0.00	0.00	0.00	0.00	0.00
K	0.97	0.01	0.01	0.01	0.01	0.96	0.96	0.96	0.95	0.94	0.93	0.94	0.94	0.01
Ba	0.01	0.00	0.00	0.00	0.00	0.01	0.01	0.01	0.01	0.01	0.01	0.01	0.01	0.00
Total	5.02	4.99	5.00	5.00	5.00	5.01	5.02	5.02	5.02	5.02	5.01	5.02	5.02	5.00
End member composition														
An	0.1	23.9	25.7	29.8	28.4	0.1	0.1	0.1	0.1	0.1	0.2	0.2	0.1	28.5
Ab	3.3	75.4	73.5	69.5	70.6	4.6	4.4	5.3	5.6	6.8	6.8	6.7	6.3	70.2
Or	96.7	0.6	0.8	0.7	1.1	95.3	95.5	94.7	94.3	93.1	93.0	93.1	93.6	1.3

Type	recrys myr	recrys myr	recrys myr	recrys myr	ksp nm	ksp core	ksp nm	recrys myr	recrys myr	recrys myr	recrys myr	ksp nm	plag core	ksp nm
SiO ₂	61.870	61.520	60.970	61.170	64.100	64.030	63.880	61.650	61.030	61.780	61.620	64.060	60.180	64.180
Al ₂ O ₃	23.610	24.010	24.020	23.900	18.570	18.570	18.600	23.730	24.170	23.720	23.870	18.620	24.880	18.700
MgO	0.000	0.000	0.000	0.000	0.003	0.002	0.005	0.000	0.000	0.000	0.001	0.005	0.000	0.000
CaO	4.960	5.330	5.450	5.190	0.027	0.014	0.004	5.060	5.570	4.970	5.170	0.015	6.380	0.023
FeO	0.011	0.028	0.020	0.019	0.024	0.032	0.027	0.019	0.043	0.033	0.054	0.048	0.022	0.000
Na ₂ O	8.600	8.340	8.270	8.440	0.346	0.677	0.596	8.410	8.120	8.440	8.460	0.609	7.960	0.613
SrO	0.079	0.118	0.125	0.118	0.094	0.090	0.095	0.105	0.110	0.126	0.116	0.095	0.104	0.083
K ₂ O	0.119	0.124	0.152	0.114	16.560	16.090	16.140	0.126	0.141	0.161	0.150	16.180	0.108	15.410
BaO	0.022	0.000	0.000	0.000	0.283	0.310	0.442	0.000	0.017	0.025	0.021	0.366	0.021	0.407
Total	99.272	99.469	99.006	98.952	100.006	99.815	99.788	99.100	99.201	99.256	99.462	99.998	99.655	99.417
Cations pfu														
Si	2.76	2.74	2.73	2.74	2.98	2.98	2.98	2.76	2.73	2.76	2.75	2.98	2.69	2.98
Al	1.24	1.26	1.27	1.26	1.02	1.02	1.02	1.25	1.27	1.25	1.25	1.02	1.31	1.02
Mg	0.00	0.00	0.00	0.00	0.00	0.00	0.00	0.00	0.00	0.00	0.00	0.00	0.00	0.00
Ca	0.24	0.25	0.26	0.25	0.00	0.00	0.00	0.24	0.27	0.24	0.25	0.00	0.31	0.00
Fe	0.00	0.00	0.00	0.00	0.00	0.00	0.00	0.00	0.00	0.00	0.00	0.00	0.00	0.00
Na	0.74	0.72	0.72	0.73	0.03	0.06	0.05	0.73	0.70	0.73	0.73	0.05	0.69	0.06
Sr	0.00	0.00	0.00	0.00	0.00	0.00	0.00	0.00	0.00	0.00	0.00	0.00	0.00	0.00
K	0.01	0.01	0.01	0.01	0.98	0.95	0.96	0.01	0.01	0.01	0.01	0.96	0.01	0.91
Ba	0.00	0.00	0.00	0.00	0.01	0.01	0.01	0.00	0.00	0.00	0.00	0.01	0.00	0.01
Total	4.99	4.99	5.00	5.00	5.02	5.02	5.02	4.99	4.99	4.99	4.99	5.02	5.00	4.99
End member composition														
An	24.0	25.9	26.5	25.2	0.1	0.1	0.0	24.8	27.3	24.3	25.0	0.1	30.5	0.1
Ab	75.3	73.4	72.7	74.1	3.1	6.0	5.3	74.5	71.9	74.7	74.1	5.4	68.9	5.7
Or	0.7	0.7	0.9	0.7	96.8	93.9	94.7	0.7	0.8	0.9	0.9	94.5	0.6	94.2

Type	str myr	str myr	str myr	ksp nm	str myr	ksp nm	plag core	plag matrix	error	error	plag matrix	plag matrix	plag matrix	ksp recryst
SiO ₂	66.770	62.540	61.890	64.060	61.630	64.210	60.230	61.140	61.880	60.350	61.870	61.160	61.750	64.350
Al ₂ O ₃	20.250	23.390	23.870	18.680	24.020	18.740	24.740	23.990	23.760	24.780	23.660	24.090	23.920	18.630
MgO	0.000	0.000	0.003	0.000	0.000	0.000	0.000	0.000	0.008	0.000	0.002	0.000	0.005	0.000
CaO	4.510	4.610	5.380	0.004	5.320	0.040	6.400	5.420	5.200	6.300	5.110	5.590	5.320	0.005
FeO	0.022	0.014	0.006	0.018	0.070	0.009	0.019	0.072	0.133	0.057	0.048	0.073	0.155	0.133
Na ₂ O	7.720	8.840	8.390	0.629	8.500	0.861	7.900	8.450	8.470	7.920	8.640	8.360	8.440	0.548
SrO	0.132	0.083	0.095	0.124	0.111	0.114	0.122	0.111	0.126	0.099	0.111	0.102	0.086	0.088
K ₂ O	0.105	0.093	0.142	15.430	0.125	15.150	0.145	0.143	0.134	0.127	0.115	0.082	0.132	15.500
BaO	0.047	0.000	0.006	0.379	0.000	0.319	0.066	0.025	0.043	0.000	0.000	0.006	0.012	0.305
Total	99.556	99.570	99.781	99.323	99.776	99.444	99.621	99.350	99.754	99.633	99.556	99.462	99.820	99.559
Cations pfu														
Si	2.94	2.78	2.75	2.98	2.74	2.98	2.69	2.73	2.75	2.70	2.76	2.73	2.75	2.99
Al	1.05	1.22	1.25	1.02	1.26	1.03	1.30	1.26	1.25	1.30	1.24	1.27	1.25	1.02
Mg	0.00	0.00	0.00	0.00	0.00	0.00	0.00	0.00	0.00	0.00	0.00	0.00	0.00	0.00
Ca	0.21	0.22	0.26	0.00	0.25	0.00	0.31	0.26	0.25	0.30	0.24	0.27	0.25	0.00
Fe	0.00	0.00	0.00	0.00	0.00	0.00	0.00	0.00	0.00	0.00	0.00	0.00	0.01	0.01
Na	0.66	0.76	0.72	0.06	0.73	0.08	0.68	0.73	0.73	0.69	0.75	0.72	0.73	0.05
Sr	0.00	0.00	0.00	0.00	0.00	0.00	0.00	0.00	0.00	0.00	0.00	0.00	0.00	0.00
K	0.01	0.01	0.01	0.92	0.01	0.90	0.01	0.01	0.01	0.01	0.01	0.00	0.01	0.92
Ba	0.00	0.00	0.00	0.01	0.00	0.01	0.00	0.00	0.00	0.00	0.00	0.00	0.00	0.01
Total	4.87	4.99	4.99	4.99	5.00	4.99	5.00	5.00	4.99	5.00	5.00	5.00	5.00	4.99
End member composition														
An	24.2	22.3	26.0	0.0	25.5	0.2	30.7	26.0	25.1	30.3	24.5	26.9	25.6	0.0
Ab	75.1	77.2	73.2	5.8	73.8	7.9	68.5	73.2	74.1	69.0	74.9	72.7	73.6	5.1
Or	0.7	0.5	0.8	94.1	0.7	91.9	0.8	0.8	0.8	0.7	0.7	0.5	0.8	94.9

Type	ksp recrys	plag core	plag matrix	plag matrix	plag matrix	plag matrix	plag matrix	plag matrix	plag matrix	str myr	ksp nm	ksp recrys	plag matrix	plag matrix	plag matrix
SiO ₂	64.440	60.470	60.870	60.960	61.590	61.930	61.350	60.540	61.780	64.100	64.200	61.410	64.530	61.490	
Al ₂ O ₃	18.560	24.560	24.420	24.080	23.800	23.660	23.930	24.660	23.700	18.630	18.570	23.830	21.880	23.900	
MgO	0.000	0.001	0.000	0.003	0.000	0.000	0.000	0.002	0.000	0.002	0.000	0.037	0.007	0.004	
CaO	0.007	6.200	5.690	5.680	5.250	5.030	5.350	6.190	5.070	0.005	0.046	4.880	4.620	5.280	
FeO	0.033	0.071	0.074	0.211	0.098	0.093	0.067	0.050	0.019	0.011	0.002	0.375	0.122	0.179	
Na ₂ O	0.339	8.080	8.140	8.280	8.480	8.430	8.370	7.890	8.530	0.651	0.404	8.450	8.270	8.470	
SrO	0.097	0.098	0.105	0.107	0.115	0.122	0.098	0.090	0.112	0.143	0.081	0.124	0.130	0.102	
K ₂ O	15.750	0.175	0.225	0.129	0.124	0.143	0.130	0.135	0.134	15.270	15.680	0.367	0.108	0.145	
BaO	0.399	0.000	0.000	0.000	0.000	0.012	0.000	0.012	0.000	0.528	0.397	0.000	0.000	0.032	
Total	99.625	99.655	99.524	99.451	99.457	99.420	99.295	99.569	99.345	99.340	99.381	99.474	99.667	99.602	
Cations pfu															
Si	2.99	2.70	2.72	2.73	2.75	2.76	2.74	2.70	2.76	2.98	2.99	2.74	2.85	2.74	
Al	1.02	1.29	1.29	1.27	1.25	1.24	1.26	1.30	1.25	1.02	1.02	1.25	1.14	1.26	
Mg	0.00	0.00	0.00	0.00	0.00	0.00	0.00	0.00	0.00	0.00	0.00	0.00	0.00	0.00	
Ca	0.00	0.30	0.27	0.27	0.25	0.24	0.26	0.30	0.24	0.00	0.00	0.23	0.22	0.25	
Fe	0.00	0.00	0.00	0.01	0.00	0.00	0.00	0.00	0.00	0.00	0.00	0.01	0.00	0.01	
Na	0.03	0.70	0.70	0.72	0.73	0.73	0.73	0.68	0.74	0.06	0.04	0.73	0.71	0.73	
Sr	0.00	0.00	0.00	0.00	0.00	0.00	0.00	0.00	0.00	0.00	0.00	0.00	0.00	0.00	
K	0.93	0.01	0.01	0.01	0.01	0.01	0.01	0.01	0.01	0.91	0.93	0.02	0.01	0.01	
Ba	0.01	0.00	0.00	0.00	0.00	0.00	0.00	0.00	0.00	0.01	0.01	0.00	0.00	0.00	
Total	4.98	5.01	5.00	5.00	5.00	4.99	4.99	4.99	4.99	4.99	4.99	5.01	4.93	5.00	
End member composition															
An	0.0	29.5	27.5	27.3	25.3	24.6	25.9	30.0	24.5	0.0	0.2	23.7	23.4	25.4	
Ab	3.2	69.5	71.2	72.0	74.0	74.6	73.3	69.2	74.7	6.1	3.8	74.2	75.9	73.8	
Or	96.8	1.0	1.3	0.7	0.7	0.8	0.7	0.8	0.8	93.9	96.0	2.1	0.7	0.8	

Type	ksp recrys	plag matrix	plag core	plag core	plag matrix	ksp recrys	flame	str myr	str myr	ksp nm	str myr	recrys myr	ksp nm	str myr
SiO ₂	63.960	61.600	60.480	60.630	61.600	64.110	67.540	61.460	61.800	64.000	61.580	61.730	63.930	61.240
Al ₂ O ₃	18.550	23.720	24.540	24.460	23.880	18.630	19.740	24.030	23.430	18.600	23.980	23.780	18.600	23.880
MgO	0.000	0.003	0.000	0.000	0.000	0.002	0.000	0.000	0.000	0.000	0.001	0.000	0.000	0.000
CaO	0.124	5.190	6.000	5.970	5.270	0.008	0.288	5.550	4.930	0.029	5.290	5.230	0.021	5.440
FeO	0.066	0.037	0.011	0.041	0.062	0.105	0.029	0.048	0.044	0.000	0.026	0.044	0.034	0.018
Na ₂ O	0.648	8.470	8.020	8.140	8.560	0.590	11.210	8.360	8.780	0.482	8.540	8.580	0.452	8.410
SrO	0.096	0.101	0.100	0.091	0.109	0.116	0.094	0.123	0.104	0.110	0.082	0.118	0.103	0.113
K ₂ O	15.170	0.113	0.109	0.101	0.146	15.220	0.142	0.129	0.119	15.370	0.123	0.155	15.570	0.080
BaO	0.406	0.004	0.000	0.017	0.000	0.544	0.000	0.010	0.000	0.509	0.000	0.054	0.321	0.000
Total	99.019	99.239	99.259	99.451	99.627	99.325	99.043	99.710	99.207	99.100	99.622	99.691	99.030	99.180
Cations pfu														
Si	2.98	2.75	2.71	2.71	2.74	2.99	2.98	2.74	2.76	2.99	2.74	2.75	2.98	2.74
Al	1.02	1.25	1.29	1.29	1.25	1.02	1.03	1.26	1.23	1.02	1.26	1.25	1.02	1.26
Mg	0.00	0.00	0.00	0.00	0.00	0.00	0.00	0.00	0.00	0.00	0.00	0.00	0.00	0.00
Ca	0.01	0.25	0.29	0.29	0.25	0.00	0.01	0.26	0.24	0.00	0.25	0.25	0.00	0.26
Fe	0.00	0.00	0.00	0.00	0.00	0.00	0.00	0.00	0.00	0.00	0.00	0.00	0.00	0.00
Na	0.06	0.73	0.70	0.71	0.74	0.05	0.96	0.72	0.76	0.04	0.74	0.74	0.04	0.73
Sr	0.00	0.00	0.00	0.00	0.00	0.00	0.00	0.00	0.00	0.00	0.00	0.00	0.00	0.00
K	0.90	0.01	0.01	0.01	0.01	0.90	0.01	0.01	0.01	0.91	0.01	0.01	0.93	0.00
Ba	0.01	0.00	0.00	0.00	0.00	0.01	0.00	0.00	0.00	0.01	0.00	0.00	0.01	0.00
Total	4.99	4.99	5.00	5.00	5.00	4.98	4.99	5.00	5.00	4.98	5.00	5.00	4.99	5.00
End member composition														
An	0.6	25.1	29.1	28.7	25.2	0.0	1.4	26.6	23.5	0.2	25.3	25.0	0.1	26.2
Ab	6.1	74.2	70.3	70.7	74.0	5.6	97.8	72.6	75.8	4.5	74.0	74.1	4.2	73.3
Or	93.3	0.7	0.6	0.6	0.8	94.4	0.8	0.7	0.7	95.3	0.7	0.9	95.7	0.5

Type	ksp nm	plag matrix	plag matrix
SiO ₂	64.020	61.680	61.310
Al ₂ O ₃	18.710	23.870	24.090
MgO	0.000	0.000	0.000
CaO	0.049	5.260	5.490
FeO	0.000	0.147	0.179
Na ₂ O	0.656	8.540	8.390
SrO	0.105	0.123	0.113
K ₂ O	15.240	0.110	0.139
BaO	0.376	0.000	0.000
Total	99.156	99.730	99.711
Cations pfu			
Si	2.98	2.75	2.73
Al	1.03	1.25	1.27
Mg	0.00	0.00	0.00
Ca	0.00	0.25	0.26
Fe	0.00	0.01	0.01
Na	0.06	0.74	0.72
Sr	0.00	0.00	0.00
K	0.91	0.01	0.01
Ba	0.01	0.00	0.00
Total	4.99	5.00	5.00
End member composition			
An	0.3	25.2	26.3
Ab	6.1	74.1	72.9
Or	93.6	0.6	0.8